

## Biomolecule electrotransfer to mammalian cells

Muralidharan, A.

**DOI**

[10.4233/uuid:5d44a19d-5916-4e06-9fef-b8902ae2433d](https://doi.org/10.4233/uuid:5d44a19d-5916-4e06-9fef-b8902ae2433d)

**Publication date**

2022

**Document Version**

Final published version

**Citation (APA)**

Muralidharan, A. (2022). *Biomolecule electrotransfer to mammalian cells*.  
<https://doi.org/10.4233/uuid:5d44a19d-5916-4e06-9fef-b8902ae2433d>

**Important note**

To cite this publication, please use the final published version (if applicable).  
Please check the document version above.

**Copyright**

Other than for strictly personal use, it is not permitted to download, forward or distribute the text or part of it, without the consent of the author(s) and/or copyright holder(s), unless the work is under an open content license such as Creative Commons.

**Takedown policy**

Please contact us and provide details if you believe this document breaches copyrights.  
We will remove access to the work immediately and investigate your claim.

# Biomolecule Electrotransfer to Mammalian Cells

## Invitation

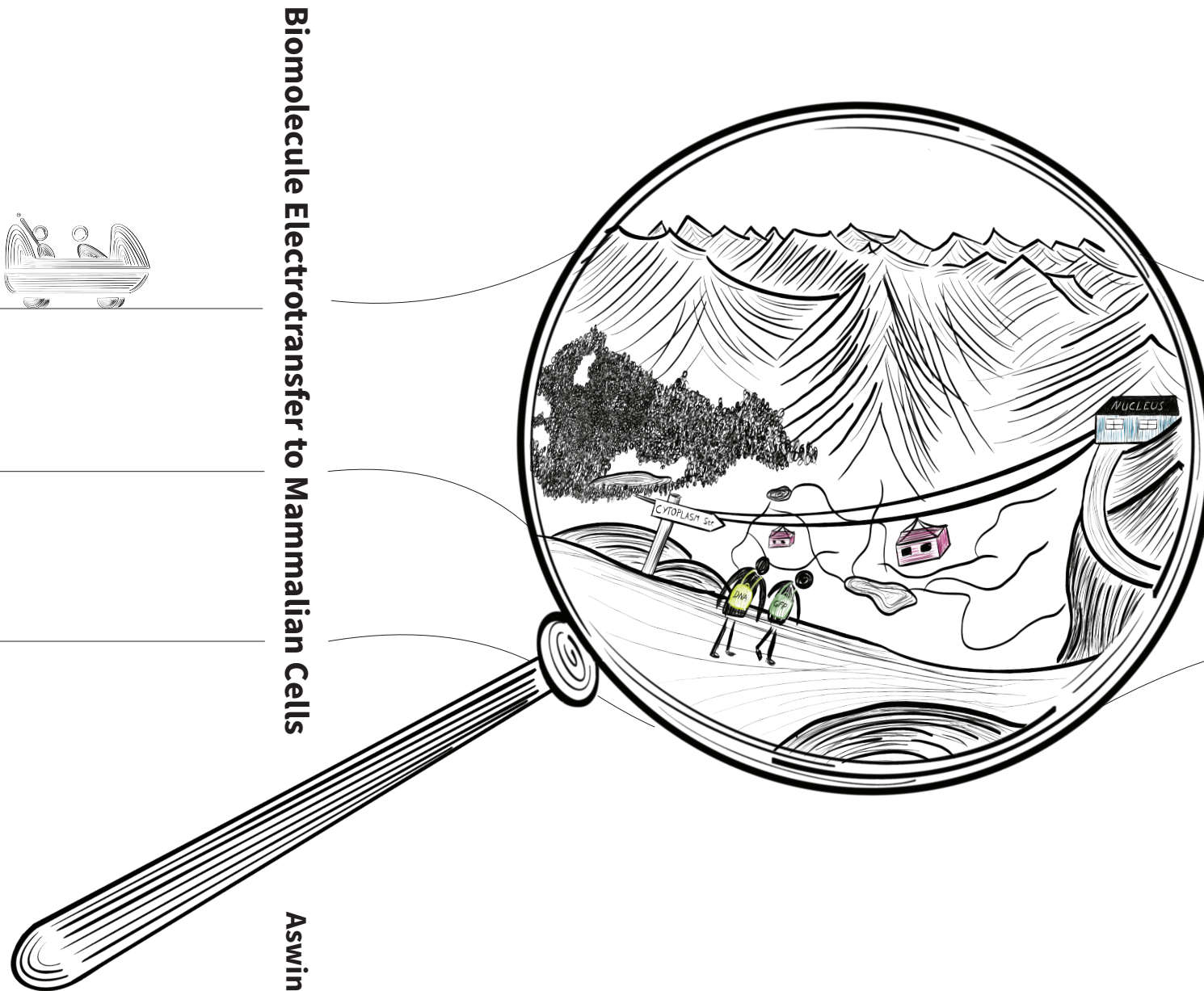
To the public defence of my doctoral thesis titled

## Biomolecule Electrotransfer to Mammalian Cells

Date | Time | Location  
26<sup>th</sup> of Oct, 2022.  
10:00 am,  
Senaatszaal,  
Aula, TU Delft,  
Mekelweg 5, Delft.

Aswin Muralidharan

aswinmuralidharan@gmail.com



Biomolecule Electrotransfer to Mammalian Cells

Aswin Muralidharan

Aswin Muralidharan

Casimir PhD Series, Delft-Leiden 2022-19  
ISBN 978-90-8593-531-5

# Propositions

accompanying the dissertation

## BIOMOLECULE ELECTROTRANSFER TO MAMMALIAN CELLS

by

**Aswin MURALIDHARAN**

1. The electroporation theory based on energetic costs of local membrane electro-pore opening fails to describe the added energy costs from anchored cytoskeletal networks.  
*This proposition pertains to chapter 2 of this thesis.*
2. It is not the DNA size but what it encounters in the cytosol which governs the intracellular electrotransferred DNA cargo transport.  
*This proposition pertains to chapter 3 of this thesis.*
3. A unified theory of electro-transfection will include the DNA size-dependent DNA-membrane complex formation and cell line dependent intracellular activity.  
*This proposition pertains to chapter 3 of this thesis and Sachdev et al., BBA Biomembranes, 2020.*
4. Scale-up is best achieved through continuous processing, that holds for localized electroporation.
5. Electroporation theoretical models help predict whether the cell membrane is permeabilized but do not help predict the associated molecule transport kinetics.
6. The global rollout of biomolecule electrotransfer in clinics will be governed by cost rather than the high efficiency and control that localized electroporation devices promise.  
*Based on ElectroPen (Byagathvalli et. al., PLoS Biology, 2020) and ePatch (Xia et. al., PNAS, 2021)*
7. Therapeutic promise of CRISPR-Cas9 will be met only when difficulty in delivering the required biomolecules *in vivo* is addressed.
8. Target specifications come first, and research questions second when it comes to development of new technologies.
9. The COVID-19 pandemic has shown that in-person mega-conferences are a waste of taxpayer money.
10. Lack of scores for gender diversity in the university rankings is the cause of gender inequality among university principal investigators.

These propositions are regarded as opposable and defensible, and have been approved as such by the promoters Dr. P.E. Boukany and Prof. dr. ir. M.T. Kreutzer

# **BIOMOLECULE ELECTROTRANSFER TO MAMMALIAN CELLS**



# **BIOMOLECULE ELECTROTRANSFER TO MAMMALIAN CELLS**

## **Dissertation**

for the purpose of obtaining the degree of doctor  
at Delft University of Technology,  
by the authority of the Rector Magnificus Prof. dr. ir. T.H.J.J. van der Hagen,  
Chair of the Board for Doctorates,  
to be defended publicly on  
Wednesday, 26 October 2022 at 10:00 o'clock.

by

**Aswin MURALIDHARAN**

Master of Science in Chemical Engineering,  
Delft University of Technology, The Netherlands,  
born in Calicut, Kerala, India.

The dissertation has been approved by

Promotor: Prof. dr. ir. M.T. Kreutzer

Promotor: Dr. P.E. Boukany

Composition of the doctoral committee:

Rector Magnificus,  
Prof. dr. ir. M.T. Kreutzer  
Dr. P.E. Boukany

Chairperson  
Delft University of Technology, promotor  
Delft University of Technology, promotor

Independent members:

Prof. dr. M.-P. Rols

Institut de Pharmacologie et de Biologie  
Structurale, CNRS Toulouse, France

Prof. dr. dr. h. c. D. Miklavčič

University of Ljubljana, Slovenia

Prof. dr. dipl.-ing. S. Kenjereš

Delft University of Technology

Prof. dr. S.J. Picken

Delft University of Technology

Dr. S. Wild

Miltenyi Biotec, Germany



This work was financially supported by the European Research Council.

*Keywords:* Electroporation, electrotransfer, cytoskeleton, anomalous diffusion,  
DNA transport, microfluidics, localized electroporation, gene delivery.

*Printed by:* Gildeprint.

*Front & Back:* The landscape of barriers by I. Bagemihl.

Copyright © 2022 by A. Muralidharan.

Casimir PhD Series, Delft-Leiden 2022-19.

ISBN 978-90-8593-531-5.

An electronic version of this dissertation is available at  
<http://repository.tudelft.nl/>.

# CONTENTS

<b>Summary</b>	<b>ix</b>
<b>Samenvatting</b>	<b>xi</b>
<b>1 Introduction and Overview</b>	<b>1</b>
1.1 Response of living cells to electric fields . . . . .	2
1.1.1 Induced transmembrane voltage. . . . .	2
1.1.2 Current state of the art of electroporation models . . . . .	3
1.1.3 Molecular transport during/after electrotransfer. . . . .	5
1.1.4 Localized electroporation . . . . .	8
References . . . . .	9
<b>2 Actin networks regulate the cell membrane permeability during electroporation</b>	<b>19</b>
2.1 Introduction . . . . .	20
2.2 Materials and methods . . . . .	22
2.2.1 Cell culture for electroporation . . . . .	22
2.2.2 Disruption of actin networks by latrunculin B treatment. . . . .	22
2.2.3 Electroporation of CHO cells. . . . .	23
2.2.4 Fluorescence imaging and analysis of propidium iodide uptake . . . . .	24
2.3 Results . . . . .	24
2.3.1 Disruption of actin networks results in increased uptake of propidium iodide during electroporation . . . . .	24
2.3.2 Temperature-dependent uptake of propidium iodide into CHO cells with intact and disrupted actin networks . . . . .	27
2.3.3 Effect of concentration of the propidium iodide on cellular uptake during electroporation at room temperature. . . . .	30
2.4 Discussion . . . . .	32
2.5 Conclusion . . . . .	35
2.A Propidium iodide uptake at different levels of disruption of actin . . . . .	36
2.B Fluorescence intensity due to propidium iodide uptake along the center-line of the cells . . . . .	37
2.C Propidium iodide uptake during electroporation at lower magnification (20x) . . . . .	39
2.D Analysis of propidium iodide uptake at different temperatures including temperature dependence of $D$ and $v$ . . . . .	39
2.E Temperature dependence of propidium iodide uptake at 600 V/cm. . . . .	42
2.F Robustness of the experimental fluorescence data . . . . .	43
2.G Numerical calculations . . . . .	44
2.G.1 Calculation of the induced transmembrane voltage . . . . .	45
2.G.2 Model of membrane electroporation. . . . .	46



2.H	Joule heating . . . . .	50
	References . . . . .	51
<b>3</b>	<b>Coexisting ergodic and non-ergodic intracellular transport of electrotransferred DNA cargo</b>	<b>59</b>
3.1	Introduction . . . . .	60
3.2	Materials and Methods . . . . .	61
3.2.1	Cell culture. . . . .	61
3.2.2	DNA staining and electrotransfer protocol . . . . .	62
3.2.3	DNA tracking experiments . . . . .	62
3.2.4	Data analysis. . . . .	62
3.2.5	Statistical analysis . . . . .	63
3.3	Results and Discussions. . . . .	63
3.3.1	Analysis of intracellular DNA cargo trafficking . . . . .	63
3.3.2	Intracellular anomalous diffusion of DNA cargo . . . . .	65
3.3.3	Coexistence of non-ergodic and ergodic processes in the intracellular DNA cargo dynamics . . . . .	68
3.3.4	Influence of cell's state on the electrotransferred DNA cargo transport . . . . .	71
3.4	Conclusions. . . . .	73
3.A	Intracellular transport of different sized DNA cargo in CHO-K1 cells . . . . .	75
3.A.1	Sample trajectories. . . . .	75
3.A.2	Ergodicity breaking . . . . .	76
3.A.3	Directional change distribution . . . . .	77
3.A.4	Apparent diffusion coefficient and anomalous exponent . . . . .	78
3.A.5	Classification of trajectories . . . . .	79
3.A.6	Velocity autocorrelation . . . . .	80
3.B	Intracellular transport of 500 bp DNA cargo in different cancer cells . . . . .	81
3.B.1	Non ergodicity of 500 bp DNA cargo in different cancer cells. . . . .	81
3.B.2	Apparent diffusion coefficient and anomalous exponent . . . . .	83
3.B.3	Classification of trajectories . . . . .	84
3.B.4	Directional change distribution . . . . .	85
	References . . . . .	86
<b>4</b>	<b>Micro-trap array on a chip for localized electroporation and electro-gene transfection</b>	<b>91</b>
4.1	Introduction . . . . .	92
4.2	Materials and methods . . . . .	93
4.2.1	Cell culture and preparation for microtrap electroporation . . . . .	93
4.2.2	Preparation of fluorescent molecules and plasmids for assessment of electroporation . . . . .	94
4.2.3	Device fabrication and experimental setup . . . . .	94
4.2.4	Delivery of biomolecules using microtrap array electroporation . . . . .	95
4.2.5	Fluorescence imaging of molecular uptake during microtrap array electroporation . . . . .	95
4.2.6	Numerical simulation of microtrap electroporation . . . . .	96

---

4.3	Results and discussions . . . . .	97
4.3.1	Microtrap array electroporation has high electroporation efficiency and maintains high cell viability . . . . .	97
4.3.2	Analysis of small molecules uptake with microtrap array electroporation . . . . .	99
4.3.3	Microtrap array electroporation induces localized cell membrane electroporation . . . . .	101
4.3.4	Plasmid DNA electrotransfer in microtrap array induce efficient gene transfection . . . . .	102
4.4	Conclusions. . . . .	104
4.A	Numerical calculations of electric field distributions in the microfluidic device. . . . .	105
4.B	Analysis of small molecule electrotransfer . . . . .	107
4.C	Bulk Electroporation . . . . .	109
4.D	Numerical calculations of electroporation . . . . .	110
4.E	Analysis of GFP expression . . . . .	114
	References . . . . .	114
<b>5</b>	<b>Conclusion and Outlook</b>	<b>121</b>
5.1	Role of actin. . . . .	121
5.2	Intracellular DNA transport . . . . .	122
5.3	Micro-trap electroporation . . . . .	122
	References . . . . .	123
	<b>Acknowledgements</b>	<b>127</b>
	<b>Curriculum Vitae</b>	<b>133</b>
	<b>List of Publications</b>	<b>135</b>



# SUMMARY

Delivery of biomolecules using pulsed electric fields or electrotransfer has applications such as biomedical engineering, bioprocess engineering and genomic engineering. When a cell is placed in an electric field, the induced transmembrane voltage catalyzes the formation of pores on the cell membrane. This enables the delivery of otherwise cell membrane-impermeable molecules to the cells. Despite the broad significance, a complete biophysical understanding of electrotransfer at a subcellular level and a translation of electroporation as a high-throughput and high-efficiency technique is still lacking.

In this dissertation: *(i)* we unravel how actin networks regulate the cell membrane electropermeability, *(ii)* we reveal the intracellular biophysical transport mechanisms of electrotransferred DNA cargo, *(iii)* we present a localized electroporation device where cells are trapped in regions of high electric fields by the flow.

Experiments were performed on mammalian cells to understand how the intracellular cytoskeletal networks are involved in cell membrane electropermeability in chapter 2. We demonstrated that the chemical disruption of actin networks lead to reduced energy barrier of electropore formation. This means, for the same applied trans-membrane voltage, a cell with disrupted actin networks displays enhanced pore formation. Hence, increased permeability of the cell membrane to small impermeable molecules was observed upon actin disruption. This discovery highlights the importance of including the interaction of cytoskeletal and membrane proteins in theoretical electroporation models for obtaining predictive power over biomolecule electrotransfer. Furthermore, our evaluation of temperature-dependent uptake kinetics of DNA binding fluorophores provides a method to directly evaluate the contribution of different (sub)cellular components to the energy barrier of membrane pore formation.

In chapter 3, we electrotransferred DNA fragments of different sizes to various mammalian cell lines and monitored their intracellular transport. We demonstrated that co-existing ergodic and non-ergodic anomalous diffusion govern electrotransferred DNA cargo transport. The anomalous exponent is independent of DNA size, while the apparent diffusion coefficient decreases with DNA size. In contrast, DNA cargo transport anomalous exponent depends on the cancer state of the cell, but the apparent diffusion coefficient is independent. The metastatic cells have a higher propensity to display superdiffusive motion than malignant and benign cells. Our findings provide new insights to develop theoretical models for mass transport during DNA electrotransfer.

We finally developed a localized electroporation device by fabricating a microtrap array inside a microfluidic device in chapter 4. The microtrap array amplifies applied electric fields at the trap apertures. When cells are supplied to this device, they are trapped at high electric fields. We used numerical calculations to prove that our device enables localized electroporation. These simulations will allow the rational design of localized electroporation in the future. The localized electroporation enables us to deliver small molecules and protein-encoding plasmids without compromising cell viability. The insulating PDMS pillars shield a significant part of the cell membrane from the applied electric fields. Furthermore, our device requires much lower voltages to electroporate cells than bulk electroporation due to the concentrated electric fields at the microtrap

apertures. Our device is a proof of concept towards a simple continuous high throughput electroporation.

# SAMENVATTING

Het afleveren van biomoleculen met behulp van gepulseerde elektrische velden of elektrotransfer heeft verscheidene toepassingen, denk hierbij aan biomedische engineering, bioproces engineering en genomische engineering. Wanneer een cel geplaatst wordt in een elektrisch veld katalyseert de geïnduceerde transmembraanspanning de formatie van poriën in het celmembraan. Dit maakt de levering van normaal gesproken celmembraan ondoordringbare moleculen aan de cel mogelijk. Ondanks het vele gebruik van deze techniek is er nog geen biofysisch begrip van elektrotransfer op subcellulair niveau en ook geen vorm van elektroporatie als een techniek met high-throughput en high-efficiency.

In dit proefschrift, *i* ontrafelen we hoe actinenetwerken de elektropermeabiliteit van een celmembraan regelen, *ii* we onthullen de werking van intracellulaire biofysische transportmechanismen van geëlektroforeerde DNA ladingen, *iii* en presenteren we een lokaal-elektroporatie toestel waarbij cellen worden vastgehouden in regio's met hogere elektrische velden met behulp van spanning.

De experimenten werden uitgevoerd op zoogdiercellen om op deze manier in te zien hoe de intracellulaire cytoskeletnetwerken betrokken zijn bij de elektropermeabiliteit van het celmembraan in hoofdstuk 2. We toonden aan dat chemische verstoring van actinenetwerken leidt tot een lagere energiebehoefte bij het vormen van elektroporiën. Dit betekent dat bij eenzelfde toegepaste transmembraanspanning een cel met verstoorde actinenetwerken verhoogde poriënvorming vertoont. Vandaar dat er een verhoogde permeabiliteit van het celmembraan voor normaliter ondoordringbare moleculen werd waargenomen bij actineverstoringen. Deze ontdekking toont het belang van het opnemen van interacties tussen het cytoskelet en membraaneiwiitten in theoretische elektroporatiemodellen voor het voorspellen van de benodigde vermogen voor de elektrotransfer van biomoleculen. Verder biedt onze beschouwing van temperatuurafhankelijke opnamekinetiek van DNA bindende fluorforen een methode aan om de bijdrage van verschillende (sub)cellulaire componenten aan de energiebarrière van membraanporievorming direct te kunnen inzien.

In hoofdstuk 3 hebben we DNA-fragmenten van verschillende grootte getransporteerd naar verschillende zoogdiercellijnen door middel van elektroporatie en elektrooverdracht, hierbij werden deze DNA fragmenten gemonitord. We toonden aan dat er tegelijkertijd sprake is van ergodische en niet-ergodische anomale diffusie bij het transport van de DNA-fragmenten. De anomale exponent is onafhankelijk van het DNA grootte terwijl de schijnbare diffusiecoëfficiënt afneemt naarmate de DNA-fragmenten groter worden. Daarentegen hangt de anomale exponent van het DNA-transport af van de 'kanker-staat' van de cel, waarbij de schijnbare diffusie coëfficiënt onafhankelijk is van deze. De metastatische cellen hebben een grotere neiging om superdiffusieve bewegingen te vertonen in vergelijking met andere kwaadaardige- en goedaardige cellen. Onze bevindingen geven nieuwe inzichten voor het ontwikkelen van theoretische modellen voor massatransport van moleculen tijdens DNA-elektrotransport.

Als laatste hebben we een elektroporatie apparaat ontwikkeld voor specifieke lokale elektroporatie in cellen, hiervoor is een micro-elektrode reeks (microtrap) in een micro-

fluidisch apparaat geplaatst in hoofdstuk 4. Deze microtrap versterkt toegepaste elektrische velden op de openingen van de ‘val’. Als cellen worden toegevoegd aan dit apparaat worden ze gevangen door deze toegepaste elektrische velden. We hebben numerieke berekeningen gebruikt om aan te tonen dat ons apparaat gelokaliseerde elektroporatie mogelijk maakt. Dankzij deze simulaties is het in de toekomst mogelijk om apparaten voor specifieke en lokale elektroporatie te ontwikkelen. Lokale elektroporatie stelt ons namelijk in staat om kleine moleculen en eiwitcoderende plasmiden af te leveren in cellen zonder de levensvatbaarheid van deze cellen aan te tasten. De isolerende PDMS-pijlers schermen een aanzienlijk deel van het celmembraan af van de elektrische velden waardoor het membraan op specifieke lokale plekken permeabel wordt. Bovendien vereist ons apparaat een veel lagere spanning om de cellen te elektroporeren in tegenstelling tot massa-elektroporatie dankzij de geconcentreerde elektrische velden bij alleen de openingen van de microtrap. Ons apparaat is een ‘proof of concept’ in de richting van versimpelde en high-throughput elektroporatie.

# 1

## INTRODUCTION AND OVERVIEW

Safe and controlled delivery of exogenous cargo to living cells is of importance for biomedical and bio-engineering applications such as chemotherapy, gene therapy/editing, vaccination. To do so, the cargo should translocate across the cell membrane which protects the intracellular contents from the extracellular environment [1–3]. Pulsed electric fields allows us to deliver naked exogenous (bio)-molecules which are otherwise impermeable to the cell membrane by transiently permeabilizing the cell membrane [4–6]. The process of permeabilizing cell membrane using pulsed electric field is commonly referred to as electroporation<sup>1</sup> or electropermeabilization. The process of using pulsed electric fields to transfer an exogenous (bio)-molecule from the extracellular environment to intracellular environment is called electrotransfer.

(Bio)-molecules with sizes ranging from 1 nm (small molecules) to ~ 100 nm (plasmid DNA) can be electrotransferred to a variety of mammalian cell types ranging from cancer cells to immune cells [3]. For instance, potency of molecules with anticancer properties such as calcium (~ 0.2 nm) [7–9], cisplatin (~ 0.6 nm) [10, 11] and bleomycin (~ 2 nm) [12, 13] can be enhanced significantly by electrotransfer both in vitro and in vivo. This effect is utilized for cancer treatment using electro-chemotherapy [14–16]. Electrotransfer of cas9 ribonucleoproteins (> 10 nm) has been successfully employed for gene editing in therapeutically relevant cells such as human T cells and induced pluripotent stem cells [17–19]. Similarly, successful gene expression has been demonstrated through electrotransfer of nucleic acids such as RNA (~ 10 nm) and plasmid DNA (size of a 5000 bp plasmid is ~ 100 nm) encoding genes for various proteins such as fluorescent proteins [20, 21], tumor antigens [21], chimeric antigen receptors [22, 23], viral oncoproteins [24], and viral glycoproteins in the spike assembly [25, 26]. The wide range of effects and functionality that can be introduced to different cells by electrotransfer of (bio)-molecules (with different sizes) makes it an indispensable tool in basic cell research, bio-manufacturing and therapeutic applications. Despite its technical simplicity and wide applicability, the extensive range of parameters (for eg : electric pulse parameters such as electric field strength, pulse duration, and number of pulses, a variety of cell types and cargo types) makes optimisation of (bio)-molecule electrotransfer difficult.

---

<sup>1</sup>The term electroporation was coined by Neumann and colleagues in 1982 in their article to explain enhanced penetration of foreign DNA into living cells in the presence of electric fields.



In this dissertation, following scientific research questions that pertain to electrotransfer are answered as individual chapters:

1. Can the cytoskeleton influence the cell membrane permeability during electroporation? (Chapter 2)
2. What is the influence of DNA size and cell type on the intracellular electrotransferred DNA cargo transport? (Chapter 3)

The following technological development is also introduced in this dissertation:

1. A lab on a chip device to perform localized electroporation in which the cells are hydrodynamically directed to and trapped in regions of high electric field strength is fabricated. (Chapter 4)

A brief background on the response of living cells to electric fields and the research gaps which are addressed in this dissertation is provided in the following sections.

## 1.1. RESPONSE OF LIVING CELLS TO ELECTRIC FIELDS

Living cell membranes display enhanced permeability to several (bio)-molecules when placed in externally applied pulsed electric fields. While several explanations for the (electro)-permeability of cell membranes were proposed, broad consensus today is that creation of aqueous (electro)-pores in the cell membranes lead to the enhanced permeability as schematically depicted in Fig. 1.1(a) [27–34]. These aqueous pores are stochastically created in the cell membrane even in the absence of applied electric fields [35]. Upon application of electric fields, a trans-membrane voltage is developed [36–38] which enhances the rate of formation of the pores in the cell membrane for better thermodynamic stability [29, 32, 39, 40]. The induced transmembrane voltage is dependent on the size of the cell size, shape, position with respect to the applied electric field and applied electric field. The maximum transmembrane voltage is found at the two poles parallel to the applied electric field and minimum at the poles perpendicular to the direction of the electric field [41–45]. A detectable permeability of the cell membrane is observed at locations corresponding to high transmembrane voltage. The increased permeability is detected by enhanced conductivity of the cell membrane or influx/efflux of molecules. Small molecules such as propidium iodide obtain access to the cell from both the poles facing the electrodes as shown in Fig. 1.1(b) [46]. In contrast, large negatively charged molecules such as DNA form DNA membrane complexes on the side of the cell facing the negative electrode upon electrotransfer as shown in Fig. 1.1(c) [47]. Upon removal of the electric fields, the cell membrane discharges and goes back to its impermeable state [37].

### 1.1.1. INDUCED TRANSMEMBRANE VOLTAGE

To estimate the transmembrane voltage, the potential distribution in the intracellular and extracellular space should be estimated by solving the Laplace equation

$$\nabla \cdot [(\sigma_{i,e} + \epsilon_{i,e})\nabla V] = 0 \quad (1.1)$$

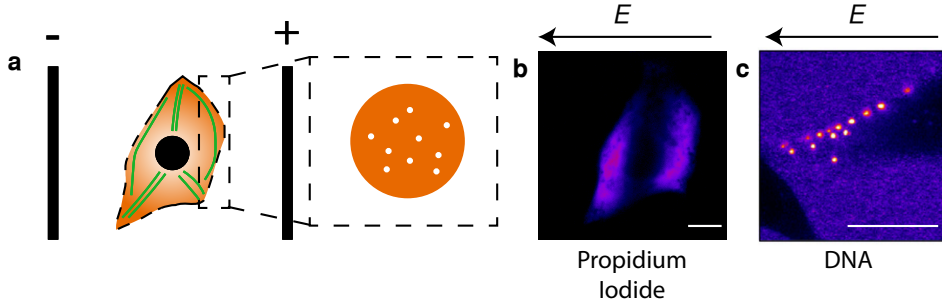


Figure 1.1: (a) Schematic representation of electroporation. A cell placed in an electric field display enhanced permeability (dashed lines) on both poles facing the electrodes. The enhanced permeability is often attributed to the formation of a population of pores (white circles) on the cell membrane as shown in the zoomed in view. Reprinted with permission from [46]. (b) Electrotransfer of propidium iodide (shown in purple) display a symmetric uptake from both the poles facing the electrode. Reprinted with permission from [46]. (c) Electrotransfer of DNA leads to DNA-membrane complex formation on the side of cell facing the cathode (negative electrode). Reprinted with permission from [47]. The scale bars represent 10  $\mu\text{m}$ .

where  $\sigma$  is the electric conductivity,  $\epsilon$  is the dielectric permittivity of the intracellular (subscript i) and extracellular (subscript e) medium. The current density is continuous across the cell membrane, so

$$\mathbf{n} \cdot \mathbf{J} = G_m(V_m - V_{\text{rest}}) + G_{\text{ep}} V_m + C_m \frac{\partial V_m}{\partial t} \quad (1.2)$$

where  $\mathbf{n}$  is the unit vector normal to the membrane surface,  $\mathbf{J}$  is the electric current density across the membrane, where as  $G_m$ ,  $G_{\text{ep}}$ ,  $C_m$  denote the passive membrane conductance, conductance due to formation of pores in the membrane, and membrane capacitance respectively. The transmembrane voltage  $V_m$  corresponds to the difference between the electric potentials on the two sides of the membrane  $V_m = V_i - V_e$  and  $V_{\text{rest}}$  is the resting voltage. For a spherical cell of radius  $R$  with negligible cell membrane conductivity, the induced transmembrane voltage can be estimated analytically as

$$V_m = \frac{3}{2} ER \cos\theta (1 - t/\tau_m) \quad (1.3)$$

where  $E$  is the electric field and  $\tau_m$  is the membrane charging time constant defined by

$$\tau_m = \frac{R\epsilon_m}{2d \frac{\sigma_i \sigma_e}{\sigma_i + \sigma_e} + R\sigma_m} \quad (1.4)$$

and  $d$  is the membrane thickness,  $\sigma_m$  is the membrane conductivity and  $\epsilon_m$  is the membrane permittivity. Once the cell membrane electroporates, the assumption of negligible membrane conductivity is invalid and  $V_m$  has to be evaluated numerically. The main features of the current electroporation models are described below.

### 1.1.2. CURRENT STATE OF THE ART OF ELECTROPORATION MODELS

To describe the cell membrane electroporation various theoretical models were developed [29]. The early models developed for planar lipid bilayer electroporation assume

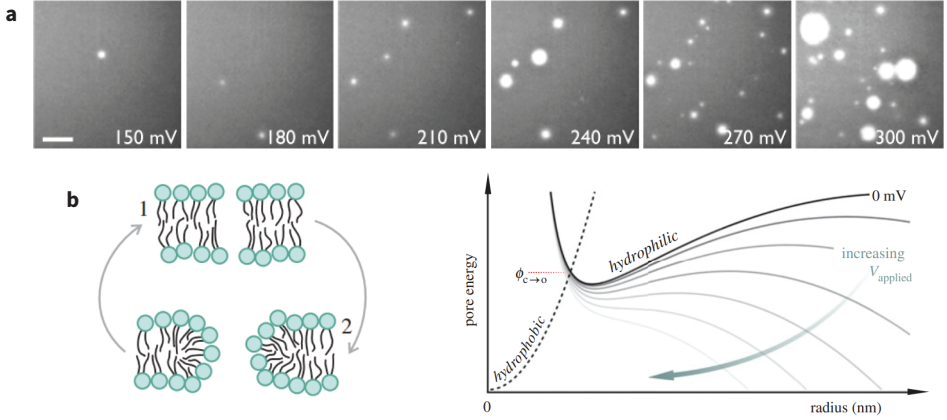


Figure 1.2: (a) Direct visualization of individual electropores in a droplet interface bilayer. With increasing applied voltage (text in white), the number and size of pores increases. Reprinted with permission from [48]. (b) Schematic representation of the theory of electroporation. (left) The pore configurations are depicted in this schematic. Thermal fluctuations cause an intact lipid bilayer to part and form a hydrophobic pore (1). It becomes energetically more favorable to protect the hydrophobic core of the membrane to water at larger radii and then a hydrophilic pore configuration is favored (2). (right) The corresponding free energy of the pore for different pore radii is schematically represented. A free energy barrier  $\phi_{c \rightarrow o}$  governs formation of the hydrophilic pore state. The free energy barrier is lowered by increasing voltage applied ( $V_{\text{applied}}$ ). Reprinted with permissions from [49].

the membrane is permeabilized by the formation of a metastable transient aqueous pore through an unstable hydrophobic pore. The initiation of permeability is considered to be a process occurring within a timescale of few nanoseconds to microseconds [42, 48, 50]. The electroporeabilized cell membrane recovers to its initial impermeable state in a time scale of few seconds to minutes [51–54]. Fig. 1.2(a) shows the pore formation process when an electric field is applied is visualized in droplet interface bilayers under a total internal reflection fluorescence microscope [48]. Theoretically this whole process can be described by a pore energy scheme visually described in Fig. 1.2(b) [49]. The energy associated with the aqueous pore (often referred to as hydrophilic pore) of radius  $r$  is a combination of reduction in the total system energy associated with removing a circular membrane region ( $-\pi r^2 \Gamma$ ) and a gain in the total system energy associated with formation of a new edge ( $2\pi r \gamma$ ) [35]. Here  $\Gamma$  is the energy per unit area of the hydrophilic lipid head groups (also called hydrophilic surface tension) and  $\gamma$  is the edge energy. The net energy change of the membrane associated with formation of or a single pore of radius  $r$  in the absence of a transmembrane voltage is hence,

$$\Delta E = 2\pi r \gamma - \pi r^2 \Gamma \quad (1.5)$$

In the presence of a transmembrane voltage, the specific capacitance of the lipid membrane is replaced with that of the aqueous medium. The net pore energy in presence of transmembrane voltage is

$$\Delta E = 2\pi r \gamma - \pi r^2 \Gamma - BV_m^2 \quad (1.6)$$

The energy of the unstable hydrophobic pore in the presence of a transmembrane voltage is given by

$$\Delta E = 2\pi r d \Gamma_0 \frac{I_1(r/\lambda)}{I_0(r/\lambda)} - BV_m^2 \quad (1.7)$$

where  $I_k$  is the modified Bessel function of the  $k$ th order,  $\Gamma_0$  is the hydrophobic surface tension (from the hydrophobic tails), and  $\lambda$  is the characteristic length of the hydrophobic interactions ( $\sim 1$  nm). The process of initiation and closure of electropores can hence be described as a nucleation process requiring  $\sim 10$ - $45 k_B T$  (where  $k_B$  is the Boltzmann constant) to form.

The flux of pores in the pore radius space is described by

$$\frac{\partial n}{\partial t} = - \frac{\partial J_p}{\partial r_p} \quad (1.8a)$$

$$J_p = -D_p \frac{\partial n}{\partial r_p} - \frac{D_p}{k_B T} n \frac{\partial \Delta E}{\partial r_p} \quad (1.8b)$$

where  $J_p$  denotes the pore flux in the their radii space,  $D_p$  the pore diffusion coefficient,  $k_B$  the Boltzmann constant,  $T$  the temperature, and  $n$  is a pore distribution function in the pore radii space such that  $n dr_p$  corresponds to the number of pores between pore radii  $r_p$  and  $r_p + dr_p$ . This description of electropores, although computationally expensive, provided opportunity to predict when and where pores form in the presence of an applied electric field. Further modifications to equation 1.8 including asymptotic reductions allows us to obtain numerical simulations of electroporation in living cells aiding experimentalists who estimate the response of cells to electric fields [38, 40, 55–57]. By coupling mass transport models to the dynamics of electropores, we can numerically estimate the molecular transport during electroporation [58]. However, kinetics of electrotransfer observed in the numerical simulations deviate from experiments. A careful comparison of numerical simulations with quantitative experimental data shows that current theoretical models overestimates the electrophoretic transport during the pulse, and significantly underestimates the diffusive transport observed after the pulse [59]. Considering current state of the art theories posit that cell membrane electroporation is governed by the membrane mechanical properties, several research groups have begun to explore the effects of different components associated with the cell membrane on biomolecule electrotransfer to resolve this gap [60–63]. In chapter 2 of this dissertation, we study the influence of actin network, a key regulator of cell membrane mechanical properties, on the electrotransfer of small molecules.

### 1.1.3. MOLECULAR TRANSPORT DURING/AFTER ELECTROTRANSFER

Depending on the molecule size and charge one/multiple of the following mechanisms dictate the molecular transport during/after electrotransfer : (i) Passive diffusion (ii) Active transport (iii) Electrophoresis.

#### SMALL MOLECULE TRANSPORT DURING/AFTER ELECTROTRANSFER

Small molecules such as bleomycin and cisplatin display increase potency in their anticancer properties when electrotransferred in vitro and in vivo. Transport of small fluo-

rescent molecules allow us to detect and study electroporation using microscopic techniques. Among the most frequently used dye molecules are nucleic acid binding fluorophores such as propidium iodide, ethidium bromide, and YO-PRO-1 iodide [64]. These are non-permeant molecules which can enter the cell upon electroporation and exhibit a large enhancement in fluorescence by binding to the nucleic acids. This allows us to obtain real time monitoring of electroporation and ability to obtain more insights on the process. To do so we need to first understand their molecular transport during electrotransfer.

Once the cell membrane is electro-permeabilized, small molecules enter the cell through a combination of electrophoresis and diffusion till the cell membrane reseals [54]. Electrophoresis is dominant during the pulse while after the pulse the transport is predominantly diffusive. The relative contribution of electrophoresis and diffusion depends on the charge and the size of the molecule, the pulse duration and the electric field strength [54, 65, 66]. The charge, pulse duration and electric field promote electrophoresis while size of the molecule inversely affects the diffusion coefficient. Theoretically, the transport of charged molecules can be described by the Nernst-Planck equation,

$$\frac{V}{S_p} \frac{dc(t)}{dt} = - \underbrace{\frac{DzF}{RT} c(t)E}_{\text{Electrophoresis}} - \underbrace{D \frac{dc(t)}{dx}}_{\text{Diffusion}} \quad (1.9)$$

where  $V$  is the volume of the cell,  $S_p$  is the permeabilized area,  $c(t)$  is the concentration of the molecule at time  $t$ ,  $D$  is the diffusion coefficient,  $z$  is the electric charge of the molecule,  $F$  is the Faraday constant,  $R$  is the universal gas constant,  $T$  is the absolute temperature, and  $E$  is the applied electric field [54]. For a fast reacting fluorescent molecule such as propidium iodide, equation 1.9 could be simplified to

$$c = \frac{Dc_e A_p \tau}{Vd} (1 - \exp(-t/\tau)), \quad (1.10)$$

where  $d$  is the thickness of the cell membrane,  $D$  is the diffusion coefficient of the molecule in the electroporation buffer, and  $\tau$  is the time scale of resealing of the cell membrane after electroporation. Equation 1.10 is used in chapters 2 and 4 to characterize single cell electroporation to obtain permeabilized area of the cell membrane and the resealing time of the cell membrane.

#### LARGE MOLECULE TRANSPORT DURING/AFTER ELECTROTRANSFER

Electrotransferring large molecules such as nucleic acids has therapeutic and industrial relevance since it opens up possibilities to express functional proteins. During the application of the electric pulses, these molecules primarily are transported as a consequence of their negative charge leading to electrophoresis. Plasmid DNA molecules form DNA membrane complexes at the pole facing the cathode upon electrotransfer to mammalian cells [68–70]. In contrast, siRNA molecules enter the cell without complex formation from the pole facing the cathode [71]. The directionality involved in the molecular entry during the negatively charged DNA and RNA electrotransfer indicates the dominance of electrophoresis as the dominant mechanism of transport during electrotransfer. The formation of DNA-membrane complex formation in living cells is size-dependent and

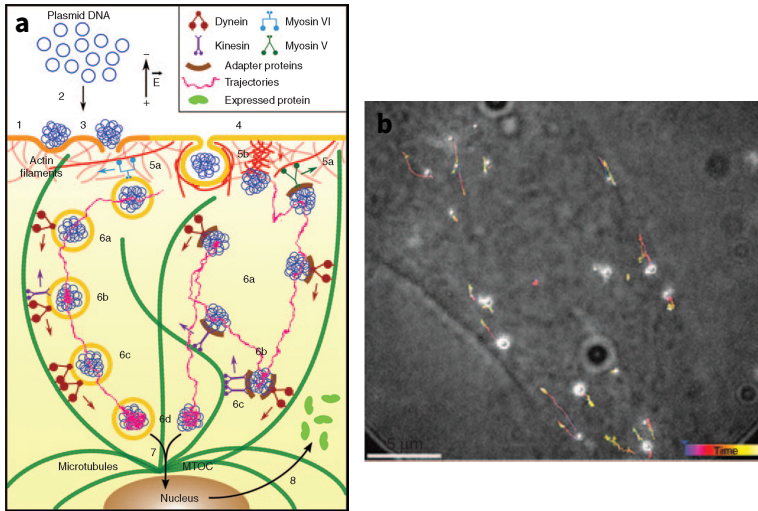


Figure 1.3: (a) Schematic representation of DNA electrotransfer in mammalian cells. When the cell is exposed to electric field, the cell membrane is permeabilized (1). The DNA is then electrophoretically pushed onto the membrane side facing the cathode (2). DNA forms DNA membrane complexes (3). Subsequent internalization of the DNA takes place through endocytosis (4). (5,6) DNA crosses the cytoplasm and move toward the nucleus. (b) Direct visualization of fluorescently labelled DNA (white spots) and their trajectories inside a Chinese Hamster Ovary cell. Figure reprinted with permission from [67]

occurs for DNA sizes above 25 bp [72]. Such complex formation was not observed in lipid vesicles which is the simplest model to mimic the cell membrane up to 20,000 bp DNA [47].

To reach the nucleus, the delivered DNA-membrane complexes should then be transported through the cytoplasm. At this stage, an active cellular process known as endocytosis is involved as shown in Fig. 1.3 [67, 70, 73]. Disruption of cytoskeletal components such as actin cytoskeleton and microfilaments in CHO cells reduced the gene expression during plasmid DNA electrotransfer [74]. Direct visualization and intracellular tracking of single plasmid DNA cargo delivered by electrotransfer showed the presence of *fast* active transport [67]. Inhibition of endocytotic pathways before electrotransfer by knocking down expression of clathrin heavy chain and dynamin II resulted in a significant decrease in transfection efficiency indicating the involvement of endocytosis in the DNA cargo transport [75]. Further investigation using endocytic markers demonstrated that ~ 50% of plasmid DNA is internalized by caveolin/raft-mediated endocytosis, ~ 25 % by clathrin-mediated endocytosis, and ~ 25 % through macropinocytosis. The use of endocytic inhibitors led to reduced gene expression. Furthermore, electrotransferred DNA cargo colocalized with endosomal markers for early endosomes, late endosomes, recycling endosomes, and lysosomes [73]. The presence of caveolae- and clathrin-mediated endocytosis, macropinocytosis, and the clathrin-independent carrier pathways in intracellular electrotransferred DNA cargo transport were demonstrated through ultrastructural analysis of immunoelectron microscopy images [76].

The increased clarity of the pathways involved in the cargo transport has aided in

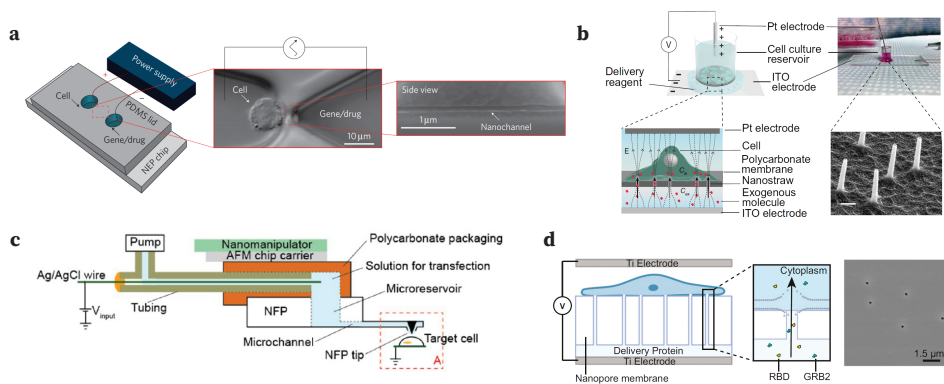


Figure 1.4: Examples of different localized electroporation systems. (a) Nanochannel electroporation system in which a nanochannel connects two microfluidic chambers containing the target cell and the drug respectively in a PDMS device. Figure reprinted with permission from [80]. (b) Nanostraw electroporation device in which cells are plated on to a polycarbonate membrane containing nanostraws through which target molecules are delivered. Figure reprinted with permission from [81]. (c) Nanofountain electroporation device in which an AFM chip carrier is used to deliver the target molecule through localized electroporation, Figure reprinted with permission from [82]. (d) Nanopore electroporation device in which the cells are plated on a porous membrane through which the target molecules are delivered. Figure reprinted with permission from [83]

development of protocols which report a higher transfection efficiency. For instance, usage of bipolar oscillating electric pulses to deliver DNA to both poles of the cells increased the transfection efficiency by  $\sim 1.7$ -5.5 fold compared to unipolar square wave and single square pulse, respectively [77]. Treatment of cells with non degradable sugars hinder vesicular trafficking to lysosomes where cargo gets enzymatically degraded, thereby improving efficiency of electrotransfer of variety of large cargos including plasmid DNA, mRNA, and the CRISPR/Cas9 system to human primary T cells [78]. Similarly, strategies to synchronize the cell growth phase such that nuclear envelope breakdown occur before plasmid DNA was electrotransferred were successful in enhancing electrotransfer efficiency [79]. A key gap in our knowledge of large biomolecule electrotransfer is how their transport is dependent on the size of the molecule and the type of the cell to which the molecules are transferred. These gaps are resolved in the chapter 3 of this dissertation.

#### 1.1.4. LOCALIZED ELECTROPORATION

Apart from the properties of the molecule to be delivered and that of the cell itself, another key variable that influences biomolecule electrotransfer is the electric field. Several research groups have identified ways to improve electrotransfer without compromising cell viability by manipulating the electric fields. One way to do so is by using microfabricated structures to localize electric fields so that only a small part of the cell is exposed to voltages that can electroporate the cell [84, 85]. Such localization of electric fields provides better control of the biomolecule electrotransfer than conventional bulk electroporation. Initial methods of localized electroporation were able to deliver biomolecules such as small fluorescent molecules and plasmid DNA to single cells by localizing elec-

tric fields in PDMS nanochannels embedded in a microfluidic chip or nano fountain probes [80, 81, 86–88].

Some of the examples of current localized electroporation devices are shown in Fig. 1.4. In nanochannel electroporation shown in Fig. 1.4(a), the drug to be electrotransferred and the cell are positioned in two separate microfluidic chambers which are connected by a nanochannel [80, 89–92]. The cell is placed in the vicinity of the nanochannel using an optical tweezer. Upon applying the electric field, nanochannel electroporation demonstrated controlled and rapid delivery of the target molecule to the cell. This principle was then extended to improve the throughput by using porous substrates as shown in Fig. 1.4(d) [83, 86–88, 93, 94]. Here the cells are plated onto a porous substrate which separates the cells and the target delivery molecule. A different method to use the substrate on which cells are plated to localize the electric field is to use nano-straws as shown in Fig. 1.4(b). A limitation of both these techniques is that while they are helpful for adherent cells, they require further steps such as centrifugation to attach the cell to the high electric field regions. Another popular design is to use atomic force microscope probes or nanopipettes to precisely deliver molecules to target cells as shown in Fig. 1.4(c) [82, 95–97]. Similar to the other techniques mentioned above, nanoprobe electroporation methods are limited to the batch mode of operation which makes them difficult to scale up.

One method to scale up the localized electroporation is to combine the benefits of the continuous operation mode of flow-through microfluidic devices with localized electroporation. To do this, a proof of concept localized electroporation device is developed and described in chapter 4 where the cells are manipulated to locations of high electric field strength using flow. The device now provides an easy way to perform localized electroporation at a high throughput as the flow in the microfluidic channels directs the cells to high electric field locations without manual intervention.

## REFERENCES

- [1] D. J. Stephens and R. Pepperkok, *The many ways to cross the plasma membrane*, Proceedings of the National Academy of Sciences **98**, 4295 (2001).
- [2] M. P. Stewart, A. Sharei, X. Ding, G. Sahay, R. Langer, and K. F. Jensen, *In vitro and ex vivo strategies for intracellular delivery*, Nature **538**, 183 (2016).
- [3] M. P. Stewart, R. Langer, and K. F. Jensen, *Intracellular delivery by membrane disruption: mechanisms, strategies, and concepts*, Chemical Reviews **118**, 7409 (2018).
- [4] E. Neumann, M. Schaefer-Ridder, Y. Wang, and P. H. Hofschneider, *Gene transfer into mouse lymphoma cells by electroporation in high electric fields*. The EMBO Journal **1**, 841 (1982).
- [5] N. Calvin and P. Hanawalt, *High-efficiency transformation of bacterial cells by electroporation*, Journal of Bacteriology **170**, 2796 (1988).
- [6] M. L. Yarmush, A. Golberg, G. Serša, T. Kotnik, and D. Miklavčič, *Electroporation-based technologies for medicine: principles, applications, and challenges*, Annual Review of Biomedical Engineering **16**, 295 (2014).



- [7] S. K. Frandsen, H. Gissel, P. Hojman, T. Tramm, J. Eriksen, and J. Gehl, *Direct therapeutic applications of calcium electroporation to effectively induce tumor necrosis*, *Cancer Research* **72**, 1336 (2012).
- [8] S. K. Frandsen, M. B. Krüger, U. M. Mangalanathan, T. Tramm, F. Mahmood, I. Novak, and J. Gehl, *Normal and malignant cells exhibit differential responses to calcium electroporation*, *Cancer Research* **77**, 4389 (2017).
- [9] H. Falk, L. Matthiessen, G. Wooler, and J. Gehl, *Calcium electroporation for treatment of cutaneous metastases; a randomized double-blinded phase II study, comparing the effect of calcium electroporation with electrochemotherapy*, *Acta Oncologica* **57**, 311 (2018).
- [10] G. Sersa, B. Stabuc, M. Cemazar, B. Jancar, D. Miklavcic, and Z. Rudolf, *Electrochemotherapy with cisplatin: potentiation of local cisplatin antitumour effectiveness by application of electric pulses in cancer patients*, *European Journal of Cancer* **34**, 1213 (1998).
- [11] A. Vižintin, S. Marković, J. Ščančar, and D. Miklavčič, *Electroporation with nanosecond pulses and bleomycin or cisplatin results in efficient cell kill and low metal release from electrodes*, *Bioelectrochemistry* **140**, 107798 (2021).
- [12] S. Orlowski, J. Belehradek Jr, C. Paoletti, and L. M. Mir, *Transient electropermeabilization of cells in culture: increase of the cytotoxicity of anticancer drugs*, *Biochemical Pharmacology* **37**, 4727 (1988).
- [13] A. Gothelf, L. M. Mir, and J. Gehl, *Electrochemotherapy: results of cancer treatment using enhanced delivery of bleomycin by electroporation*, *Cancer Treatment Reviews* **29**, 371 (2003).
- [14] L. Mir, L. F. Glass, G. Serša, J. Teissie, C. Domenge, D. Miklavčič, M. J. Jaroszeski, S. Orlowski, D. Reintgen, Z. Rudolf, *et al.*, *Effective treatment of cutaneous and subcutaneous malignant tumours by electrochemotherapy*, *British Journal of Cancer* **77**, 2336 (1998).
- [15] M. Marty, G. Sersa, J. R. Garbay, J. Gehl, C. G. Collins, M. Snoj, V. Billard, P. F. Geertsen, J. O. Larkin, D. Miklavcic, *et al.*, *Electrochemotherapy—an easy, highly effective and safe treatment of cutaneous and subcutaneous metastases: Results of ESOPE (European Standard Operating Procedures of Electrochemotherapy) study*, *European Journal of Cancer Supplements* **4**, 3 (2006).
- [16] B. Geboers, H. J. Scheffer, P. M. Graybill, A. H. Ruarus, S. Nieuwenhuizen, R. S. Puijk, P. M. van den Tol, R. V. Davalos, B. Rubinsky, T. D. de Gruijl, *et al.*, *High-voltage electrical pulses in oncology: irreversible electroporation, electrochemotherapy, gene electrotransfer, electrofusion, and electroimmunotherapy*, *Radiology* **295**, 254 (2020).
- [17] K. Schumann, S. Lin, E. Boyer, D. R. Simeonov, M. Subramaniam, R. E. Gate, G. E. Haliburton, J. Y. Chun, J. A. Bluestone, J. A. Doudna, *et al.*, *Generation of knock-in primary human T cells using Cas9 ribonucleoproteins*, *Proceedings of the National Academy of Sciences* **112**, 10437 (2015).

- [18] X. Liang, J. Potter, S. Kumar, Y. Zou, R. Quintanilla, M. Sridharan, J. Carte, W. Chen, N. Roark, S. Ranganathan, *et al.*, *Rapid and highly efficient mammalian cell engineering via Cas9 protein transfection*, *Journal of Biotechnology* **208**, 44 (2015).
- [19] T. L. Roth, C. Puig-Saus, R. Yu, E. Shifrut, J. Carnevale, P. J. Li, J. Hiatt, J. Saco, P. Krystofinski, H. Li, *et al.*, *Reprogramming human T cell function and specificity with non-viral genome targeting*, *Nature* **559**, 405 (2018).
- [20] H. Yokoe and T. Meyer, *Spatial dynamics of GFP-tagged proteins investigated by local fluorescence enhancement*, *Nature Biotechnology* **14**, 1252 (1996).
- [21] V. F. Van Tendeloo, P. Ponsaerts, F. Lardon, G. Nijs, M. Lenjou, C. Van Broeckhoven, D. R. Van Bockstaele, and Z. N. Berneman, *Highly efficient gene delivery by mRNA electroporation in human hematopoietic cells: superiority to lipofection and passive pulsing of mRNA and to electroporation of plasmid cDNA for tumor antigen loading of dendritic cells*, *Blood, The Journal of the American Society of Hematology* **98**, 49 (2001).
- [22] L. Li, L. N. Liu, S. Feller, C. Allen, R. Shivakumar, J. Fratantoni, L. A. Wolfrum, H. Fujisaki, D. Campana, N. Chopas, *et al.*, *Expression of chimeric antigen receptors in natural killer cells with a regulatory-compliant non-viral method*, *Cancer Gene Therapy* **17**, 147 (2010).
- [23] N. Shimasaki, H. Fujisaki, D. Cho, M. Masselli, T. Lockey, P. Eldridge, W. Leung, and D. Campana, *A clinically adaptable method to enhance the cytotoxicity of natural killer cells against B-cell malignancies*, *Cytotherapy* **14**, 830 (2012).
- [24] C. L. Trimble, M. P. Morrow, K. A. Kraynyak, X. Shen, M. Dallas, J. Yan, L. Edwards, R. L. Parker, L. Denny, M. Giffear, *et al.*, *Safety, efficacy, and immunogenicity of vgx-3100, a therapeutic synthetic DNA vaccine targeting human papillomavirus 16 and 18 e6 and e7 proteins for cervical intraepithelial neoplasia 2/3: a randomised, double-blind, placebo-controlled phase 2b trial*, *The Lancet* **386**, 2078 (2015).
- [25] K. Modjarrad, C. C. Roberts, K. T. Mills, A. R. Castellano, K. Paolino, K. Muthumani, E. L. Reuschel, M. L. Robb, T. Racine, M.-d. Oh, *et al.*, *Safety and immunogenicity of an anti-middle east respiratory syndrome coronavirus DNA vaccine: a phase 1, open-label, single-arm, dose-escalation trial*, *The Lancet Infectious Diseases* **19**, 1013 (2019).
- [26] T. R. Smith, A. Patel, S. Ramos, D. Elwood, X. Zhu, J. Yan, E. N. Gary, S. N. Walker, K. Schultheis, M. Purwar, *et al.*, *Immunogenicity of a DNA vaccine candidate for COVID-19*, *Nature Communications* **11**, 1 (2020).
- [27] A. Barnett and J. C. Weaver, *Electroporation: a unified, quantitative theory of reversible electrical breakdown and mechanical rupture in artificial planar bilayer membranes*, *Bioelectrochemistry and Bioenergetics* **25**, 163 (1991).
- [28] S. A. Freeman, M. A. Wang, and J. C. Weaver, *Theory of electroporation of planar bilayer membranes: predictions of the aqueous area, change in capacitance, and pore-pore separation*, *Biophysical Journal* **67**, 42 (1994).

- [29] J. C. Weaver and Y. A. Chizmadzhev, *Theory of electroporation: a review*, *Bioelectrochemistry and Bioenergetics* **41**, 135 (1996).
- [30] K. C. Melikov, V. A. Frolov, A. Shcherbakov, A. V. Samsonov, Y. A. Chizmadzhev, and L. V. Chernomordik, *Voltage-induced nonconductive pre-pores and metastable single pores in unmodified planar lipid bilayer*, *Biophysical Journal* **80**, 1829 (2001).
- [31] J. Teissie and T. Y. Tsong, *Electric field induced transient pores in phospholipid bilayer vesicles*, *Biochemistry* **20**, 1548 (1981).
- [32] R. W. Glaser, S. L. Leikin, L. V. Chernomordik, V. F. Pastushenko, and A. I. Sokirko, *Reversible electrical breakdown of lipid bilayers: formation and evolution of pores*, *Biochimica et Biophysica Acta (BBA)-Biomembranes* **940**, 275 (1988).
- [33] D. P. Tieleman, H. Leontiadou, A. E. Mark, and S.-J. Marrink, *Simulation of pore formation in lipid bilayers by mechanical stress and electric fields*, *Journal of the American Chemical Society* **125**, 6382 (2003).
- [34] M. Tarek, *Membrane electroporation: a molecular dynamics simulation*, *Biophysical Journal* **88**, 4045 (2005).
- [35] J. Litster, *Stability of lipid bilayers and red blood cell membranes*, *Physics Letters A* **53**, 193 (1975).
- [36] T. Kotnik, G. Pucihar, and D. Miklavčič, *Induced transmembrane voltage and its correlation with electroporation-mediated molecular transport*, *The Journal of Membrane Biology* **236**, 3 (2010).
- [37] J. Teissie, M. Golzio, and M. Rols, *Mechanisms of cell membrane electropermeabilization: a minireview of our present (lack of?) knowledge*, *Biochimica et Biophysica Acta (BBA)-General Subjects* **1724**, 270 (2005).
- [38] W. Krassowska and P. D. Filev, *Modeling electroporation in a single cell*, *Biophysical Journal* **92**, 404 (2007).
- [39] I. Abidor, V. Arakelyan, L. Chernomordik, Y. A. Chizmadzhev, V. Pastushenko, and M. Tarasevich, *Electric breakdown of bilayer lipid membranes: I. the main experimental facts and their qualitative discussion*, *Journal of Electroanalytical Chemistry and Interfacial Electrochemistry* **104**, 37 (1979).
- [40] Z. Vasilkoski, A. T. Esser, T. Gowrishankar, and J. C. Weaver, *Membrane electroporation: The absolute rate equation and nanosecond time scale pore creation*, *Physical Review E* **74**, 021904 (2006).
- [41] J. Bernhardt and H. Pauly, *On the generation of potential differences across the membranes of ellipsoidal cells in an alternating electrical field*, *Biophysik* **10**, 89 (1973).
- [42] M. Hibino, H. Itoh, and K. Kinoshita Jr, *Time courses of cell electroporation as revealed by submicrosecond imaging of transmembrane potential*, *Biophysical Journal* **64**, 1789 (1993).

- [43] T. Kotnik and D. Miklavčič, *Analytical description of transmembrane voltage induced by electric fields on spheroidal cells*, Biophysical Journal **79**, 670 (2000).
- [44] B. Valič, M. Golzio, M. Pavlin, A. Schatz, C. Faurie, B. Gabriel, J. Teissié, M.-P. Rols, and D. Miklavčič, *Effect of electric field induced transmembrane potential on spheroidal cells: theory and experiment*, European Biophysics Journal **32**, 519 (2003).
- [45] G. Pucihar, T. Kotnik, B. Valič, and D. Miklavčič, *Numerical determination of transmembrane voltage induced on irregularly shaped cells*, Annals of Biomedical Engineering **34**, 642 (2006).
- [46] A. Muralidharan, L. Rems, M. T. Kreutzer, and P. E. Boukany, *Actin networks regulate the cell membrane permeability during electroporation*, Biochimica et Biophysica Acta (BBA)-Biomembranes **1863**, 183468 (2021).
- [47] S. Sachdev, A. Muralidharan, D. K. Choudhary, D. L. Perrier, L. Rems, M. T. Kreutzer, and P. E. Boukany, *DNA translocation to giant unilamellar vesicles during electroporation is independent of DNA size*, Soft Matter **15**, 9187 (2019).
- [48] J. T. Sengel and M. I. Wallace, *Imaging the dynamics of individual electropores*, Proceedings of the National Academy of Sciences **113**, 5281 (2016).
- [49] J. T. Sengel and M. I. Wallace, *Measuring the potential energy barrier to lipid bilayer electroporation*, Philosophical Transactions of the Royal Society B: Biological Sciences **372**, 20160227 (2017).
- [50] M. Hibino, M. Shigemori, H. Itoh, K. Nagayama, and K. Kinoshita Jr, *Membrane conductance of an electroporated cell analyzed by submicrosecond imaging of transmembrane potential*, Biophysical Journal **59**, 209 (1991).
- [51] E. Neumann, K. Tönsing, S. Kakorin, P. Budde, and J. Frey, *Mechanism of electroporative dye uptake by mouse b cells*, Biophysical Journal **74**, 98 (1998).
- [52] M.-P. Rols and J. Teissié, *Electropermeabilization of mammalian cells to macromolecules: control by pulse duration*, Biophysical Journal **75**, 1415 (1998).
- [53] R. Shirakashi, V. L. Sukhorukov, I. Tanasawa, and U. Zimmermann, *Measurement of the permeability and resealing time constant of the electroporated mammalian cell membranes*, International Journal of Heat and Mass Transfer **47**, 4517 (2004).
- [54] G. Pucihar, T. Kotnik, D. Miklavčič, and J. Teissié, *Kinetics of transmembrane transport of small molecules into electropermeabilized cells*, Biophysical Journal **95**, 2837 (2008).
- [55] J. C. Neu and W. Krassowska, *Asymptotic model of electroporation*, Physical Review E **59**, 3471 (1999).
- [56] K. A. DeBruin and W. Krassowska, *Modeling electroporation in a single cell. i. effects of field strength and rest potential*, Biophysical Journal **77**, 1213 (1999).

- [57] K. A. DeBruin and W. Krassowska, *Modeling electroporation in a single cell. ii. effects of ionic concentrations*, Biophysical Journal **77**, 1225 (1999).
- [58] K. C. Smith, *A unified model of electroporation and molecular transport*, Ph.D. thesis, Massachusetts Institute of Technology (2011).
- [59] M. Scuderi, J. Dermol-Černe, A. Muralidharan, P. Boukany, and L. Rems, *The current cell electroporation models should be improved to assess the associated molecular transport*, Manuscript under preparation (2022).
- [60] R. L. Knorr, M. Staykova, R. S. Gracià, and R. Dimova, *Wrinkling and electroporation of giant vesicles in the gel phase*, Soft Matter **6**, 1990 (2010).
- [61] I. van Uitert, S. Le Gac, and A. van den Berg, *The influence of different membrane components on the electrical stability of bilayer lipid membranes*, Biochimica et Biophysica Acta (BBA)-Biomembranes **1798**, 21 (2010).
- [62] D. L. Perrier, L. Rems, and P. E. Boukany, *Lipid vesicles in pulsed electric fields: fundamental principles of the membrane response and its biomedical applications*, Advances in Colloid and Interface Science **249**, 248 (2017).
- [63] D. L. Perrier, A. Vahid, V. Kathavi, L. Stam, L. Rems, Y. Mulla, A. Muralidharan, G. H. Koenderink, M. T. Kreuzer, and P. E. Boukany, *Response of an actin network in vesicles under electric pulses*, Scientific Reports **9**, 8151 (2019).
- [64] T. B. Napotnik and D. Miklavčič, *In vitro electroporation detection methods—an overview*, Bioelectrochemistry **120**, 166 (2018).
- [65] P. J. Canatella, J. F. Karr, J. A. Petros, and M. R. Prausnitz, *Quantitative study of electroporation-mediated molecular uptake and cell viability*, Biophysical Journal **80**, 755 (2001).
- [66] M. Puc, T. Kotnik, L. M. Mir, and D. Miklavčič, *Quantitative model of small molecules uptake after in vitro cell electropermeabilization*, Bioelectrochemistry **60**, 1 (2003).
- [67] C. Rosazza, A. Buntz, T. Rieß, D. Wöll, A. Zumbusch, and M.-P. Rols, *Intracellular tracking of single-plasmid DNA particles after delivery by electroporation*, Molecular Therapy **21**, 2217 (2013).
- [68] M. Golzio, J. Teissié, and M.-P. Rols, *Direct visualization at the single-cell level of electrically mediated gene delivery*, Proceedings of the National Academy of Sciences **99**, 1292 (2002).
- [69] C. Faurie, M. Rebersek, M. Golzio, M. Kanduser, J.-M. Escoffre, M. Pavlin, J. Teissie, D. Miklavcic, and M.-P. Rols, *Electro-mediated gene transfer and expression are controlled by the life-time of DNA/membrane complex formation*, The Journal of Gene Medicine **12**, 117 (2010).

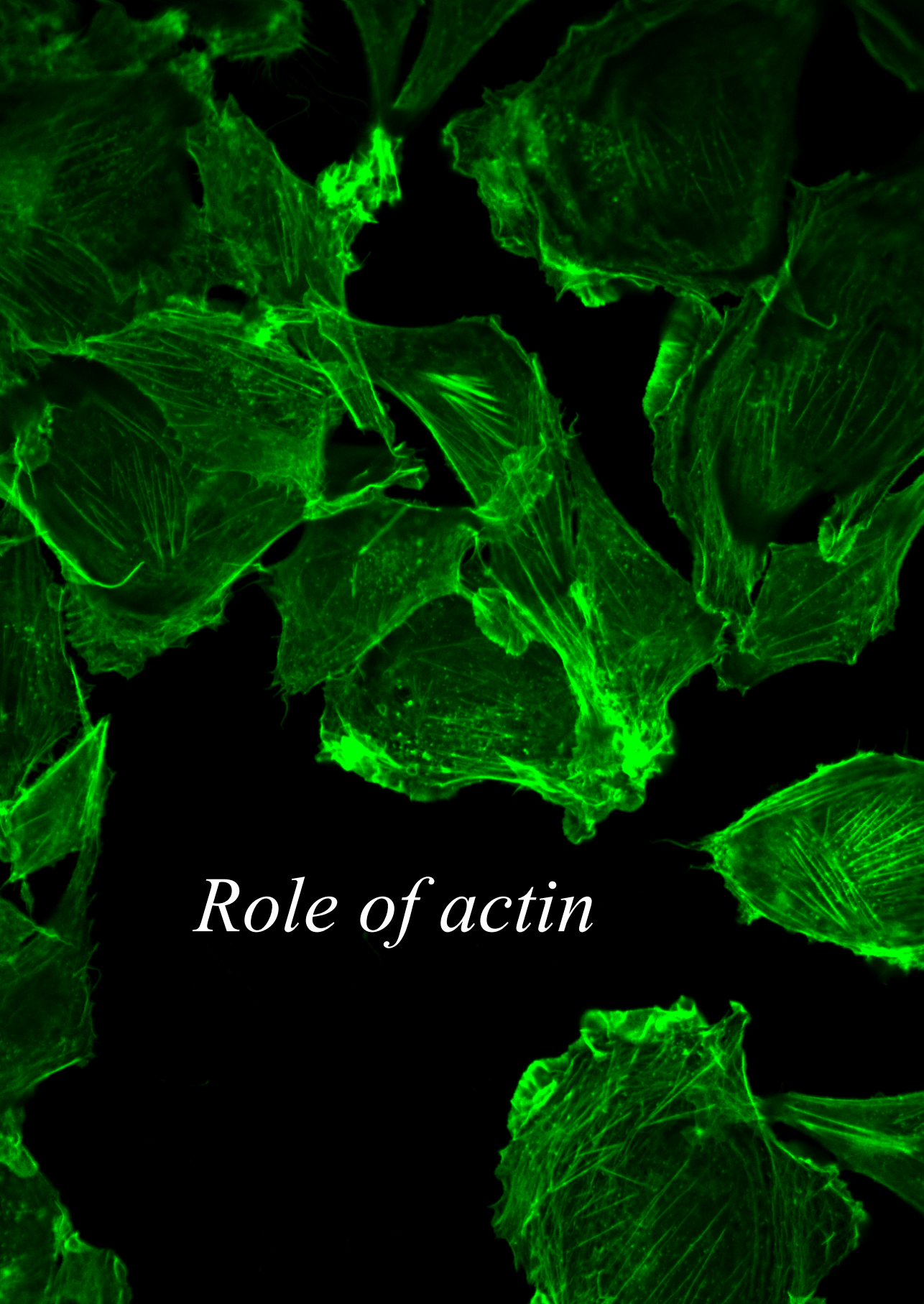
- [70] M. Wu and F. Yuan, *Membrane binding of plasmid DNA and endocytic pathways are involved in electrotransfection of mammalian cells*, *PLoS One* **6**, e20923 (2011).
- [71] A. Paganin-Gioanni, E. Bellard, J.-M. Escoffre, M.-P. Rols, J. Teissié, and M. Golzio, *Direct visualization at the single-cell level of siRNA electrotransfer into cancer cells*, *Proceedings of the National Academy of Sciences* **108**, 10443 (2011).
- [72] S. Sachdev, S. F. Moreira, Y. Keehnen, L. Rems, M. T. Kreutzer, and P. E. Boukany, *DNA-membrane complex formation during electroporation is DNA size-dependent*, *Biochimica et Biophysica Acta (BBA)-Biomembranes* **1862**, 183089 (2020).
- [73] C. Rosazza, H. Deschout, A. Buntz, K. Braeckmans, M.-P. Rols, and A. Zumbusch, *Endocytosis and endosomal trafficking of DNA after gene electrotransfer in vitro*, *Molecular Therapy-Nucleic Acids* **5**, e286 (2016).
- [74] C. Rosazza, J.-M. Escoffre, A. Zumbusch, and M.-P. Rols, *The actin cytoskeleton has an active role in the electrotransfer of plasmid DNA in mammalian cells*, *Molecular Therapy* **19**, 913 (2011).
- [75] C.-C. Chang, M. Wu, and F. Yuan, *Role of specific endocytic pathways in electrotransfection of cells*, *Molecular Therapy-Methods & Clinical Development* **1**, 14058 (2014).
- [76] L. Wang, S. E. Miller, and F. Yuan, *Ultrastructural analysis of vesicular transport in electrotransfection*, *Microscopy and Microanalysis* **24**, 553 (2018).
- [77] E. Tekle, R. D. Astumian, and P. B. Chock, *Electroporation by using bipolar oscillating electric field: an improved method for DNA transfection of NIH 3T3 cells*. *Proceedings of the National Academy of Sciences* **88**, 4230 (1991).
- [78] M. Mao, C.-C. Chang, A. Pickar-Oliver, L. D. Cervia, L. Wang, J. Ji, P. B. Liton, C. A. Gersbach, and F. Yuan, *Redirecting vesicular transport to improve nonviral delivery of molecular cargo*, *Advanced Biosystems* **4**, 2000059 (2020).
- [79] L. D. Cervia, C.-C. Chang, L. Wang, M. Mao, and F. Yuan, *Enhancing electrotransfection efficiency through improvement in nuclear entry of plasmid DNA*, *Molecular Therapy-Nucleic Acids* **11**, 263 (2018).
- [80] P. E. Boukany, A. Morss, W.-c. Liao, B. Henslee, H. Jung, X. Zhang, B. Yu, X. Wang, Y. Wu, L. Li, *et al.*, *Nanochannel electroporation delivers precise amounts of biomolecules into living cells*, *Nature Nanotechnology* **6**, 747 (2011).
- [81] Y. Cao, H. Chen, R. Qiu, M. Hanna, E. Ma, M. Hjort, A. Zhang, R. Lewis, J. Wu, and N. Melosh, *Universal intracellular biomolecule delivery with precise dosage control*, *Science Advances* **4**, eaat8131 (2018).
- [82] W. Kang, F. Yavari, M. Minary-Jolandan, J. P. Giraldo-Vela, A. Safi, R. L. McNaughton, V. Parpoil, and H. D. Espinosa, *Nanofountain probe electroporation (nfp-e) of single cells*, *Nano Letters* **13**, 2448 (2013).

- [83] Z. Chen, Y. Cao, C.-W. Lin, S. Alvarez, D. Oh, P. Yang, and J. T. Groves, *Nanopore-mediated protein delivery enabling three-color single-molecule tracking in living cells*, Proceedings of the National Academy of Sciences **118** (2021).
- [84] T. Geng and C. Lu, *Microfluidic electroporation for cellular analysis and delivery*, Lab on a Chip **13**, 3803 (2013).
- [85] J. Brooks, G. Minnick, P. Mukherjee, A. Jaber, L. Chang, H. D. Espinosa, and R. Yang, *High throughput and highly controllable methods for in vitro intracellular delivery*, Small **16**, 2004917 (2020).
- [86] P. Mukherjee, S. S. P. Nathangari, J. A. Kessler, and H. D. Espinosa, *Combined numerical and experimental investigation of localized electroporation-based cell transfection and sampling*, ACS Nano **12**, 12118 (2018).
- [87] W. Kang, R. L. McNaughton, and H. D. Espinosa, *Micro- and nanoscale technologies for delivery into adherent cells*, Trends in Biotechnology **34**, 665 (2016).
- [88] Y. Cao, E. Ma, S. Cestellos-Blanco, B. Zhang, R. Qiu, Y. Su, J. A. Doudna, and P. Yang, *Nontoxic nanopore electroporation for effective intracellular delivery of biological macromolecules*, Proceedings of the National Academy of Sciences **116**, 7899 (2019).
- [89] P. E. Boukany, Y. Wu, X. Zhao, K. J. Kwak, P. J. Glazer, K. Leong, and L. J. Lee, *Nonendocytic delivery of lipoplex nanoparticles into living cells using nanochannel electroporation*, Advanced Healthcare Materials **3**, 682 (2014).
- [90] X. Zhao, X. Huang, X. Wang, Y. Wu, A.-K. Einfeld, S. Schwind, D. Gallego-Perez, P. E. Boukany, G. I. Marcucci, and L. J. Lee, *Nanochannel electroporation as a platform for living cell interrogation in acute myeloid leukemia*, Advanced Science **2**, 1500111 (2015).
- [91] K. Gao, L. Li, L. He, K. Hinkle, Y. Wu, J. Ma, L. Chang, X. Zhao, D. G. Perez, S. Eckardt, *et al.*, *Design of a microchannel-nanochannel-microchannel array based nanoelectroporation system for precise gene transfection*, Small **10**, 1015 (2014).
- [92] K. Gao, X. Huang, C.-L. Chiang, X. Wang, L. Chang, P. Boukany, G. Marcucci, R. Lee, and L. J. Lee, *Induced apoptosis investigation in wild-type and flt3-itd acute myeloid leukemia cells by nanochannel electroporation and single-cell qrt-pcr*, Molecular Therapy **24**, 956 (2016).
- [93] L. Chang, P. Bertani, D. Gallego-Perez, Z. Yang, F. Chen, C. Chiang, V. Malkoc, T. Kuang, K. Gao, L. J. Lee, *et al.*, *3d nanochannel electroporation for high-throughput cell transfection with high uniformity and dosage control*, Nanoscale **8**, 243 (2016).
- [94] L. Chang, D. Gallego-Perez, C.-L. Chiang, P. Bertani, T. Kuang, Y. Sheng, F. Chen, Z. Chen, J. Shi, H. Yang, *et al.*, *Controllable large-scale transfection of primary mammalian cardiomyocytes on a nanochannel array platform*, Small **12**, 5971 (2016).

- [95] R. Yang, V. Lemaître, C. Huang, A. Haddadi, R. McNaughton, and H. D. Espinosa, *Monoclonal cell line generation and crispr/cas9 manipulation via single-cell electroporation*, *Small* **14**, 1702495 (2018).
- [96] S. S. P. Nathamgari, N. Pathak, V. Lemaitre, P. Mukherjee, J. J. Muldoon, C.-Y. Peng, T. McGuire, J. N. Leonard, J. A. Kessler, and H. D. Espinosa, *Nanofountain probe electroporation enables versatile single-cell intracellular delivery and investigation of postpulse electropore dynamics*, *Small* **16**, 2002616 (2020).
- [97] J. P. Giraldo-Vela, W. Kang, R. L. McNaughton, X. Zhang, B. M. Wile, A. Tsourkas, G. Bao, and H. D. Espinosa, *Single-cell detection of mrna expression using nanofountain-probe electroporated molecular beacons*, *Small* **11**, 2386 (2015).







*Role of actin*

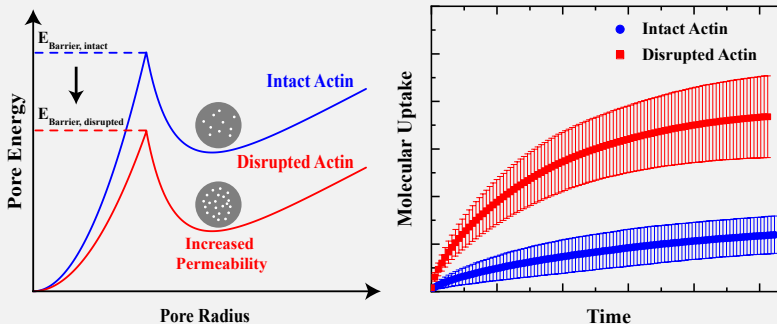


# 2

## ACTIN NETWORKS REGULATE THE CELL MEMBRANE PERMEABILITY DURING ELECTROPORATION

### Highlights

- Electroporative uptake of (bio)molecules increases when actin networks are disrupted.
- Electroporative uptake of (bio)molecules is a temperature dependent process.
- Activation energy barrier of electroporation is reduced when the actin networks are disrupted.
- The observed reduction in activation energy barrier is possibly due to altered cell membrane mechanical properties.



This chapter is published as A. Muralidharan, L. Rems, M. T. Kreutzer, and P.E. Boukany, *Biochimica et Biophysica Acta (BBA) - Biomembranes* (2021) [1].

*Transient physical disruption of cell membranes by electric pulses (or electroporation) has significance in biomedical and biological applications requiring the delivery of exogenous (bio)molecules to living cells. We demonstrate that actin networks regulate the cell membrane permeability during electroporation. Disruption of actin networks increases the uptake of membrane-impermeable molecules such as propidium iodide during electroporation. Our experiments at different temperatures ranging from 11 °C to 37 °C show that molecular uptake during electroporation increases with temperature. Furthermore, by examining the temperature-dependent kinetics of propidium iodide uptake, we infer that the activation energy barrier of electroporation is lowered when the actin networks are disrupted. Our numerical calculations of transmembrane voltage show that the reduced activation energy barrier for the cells with disrupted actin is not a consequence of the changes in transmembrane voltage associated with changes in the cell shape due to the disruption of actin, indicating that this could be due to changes in membrane mechanical properties. Our results suggest that the current theoretical models of electroporation should be advanced further by including the contributions of the cytoskeletal networks on the cell membrane permeability during the delivery of exogenous materials.*

## 2.1. INTRODUCTION

Cell membranes, which are composed of a lipid bilayer with embedded proteins, act as a protective barrier that separates the intracellular components from the extracellular environment. In mammalian cells, the membrane is stabilized by the cytoskeletal network present inside the cell, which is a network of different filamentous biopolymers, including actin fibers and microtubules [2, 3]. While the protective function of the membrane is necessary for the survival of the cell, deliberate permeabilization of the cell membrane to deliver exogenous materials such as small drug molecules, nucleic acids, or proteins is often required for biomedical applications [4]. One of the most common and safest non-viral methods used to transiently increase the cell membrane permeability is the introduction of transient transmembrane pores by subjecting the cell to a pulsed electric field [5, 6]. This process is called electroporation or electropermeabilization, with applications including DNA vaccination, electrochemotherapy, and irreversible electroporation for nonthermal ablation of solid tumors and cardiac muscle ablation [7–13].

Exposing living cells to electric field results in the build-up of a transmembrane voltage ( $V_m$ ) [14, 15], which promotes the nucleation of electropores (or defects) in the cell membrane [16–20]. When the electric field is removed, the membrane discharges resulting in a gradual recovery (resealing) of the cell membrane to its initial impermeable state [14]. Evidence of the existence of the electropores comes primarily from experiments [21–24] and numerical simulations performed on simplified cell membrane systems composed of lipid bilayers [25–27]. Theory and evidence from experiments and numerical simulations have proposed that the initiation and closure of the electropores are temperature-dependent processes, and are governed by activation energy barriers; the reported values of activation energy barriers of pore creation range between 10 and  $45 k_B T$  where  $k_B$  is the Boltzmann constant, and  $T$  is the temperature [17, 18, 22, 27–29]. While the lipid bilayer provides an excellent experimental model for studying electroporation, observations from experiments on living cells are often inconsistent with the experiments on simplified lipid bilayer models [14]. In particular, the measured re-

sealing time of electroporated membranes of cells is in the order of several seconds to minutes [30, 31] while the resealing time of lipid bilayers is considerably shorter (less than one second) [6, 24, 32]. Besides, the electroporation of giant unilamellar vesicles or GUVs leads to the formation of pores in the size range of micrometers in the membrane (also called macropores) whereas pores of such dimensions are not observed in living cells [23, 24, 33].

Since the experiments with simplified lipid bilayer models are insufficient to explain all the observations made in living cells, groups have begun to employ a bottom-up approach by investigating artificial cell models with increasing complexity, including multi-component membranes with lipid phase separation [34–36], and GUVs with incorporated cytoskeleton networks [37]. Experiments with GUVs made of gel phase lipids with mechanical and rheological properties several orders of magnitude higher than those of vesicles made of fluid phase lipids show that the voltage required to form pores in the former is several times higher than the latter [34]. When GUVs made with a mixture of fluid and gel phase lipids were electroporated, the electropores form in the fluid phase [35]. The addition of transmembrane proteins like  $\alpha$ -hemolysin showed up to a four-fold increase in the voltage required to create pores on 1,2-diphytanoyl-sn-glycero-3-phosphocholine (DPhPC) membranes [36]. The addition of cholesterol altered the minimum voltage required to form pores in the DPhPC membrane depending on the concentration of cholesterol added; concentrations below 5% w/w displayed an increase of approximately 25%, followed by almost a 100% decrease in the voltage required for electroporation at higher concentrations [36]. For GUVs incorporated with actin networks, experiments suggest that upon application of an electric pulse the resealing time of the membrane is longer compared to pure lipids vesicles, and macropores that were observed in empty GUVs were absent in vesicles incorporated with actin networks [37].

Similar to experiments with GUVs with encapsulated cytoskeletal networks, experiments on living cells utilizing chemicals that destabilize the cytoskeletal proteins suggest that the cytoskeleton can address some of the mismatches in observations from lipid vesicles and living cells [38, 39]. When Chinese Hamster Ovary (CHO) cells treated with colchicine, a drug that induces microtubule depolymerization, were electroporated (using ten 100  $\mu$ s pulses of 1.8 kV/cm),  $\sim$  10% of the treated cells remain permeable five minutes after application of pulses compared to  $\sim$  60% of the control cells which remain permeable five minutes after delivery of the pulses [38, 39]. Furthermore, the application of multiple 100  $\mu$ s pulses with an amplitude between 100 V/cm and 1200 V/cm to endothelial cells and CHO cells alters the organization of microtubules and actin filaments [40, 41]. Moreover, the application of eight 5 ms pulses of 400 V/cm results in a 40% reduction in Young's modulus of CHO cells, which is associated with a destabilized cytoskeleton [42]. Disruption of actin networks in Jurkat cells using latrunculin results in a reduction of the relative proportion of liquid-ordered compared to the liquid-disordered domains in the membrane [43], and experiments on droplet interface bilayers [21] and molecular dynamics simulations [44] show that the electropores form preferentially in the liquid-disordered phase of the membrane. These studies show that the actin networks can influence the permeability of the cells during electroporation and, as a consequence, the delivery of molecules to cells [45]. Recently, experiments have suggested that the disassembly of actin networks inside cells using cytochalasin results in

reduced uptake of tracer molecules during electroporation [46]. However, this study has utilized multiple electric pulses, which complicates the interpretation of results from a mechanistic perspective to address the pore formation and closure in the cellular membrane with or without the actin networks. That is because the first pulse can increase the permeability of the cell membrane, and the subsequent pulses can begin disrupting the actin network due to electric currents that can flow through the permeabilized cells [37, 47].

Despite several pieces of evidence pointing towards the involvement of cytoskeletal networks in electroporation, the details of how the presence of actin networks influences the permeability of cells during electroporation remain unclear. In this article, we focus on the electroporative uptake of impermeable tracer molecules (propidium iodide) to CHO cells with an intact and disrupted actin filaments when they are exposed to a single electric pulse. We demonstrate that the CHO cells with disrupted actin filaments become more permeable compared to cells with intact actin filaments. By theoretically analyzing our measurements performed at different temperatures, we further demonstrate that the increased membrane permeability in cells with disrupted actin networks can be attributed to reduced activation barrier for pore formation. As such, our combined experimental and numerical results indicate that the presence of actin networks increases the energy barrier of pore formation, possibly due to changes in membrane mechanical properties such as bending modulus.

## 2.2. MATERIALS AND METHODS

### 2.2.1. CELL CULTURE FOR ELECTROPORATION

The Chinese Hamster Ovary cells, CHO-K1 (DSMZ), were grown in T-flasks containing culture medium consisting of Nutrient Mixture Ham F-12 (Sigma Aldrich) supplemented with ~ 10% Fetal Bovine Serum (Sigma Aldrich) and ~ 1% Antibiotic-Antimycotic solution (Gibco). The cells were then incubated at 37 °C with 5% CO<sub>2</sub> and were sub-cultured every two days. Twenty-four hours before the electroporation experiments,  $1 \times 10^4$  cells suspended in 500  $\mu$ l of culture medium were plated in one well of a four-well glass-bottom chambered coverslip ( $\mu$ -slide, Ibidi) with a growth area per well of 2.5 cm<sup>2</sup>.

### 2.2.2. DISRUPTION OF ACTIN NETWORKS BY LATRUNCULIN B TREATMENT

To depolymerize the actin filaments, latrunculin B, a marine toxin which binds to a monomer of actin and depolymerizes the actin filaments was used [48, 49]. 1 mg of latrunculin B (Enzo Life Sciences, molecular weight: 395.5 g/mol) was purchased as a lyophilized solid and was dissolved in DMSO to obtain a stock solution with a concentration of 25 mg/ml or 63 mM. The stock solution was then stored at a temperature of -20 °C. The stock solution was diluted to a concentration of 0.5  $\mu$ M in the culture medium on the day of the experiment. We use a concentration of latrunculin B which can cause severe disruption of the actin filaments in the cells [48]. The measured cell viability after latrunculin B treatment is ~ 100%. The culture medium from the four-well chambered coverslips containing the plated cells was then replaced with 500  $\mu$ l of 0.5  $\mu$ M latrunculin B solution. The chambered coverslips were then placed in the incubator for one hour after which the electroporation experiments were performed.

It was observed that the cells take a spherical morphology as a result of the disruption of the actin filaments compared to their initial flat elongated shapes after the treatment (see Fig. 2.1(a)). The cells were fixed in 500  $\mu\text{l}$  of 3.7% formaldehyde solution in phosphate buffer saline (PBS) for five minutes to visualize the actin filaments. After this, the cells were washed thrice with 500  $\mu\text{l}$  of PBS. 0.1% Triton X-100 in PBS was then used to permeabilize the cells. The cells were again washed thrice with 500  $\mu\text{l}$  of PBS. The actin filaments of the cells were then stained with 200  $\mu\text{l}$  of 50  $\mu\text{g}/\text{ml}$  phalloidin-FITC (Sigma-Aldrich, excitation: 495 nm/emission: 520 nm) solution in PBS by incubating the cells with phalloidin-FITC for 40 minutes at room temperature (22  $^{\circ}\text{C}$ ). The cells were again washed thrice with PBS and imaged under a confocal microscope (Zeiss LSM 710) with a 40x/1.3 oil immersion objective. Fig. 2.1(a) shows that the control cell displays a network of actin stress fibers while they were absent in the cells treated with latrunculin B.

### 2.2.3. ELECTROPORATION OF CHO CELLS

The chambered coverslip containing the CHO cells was taken out of the incubator, and the culture medium was removed from the chamber approximately ten minutes before the experiment. The cells were then washed three times with 500  $\mu\text{l}$  of pulsing buffer (10 mM  $\text{Na}_2\text{HPO}_4/\text{KH}_2\text{PO}_4$ , 1 mM  $\text{MgCl}_2$ , 250 mM sucrose, pH 7.0-7.4). 500  $\mu\text{l}$  of propidium iodide or PI (Invitrogen) of suitable concentration diluted in the pulsing buffer was then added to the chambers. Unless otherwise stated, the concentration of PI used in the experiments is 100  $\mu\text{M}$ . PI (molecular weight: 668 g/mol) is a small fluorescent molecule (excitation: 535 nm/emission: 617 nm), which dissociates into propidium ion and iodide ion when dissolved in water and is impermeable to cells with intact membranes [50]. The ions can enter the cells through the electroporated membrane and bind to the nucleic acids present inside the cell, thereby increasing their fluorescence intensity.

The chambered glass slide was then placed on a Linkham PE94 temperature controlled stage for ten minutes, which allows the cells to attain the required temperature. The temperature inside the chambered glass side was measured using a thermocouple (type K, Ibidi). The temperature of the stage was set to be 4  $^{\circ}\text{C}$ , 22  $^{\circ}\text{C}$ , 35  $^{\circ}\text{C}$ , or 44  $^{\circ}\text{C}$  so that the sample attains a temperature of 11  $^{\circ}\text{C}$ , 22  $^{\circ}\text{C}$ , 28  $^{\circ}\text{C}$ , or 37  $^{\circ}\text{C}$  respectively. For the experiments which require cooling, the stage was supplied with demineralized water at room temperature using an aquarium pump (Eheim). The electric field was applied to the cells using custom made stainless steel electrodes placed parallel to each other with 3 mm spacing, which were inserted inside the imaging chamber such that the electrodes were positioned at the bottom of the coverslip. For this electrode geometry, we calculate the electric field experienced by the cells as the voltage to distance ratio. The electrodes were connected to a pulse generator (BETA tech) to deliver the electric pulses. The imaging chamber was positioned on an inverted fluorescence microscope in such a way that cells which look morphologically healthy were in the field of view. Unless stated otherwise, the applied voltage drop across the electrodes was 240 V, corresponding to an electric field of 800 V/cm. Only one pulse with a duration of 500  $\mu\text{s}$  is applied during all the experiments. This pulsing condition is expected to result in negligible temperature increase ( $\sim 0.1$  K) due to Joule heating (see appendix section 2.H).



### 2.2.4. FLUORESCENCE IMAGING AND ANALYSIS OF PROPIDIUM IODIDE UPTAKE

The fluorescence imaging experiments were performed on an inverted fluorescence microscope (Zeiss Axio-Observer Z1) coupled with an EMCCD camera (Andor ixon3) with a resolution of  $512 \times 512$  pixels. A  $100\times/1.2$  oil immersion objective (Zeiss Acroplan) was used for magnification resulting in a field of view of  $81.92 \times 81.92 \mu\text{m}^2$ . An HXP 120C lighting unit (Zeiss) coupled with a Texas red filter set (excitation: 538 nm/emission: 617 nm) was used as a light source for fluorescence imaging of uptake of PI. Acquisition of a series of images (14 bit) with an exposure time of 20 ms with a 52 ms interval, resulting in a frequency of 19.15 frames per second was initiated approximately ten seconds before the pulse.

## 2.3. RESULTS

### 2.3.1. DISRUPTION OF ACTIN NETWORKS RESULTS IN INCREASED UPTAKE OF PROPIDIUM IODIDE DURING ELECTROPORATION

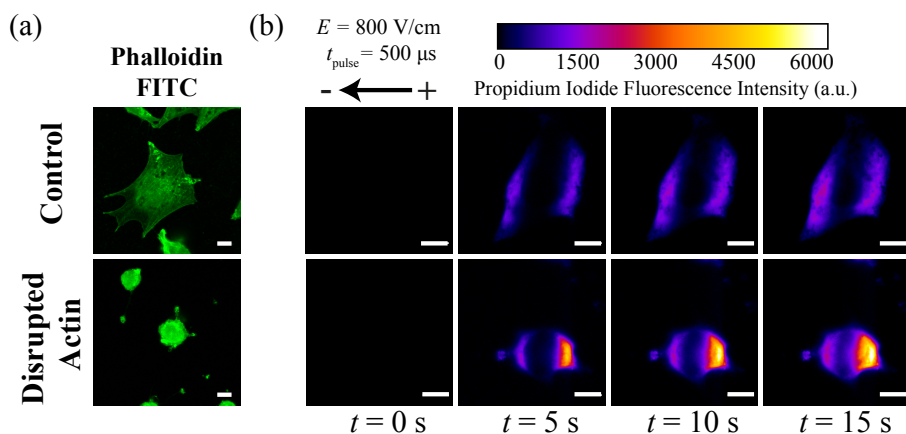


Figure 2.1: (a) Representative confocal images showing the structure of the actin network inside the control cells (top) and the cells treated with  $0.5 \mu\text{M}$  latrunculin B to disrupt actin networks (bottom). The cells were fixed in formaldehyde and stained with phalloidin FITC. The images are obtained by using the same imaging settings. (b) Representative fluorescence intensity profiles (bound propidium signal) for CHO cells with intact actin network (top row), and disrupted actin network using  $0.5 \mu\text{M}$  latrunculin B (bottom row) at different times after electroporation. No intracellular PI fluorescence was detected before electroporation at  $t = 0$  s for both control and treated cells. A single electric pulse with an amplitude of  $800 \text{ V/cm}$  and a pulse duration of  $500 \mu\text{s}$  was applied for these uptake experiments. The experiments are performed at room temperature ( $22^\circ\text{C}$ ). Scale bars represent  $10 \mu\text{m}$ .

To measure the uptake of small molecules to the cells after electroporation, we use a membrane-impermeable molecule, PI, as a marker molecule. Propidium ions emit a strong fluorescence signal when they bind to nucleic acids, which are present inside the cell. Hence, when an electric pulse is applied to the cell in the presence of PI, an increase in fluorescence intensity is observed as a result of transport of the propidium ions to the cell through the permeabilized cell membrane [51]. The uptake of propidium

ions by cells during electroporation for an experiment where a single 500  $\mu\text{s}$  pulse with an amplitude of 800 V/cm is applied at room temperature is displayed in Fig. 2.1(b) (the uptake profiles at lower magnification providing a larger field of view is presented in appendix Fig. 2.11). The transport of propidium ions follows two stages. During the electric pulse, the propidium ions are electrophoretically delivered to the cells from the side facing the positive electrode. After the pulse, the propidium ions continue to diffuse through the permeabilized membrane from both sides of the cell facing the electrodes until the membrane recovers its selective permeability (time scale  $\sim 10$  s) [51, 52]. This results in increased fluorescence intensity at both poles of the cell as seen in Fig. 2.1(b).

The time-series images are analyzed to extract the increase in fluorescence intensity inside the cell with time after the electric pulse is applied using a customized script, coded in Matlab<sup>®</sup>. First, a region of interest is selected by manually outlining the individual cells. The intensity of an image before electroporation is subtracted from all the images to remove the background signal. The sum of the intensity values in the region of interest is then divided by the number of pixels inside the region of interest for each frame to obtain the transient fluorescence intensity profiles ( $I_{\text{Total}}$ ). The time corresponding to zero seconds is defined as the frame in which an increase in fluorescence intensity inside cells is observed with respect to background noise. The transient increase of  $I_{\text{Total}}$  for the control cells and the cells treated with latrunculin B at room temperature are plotted in Fig. 2.2(a). For brevity, we refer to cells treated with latrunculin B either as cells with disrupted actin or as treated cells in the rest of the article. Fig. 2.2(a) shows that the  $I_{\text{Total}}$  is higher for the treated cells compared to the control cells. This indicates that the treated cells take up more PI compared to the control cells. In addition, the fluorescence intensity along the centerline of representative control and treated cell (displayed in inset of Fig. 2.2(b)) parallel to the direction of the electric field is plotted in Fig. 2.2(b). The centerline fluorescence profiles for all the cells studied at this condition is provided in the appendix (Fig. 2.9 and 2.10). Inset from Fig. 2.2(b) shows that while the uptake of PI is symmetric in the control cells, it is asymmetric in the cells with disrupted actin. In the cells with disrupted actin, there is almost a two-times higher fluorescence intensity that is emitted at the pole of the cell facing the positive electrode compared to the pole facing the negative electrode. Mobility of nucleic acids, which are responsible for fluorescence signal emitted when PI enters the cell, is known to increase up to an order of magnitude on the disruption of actin networks inside the cell [53]. The increased fluorescence intensity on the pole facing the anode could be due to the easier migration of the negatively charged nucleic acids inside the treated cells towards the positive electrode when an electric field is applied.

Transport of PI to cells is dependent on the permeabilized area of the cell membrane and the resealing time of the membrane [51]. The membrane becomes permeable in the regions, where the transmembrane voltage exceeds a critical value, and these regions are called “permeabilized areas”. The increased permeability within the permeabilized area is thought to be due to the presence of pores, as shown in Fig. 2.2(c). For brevity, we refer to the sum area of the pores on the membrane as the “pore area” in the rest of the article. Consider a cell of volume  $V$  placed in an electroporation buffer containing propidium ions of concentration  $c_e$  and exposed to an electric field. Upon exposure, the permeability of the cell membrane increases such that the pore area is  $A_{p0}$ . Once the cell

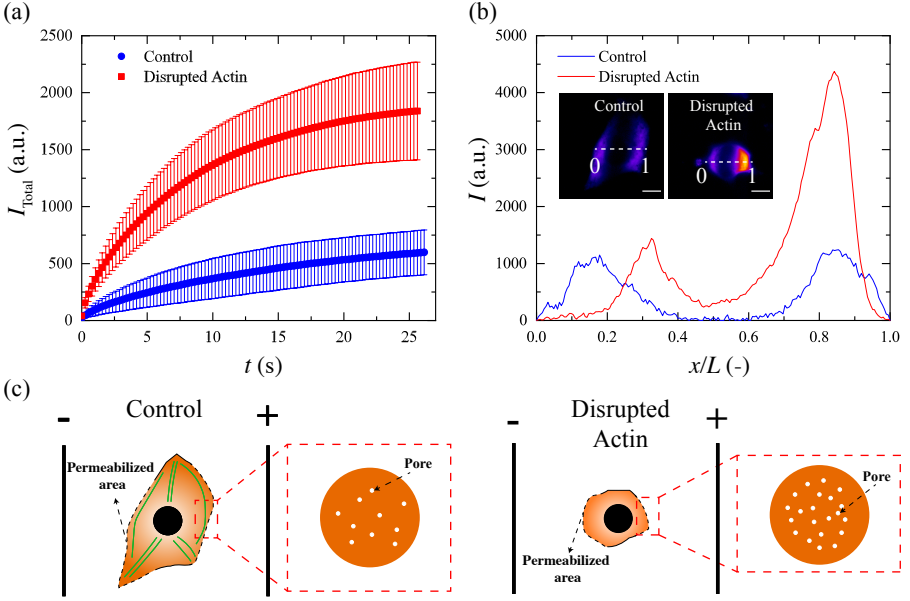


Figure 2.2: (a) Temporal evolution of the total fluorescence intensity divided by the number of pixels in the region of interest both the control cells and the treated cells at room temperature. The total fluorescence intensity is measured as the sum of the fluorescence intensity inside a region of interest defined by the boundary of the cell. The data points represent the average value, and the error bars represent the standard deviation from 5-6 cells. Only one among every fifth data point is shown for improving visibility. (b) A representative plot showing the fluorescence intensity across the centerline (dashed white line in the inset, parallel to the electric field) of the cells shown in the inset at the time corresponding to the resealing time of the cell membrane. The point 0 corresponds to the first point on the cell from the side of the cathode, which emits a fluorescence intensity signal, and 1 corresponds to the last point, which emits a fluorescence intensity signal. One electric pulse of 800 V/cm with a duration of 500  $\mu\text{s}$  is applied to obtain this data. The scale bars represent 10  $\mu\text{m}$ . (c) A schematic showing the difference between permeabilized region (dashed lines) and pores (white circles) present within the permeabilized region.

membrane is permeable, the propidium ions enter the cell and bind to the nucleic acids and form a fluorescent species with the concentration [PIB]. If  $d$  is the thickness of the cell membrane,  $D$  is the diffusion coefficient of propidium ions in the electroporation buffer, and  $\tau$  is the time scale of resealing of the cell membrane, the concentration of bound propidium ions can be expressed as [51, 52, 54]

$$[\text{PIB}] = \frac{Dc_e A_{p0}\tau}{Vd} (1 - \exp(-t/\tau)). \quad (2.1)$$

Assuming that the fluorescence signal emitted by bound propidium ions vary linearly with [PIB] as  $I_{\text{Total}} = m \cdot [\text{PIB}]$ , we obtain  $I_{\text{Total}} = I_{\text{max}}(1 - \exp(-t/\tau))$ . In this expression,  $I_{\text{max}} = (mDc_e A_{p0}\tau)/(Vd)$ ,  $m$  is the proportionality constant that relates the concentration of bound propidium ions to the fluorescence intensity measured by the imaging system, and  $I_{\text{max}}$  is the plateau of fluorescence intensity emitted by the cell after electroporation in the presence of PI. eq. 2.1 is then fitted to the temporal evolution of fluores-

cence intensity obtained from the image analysis using  $lsqcurvefit()$  function in Matlab<sup>®</sup> to obtain  $I_{\max}$  and  $\tau$  as displayed in Fig. 2.13 (appendix). It is observed that the  $I_{\max}$  is  $\sim 695 \pm 237$  a.u. for the control cells while the treated cells display approximately three times higher  $I_{\max}$  of  $\sim 1945 \pm 442$  a.u. The extracted resealing time  $\tau$  is  $\sim 13 \pm 7$  s for the control cells  $\sim 8 \pm 3$  s for the treated cells. An additional parameter of interest is the ratio of  $I_{\max}$  and  $\tau$ , which is given by

$$\frac{I_{\max}}{\tau} = \frac{mDc_e A_{p0}}{Vd}. \quad (2.2)$$

This ratio is directly proportional to the initial pore area on the cell membrane after the electric pulse and the diffusion coefficient of PI through the cell membrane, which are temperature dependent quantities.  $I_{\max}/\tau$  is measured to be  $67 \pm 45$  for the control cells and  $279 \pm 104$  for the treated cells. Assuming that the cells have a similar volume, this indicates that the average pore area is significantly larger ( $\sim 4$  times) for cells with disrupted actin in comparison to control cells. However, Fig. 2.1(b) shows that the propidium ions can enter through a larger part of the cell membrane in the control cells compared to the treated cells. There are three possibilities to explain the higher uptake of PI in the treated cells despite the lower permeabilized portion of the cell membrane: (i) the treated cells have more pores within the permeabilized area than in the control cells leading to higher pore density; (ii) the size of the pores is larger in the treated cells than in the control cells; (iii) or a combination of both.

### 2.3.2. TEMPERATURE-DEPENDENT UPTAKE OF PROPIDIUM IODIDE INTO CHO CELLS WITH INTACT AND DISRUPTED ACTIN NETWORKS

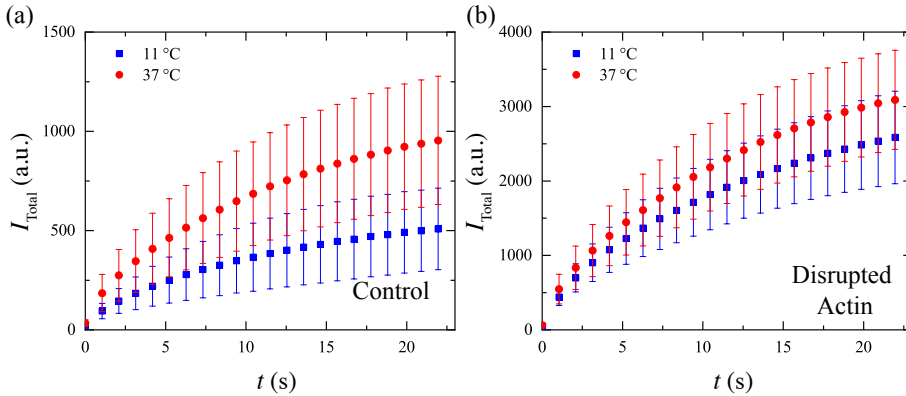


Figure 2.3: Temperature dependence of  $I_{\text{Total}}$  for (a) control cells and (b) cells with disrupted actin. Data for 11°C and 37°C are shown in this figure. Only one among every fifteenth data point of the time series is shown for better clarity of the data. The symbols represent the average value, and the error bars represent the standard deviation over measurements from 4-7 cells. One electric pulse of 800 V/cm with a duration of 500  $\mu\text{s}$  is applied to obtain this data.

One of the most accepted descriptions of the electroporation of cell membranes as a response to the applied electric field is the nucleation theory of electropo-

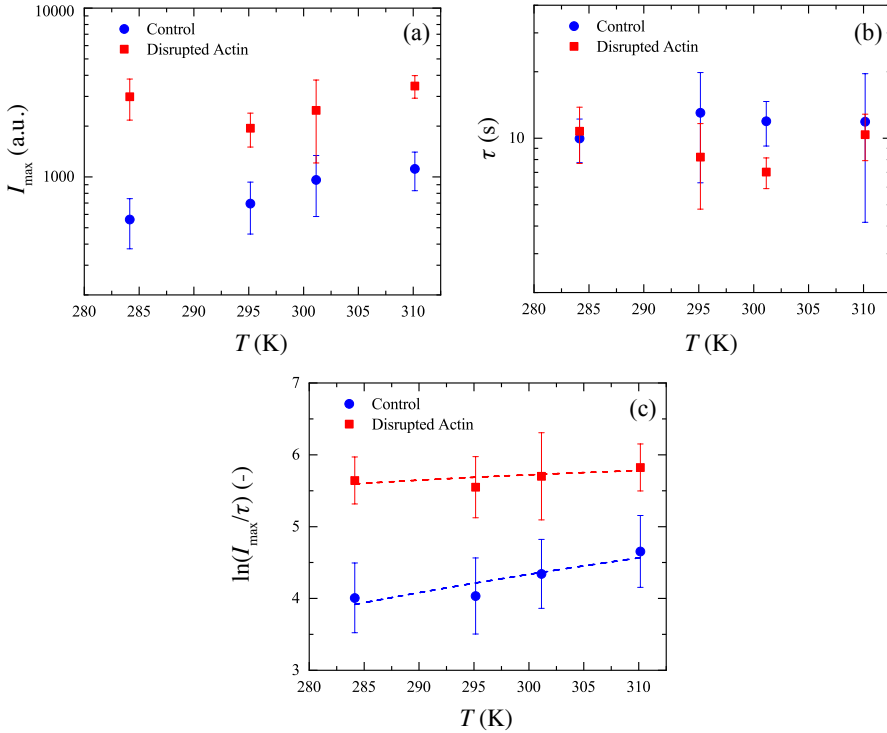


Figure 2.4: (a) Dependence of the plateau fluorescence intensity  $I_{\max}$  on temperature. (b) Dependence of the resealing time,  $\tau$  on temperature. (c) Dependence of  $\ln(I_{\max}/\tau)$  on temperature. The solid symbols represent average value, and the error bars represent standard deviation over 4-7 cells. The dashed lines correspond to the best fit of the experimental data with eq. 2.5. One electric pulse of 800 V/cm with a duration of 500  $\mu$ s is applied to obtain this data.

ration [18]. According to this theory, the rate of formation and closure of transmembrane pores is dependent on the temperature of the cell membrane [18, 22, 27]. The temperature-dependent rate of the creation and closure of the pores are governed by activation energy barriers [17]. Hence, the pore area and the lifetime of permeability of the cell membrane depend on the temperature. An experiment which uses the temperature dependence of the pore area and the lifetime of permeability hence allows us to measure the energy barrier of pore formation [22].

To study the energetics of the electropores and its dependence on the internal architecture of the actin networks, we perform experiments studying the uptake of PI into CHO cells (both control cells and cells treated by latrunculin B) at different temperatures ranging from 11  $^{\circ}$ C to 37  $^{\circ}$ C. We make the following observations from the temperature-dependent PI uptake experiments. As seen in Fig. 2.3(a) and (b), control cells and treated cells display a higher fluorescence signal at 37  $^{\circ}$ C compared to at 11  $^{\circ}$ C, implying more transport of propidium ions at the higher temperature. By fitting the temporal fluorescence intensity data from control cells and treated cells, we obtain  $I_{\max}$  and  $\tau$  at different

temperatures presented in the Fig. 2.4(a) and (b). We found that  $I_{\max}$  increases systematically for the control cells while the increase is less pronounced in the treated cells (see Fig. 2.4(a)). As shown in this figure, the  $I_{\max}$  is almost five times higher at 11 °C while approximately three times higher at 37 °C for cells with disrupted actin compared to the control cells. At the same time, Fig. 2.4(b) shows that  $\tau$  does not have any noticeable dependence on the temperature of the cells.

The higher fluorescence intensity from the treated cells compared to the control cells can be attributed to a higher pore area in the cells with disrupted actin networks after electroporation. The nucleation theory of electroporation describes the formation of the electropores within the membrane. The rate of formation of electropores depends on a nucleation free energy barrier governed by the transition of an intact bilayer to a hydrophilic pore, through an unstable hydrophobic pore configuration [17, 18]. If the effective energy barrier of pore formation within the cell membrane is  $E^*$ , the rate of formation is  $\dot{n}_0 = \nu S/a_0 \exp(-E^*/k_B T)$  where  $k_B$  is the Boltzmann constant,  $\nu$  is the attempt rate frequency,  $S$  is the permeabilized area,  $a_0$  is the area per lipid molecule and  $T$  is the temperature [17, 22]. If the effective area of a single pore is  $a_p$ , and the pores form for a duration  $t_{\text{pore}}$ , the accumulated pore area is

$$A_{p0} = \frac{\nu S}{a_0} \exp(-E^*/k_B T) t_{\text{pore}} a_p. \quad (2.3)$$

Combining the eq. 2.2 with the eq. 2.3, we arrive at,

$$\frac{I_{\max}}{\tau} = \left( \frac{m c_e S a_p t_{\text{pore}}}{V d a_0} \right) \cdot (D \nu) \exp(-E^*/k_B T). \quad (2.4)$$

Taking logarithm on both sides, we arrive at,

$$\ln\left(\frac{I_{\max}}{\tau}\right) = \ln\left(\frac{m c_e S a_p t_{\text{pore}}}{V d a_0}\right) + \ln(D \nu) - \frac{E^*}{k_B T}. \quad (2.5)$$

eq. 2.5 provides us a way to estimate the nucleation barrier for the pore formation within the cell membrane by the dependence of  $\ln(I_{\max}/\tau)$  versus temperature. We demonstrate that  $\ln(I_{\max}/\tau)$  is significantly higher for the cells with disrupted actin compared to the control cells at all the temperatures in Fig. 2.4(c). A second observation is that  $\ln(I_{\max}/\tau)$  increases with temperature for both the control and the cells with disrupted actin. The increase in  $\ln(I_{\max}/\tau)$  with temperature is more pronounced for the control cells compared to the treated cells. This effect indicates that the increase in pore area in the control cells with temperature is higher in comparison to that of the treated cells. Assuming that the duration for which electropores form is independent of the assembly of the actin networks, we infer that the rate of pore formation is higher in the treated cells compared to the control cells. Since the temperature dependence of the diffusion coefficient is independent of the structure of actin networks inside the cells, we attribute the difference in the temperature dependence of  $\ln(I_{\max}/\tau)$  to the differences in the energy barrier of pore formation in the cell membrane for the cells. Based on the temperature dependence of  $\ln(I_{\max}/\tau)$ , we infer that the energy barrier of pore formation for the treated cells is lower than that of control cells. This hypothesis is consistent with the observation that the treated cells have a higher uptake of propidium ions in comparison to

the control cells. We obtain a rough estimate of the energy barriers by fitting the experimental data with eq. 2.5 after assuming diffusion coefficient and attempt rate frequency to be independent of temperature as seen in Fig. 2.4(c). The estimate suggests an energy barrier for pore formation of  $\sim 7 \pm 2 k_B T$  for control cells and  $\sim 2 \pm 1 k_B T$  for the treated cells. Note that the energy barriers are estimated in the presence of an applied electric field.

In addition to the experiments with an applied electric field intensity of 800 V/cm, we also performed the same experiment at lower applied electric fields. For the imaging settings that we use, the fluorescence intensity that we observe at an applied field intensity of 500 V/cm is significantly lower than that at 800 V/cm. However, the fluorescence intensity is not sufficient enough to extract any reliable information through the fitting of the experimental data. Similarly, at an applied electric field of 600 V/cm, despite post pulse diffusion being the primary contributor to the uptake of molecules, a lower uptake is observed compared to the same experiment performed at 800 V/cm. The extracted  $I_{\max}$ ,  $\tau$  and  $I_{\max}/\tau$  for the molecular uptake experiment at different temperatures performed at 600 V/cm are provided in the appendix (Fig. 2.15). Also, similar to the molecular uptake experiments performed at 800 V/cm, cells with disrupted actin show a higher uptake compared to control cells without a notable change in resealing time. The dependence of  $\ln(I_{\max}/\tau)$  on temperature is also similar to that at 800 V/cm, with the control cells exhibiting a stronger dependence of  $\ln(I_{\max}/\tau)$  on temperature compared to the cells with disrupted actin. In summary, the results at 600 V/cm are consistent with the observations at 800 V/cm.

### 2.3.3. EFFECT OF CONCENTRATION OF THE PROPIDIUM IODIDE ON CELLULAR UPTAKE DURING ELECTROPORATION AT ROOM TEMPERATURE

We perform experiments with different concentrations of PI ranging from 50  $\mu\text{M}$  to 125  $\mu\text{M}$  for the control cells and from 25  $\mu\text{M}$  to 100  $\mu\text{M}$  for the treated cells at room temperature (22  $^\circ\text{C}$ ) to study the dependence of PI uptake on the external concentration of PI. These concentrations provide sufficient fluorescence intensity inside the cell during electroporation in comparison to the background noise and do not exceed the saturation value for pixels in the imaging sensor. Fig. 2.5 shows the results of the experiments demonstrating the dependence of the uptake of the propidium ions on the external concentration of PI,  $c_e$ . Fig. 2.5(a) displays that the  $I_{\max}$  increases with concentration for control and treated cells as expected. We also observe that the uptake of PI is significantly higher in the treated cells in comparison to the control cells for the range of the tested concentrations. In other words, it is possible to deliver the same dosage of propidium ions to the treated cells with a lower external concentration of PI compared to the control cells.

The eq. 2.2 states that  $I_{\max}/\tau$  increases linearly with the concentration of PI outside,  $c_e$ . The slope of a plot between  $I_{\max}/\tau$  and  $c_e$  can be determined as

$$\frac{d}{dc_e} \left( \frac{I_{\max}}{\tau} \right) = \frac{mDA_{p0}\tau}{Vd}. \quad (2.6)$$

eq. 2.6 shows that the slope of the plot between  $I_{\max}/\tau$  and  $c_e$  is directly proportional to  $A_{p0}$ . Hence, the dependence of uptake of PI on the external concentration of PI al-

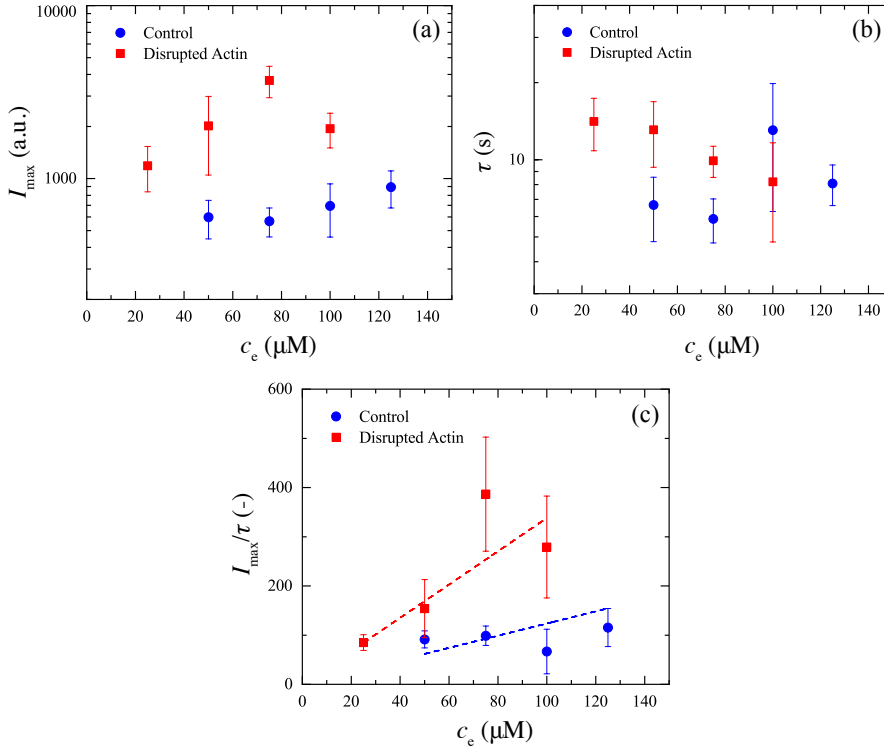


Figure 2.5: (a) Dependence of plateau fluorescence intensity  $I_{\text{max}}$  on  $c_e$ . (b) Dependence of resealing time,  $\tau$  on  $c_e$ . (c) Dependence of  $I_{\text{max}}/\tau$  on  $c_e$ . The solid symbols represent the average value and the error bars represent the standard deviation over 5-8 cells. The dashed lines represent best linear fit of the data with eq. 2.2 used to estimate the right hand side of eq. 2.6. One electric pulse of 800 V/cm with a duration of 500  $\mu\text{s}$  is applied to obtain this data. This data is obtained at room temperature.

allows us to determine the ratio of the pore area between the control and the treated cells. The dependence of  $I_{\text{max}}/\tau$  with  $c_e$  is plotted in Fig. 2.5(c). The plot shows that  $I_{\text{max}}/\tau$  increases with  $c_e$  for both the control and the treated cells. It can be observed that the slope of increase of  $I_{\text{max}}/\tau$  with  $c_e$  is lower for the control cells in comparison to the treated cells as expected from eq. 2.6. The slopes (right hand side of eq. 2.6) are estimated by linear fitting (to eq. 2.2) using OriginPro, after fixing the y-intercept of the fit at zero. The corresponding values for the slope for control cells and cells with disrupted actin are  $1.23 \pm 0.22 \mu\text{M}^{-1}$  and  $3.38 \pm 0.35 \mu\text{M}^{-1}$  respectively. From the ratio of the slopes, it can be inferred that the pore area is  $\sim 2.7$  times higher in cells with disrupted actin in comparison to control cells, reaffirming the inference made in the section 2.3.1 that the estimated pore area can be  $\sim 4$  times higher in cells with disrupted actin compared to control cells.



## 2.4. DISCUSSION

Our results indicate that actin networks are involved in the electropore formation in living cells. Previous experiments have shown that the incorporation of actin network into giant unilamellar vesicles (GUVs) resulted in a higher molecular uptake through the lipid membrane due to the resulting longer resealing time compared to the empty GUVs [37]. In our study, the estimated average resealing time at room temperature of the control cells is  $\sim 60\%$  longer compared to the cells treated with latrunculin B; however, despite their shorter resealing time, the treated cells exhibit more PI uptake. This suggests that the total area of the membrane pores, which allow the transport of the propidium ions, is higher in the treated cells. Since a more substantial part of the cell membrane is electropermeabilized in the control cells compared to the treated cells, this further suggests that a large amount of pore area resides within a smaller permeabilized area for the treated cells.

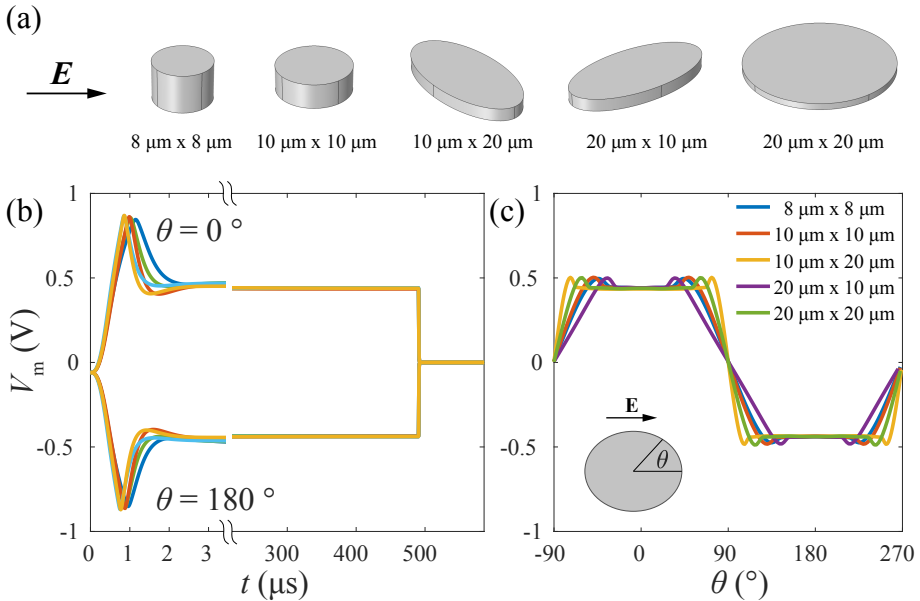


Figure 2.6: Calculations of the induced transmembrane voltage for the cylindrical cells having volumes that mimic our experimental cases. The details of the numerical calculations are provided in the appendix (see section 2.G). (a) 3D representation of the cell geometry considered. (b) Time course of the transmembrane voltage at the anodic and the cathodic pole of the cell (at  $\theta = 0^\circ$  and  $\theta = 180^\circ$ ). (c) Profile of the induced transmembrane voltage along the cell membrane at the end of a  $500 \mu\text{s}$ ,  $800 \text{ V/cm}$  pulse (identical to the experimental conditions).  $\theta$  is the angle between the point on the membrane and the electric field  $E$  (see inset).

The electropermeabilization of the cell membrane is typically described by the formation of metastable pores on the cell membrane, which is facilitated by the transmembrane voltage induced by the applied electric field [18]. Analytical calculations for spheroidal cells show that the induced  $V_m$  is a function of the cell size, the shape, and the orientation, and reaches higher absolute values in cells, which are larger and/or

elongated having their major axis aligned with the direction of the electric field [55, 56]. The permeabilized area is hence expected to be higher in the control cells, which are larger and elongated, compared to the more spherical treated cells. However, we observe higher PI uptake in the treated cells. Higher uptake thus cannot be attributed to a larger permeabilized area or longer resealing time but a higher number and/or size of the pores within the permeabilized region. The latter can be attributed to a higher rate of pore creation in the treated cells, as detailed below.

According to the nucleation theory, the rate of the pore formation depends on the number of possible pore nucleation sites, the energy barrier of pore formation, and the temperature. Our experiments at different temperatures between 11 °C and 37 °C indicate that the disruption of actin filament reduces the energy barrier of pore formation, thereby increasing the rate of pore formation compared to control cells. The energy barrier of pore formation,  $E^*$  can be considered as a sum of two components: (i) the energy barrier in the absence of electric field  $E_0$ , which depends on the membrane interfacial tension ( $\Gamma$ ), and the pore edge tension ( $\gamma$ ); and (ii) the decrease in the energy barrier due to induced  $V_m$ . The theoretical models of electroporation typically assume the following relation:

$$E^* = E_0 - BV_m^2. \quad (2.7)$$

In the above relation,  $B$  is a proportionality constant [19, 22]. As discussed above, analytical calculations demonstrate that  $V_m$  should be higher in the elongated cells; in our case, the control cells. This means that the lower energy barrier for pore formation in the treated cells, which we deduce from our analysis, is not due to the higher  $V_m$  induced on the treated cells. We corroborate this conclusion further by performing numerical calculations (see appendix for details of the numerical calculations) of the  $V_m$  on cylindrical cells with different sizes and orientation (Fig. 2.6(a)), as depicted in Fig. 2.6 as well as on spheroidal cells as reported in the appendix (Fig. 2.19). Fig. 2.6(b) shows the time course of the  $V_m$  at the two poles of each cell when the cells are exposed to a 500  $\mu$ s, 800 V/cm pulse. Regardless of the cell geometry,  $V_m$  reaches a peak value of  $\sim 0.8$  V upon which it decreases and stabilizes at  $\sim 0.5$  V. This decrease, also referred to as “electrical membrane breakdown” is due to an increase in the membrane conductivity caused by the formation of pores in the membrane. Since the pore creation rate is proportional to

$$\dot{n}_0 = \exp\left(-\frac{E_0}{k_B T} + \frac{BV_m^2}{k_B T}\right) \quad (2.8)$$

almost all the pores form in the membrane around the time of electrical breakdown when the  $V_m$  reaches its highest absolute value. Since the highest  $V_m$  practically does not depend on cell geometry, we exclude  $V_m$  as a possible source of the reduced energy barrier for pore formation in cells with disrupted actin filaments. To strengthen this conclusion further, we show numerical calculations in the supplementary material (Fig. 2.18) that by applying a lower electric field of 600 V/cm, the peak  $V_m$  is still about 0.8 V. Accordingly, we deduce similar values of the pore creation energy from experimental measurements at 600 V/cm (Fig. 2.15). Despite the similar values of pore creation energy at 600 V/cm, we observe a lower uptake of propidium ions to the cell compared to experiments at 800 V/cm. This can be attributed to the lower permeabilized area that is formed at lower voltages [30]. In Fig. 2.6, we show calculations for cells with cylindrical

shapes, keeping the cell volume constant, which we consider as the most representative for our experimental conditions. However, in Fig. 2.19 (appendix), we show that similar results are obtained for spheroidal cells with different volumes, further confirming that the time course of  $V_m$  is not highly dependent on the cell shape and size. We obtain the same conclusions by performing propidium uptake experiments on cells with intact actin networks, but a roughly spherical shape (appendix section 2.A). We show that the propidium uptake of CHO cells with a roughly spherical shape and intact actin networks have similar uptake profiles as our control cells, and a much lower uptake compared to cells treated by latrunculin (Fig. 2.7 and Fig. 2.8). In addition, we also show that disruption of actin with lower concentration (0.25  $\mu\text{M}$ ) still results in higher uptake of propidium compared to control cells, but lower compared to cells treated by latrunculin (0.5  $\mu\text{M}$ ), which provides clear evidence that the increased uptake that we observe is due to the disruption of actin.

Apart from  $V_m$ , the energy barrier of pore formation is also dependent on the membrane interfacial tension ( $\Gamma$ ), and the pore edge tension ( $\gamma$ ) [57, 58]. The free energy difference  $E$  between a defect-free lipid bilayer and one with a single hydrophilic pore of radius  $r_p$  is theoretically described as  $E = 2\pi r_p \gamma - \pi r_p^2 \Gamma$  [57]. The interfacial tension promotes the expansion of the pores while the edge tension works to close it. In the nucleation theory of electroporation, the energy barrier  $E^*$  is defined as the energy of the hydrophilic/hydrophobic pore when a hydrophobic pore transitions to a hydrophilic pore, which is theorized to happen at a pore radius of  $\sim 0.5$  nm. The contribution of surface tension to the free energy is negligible in comparison to that of edge tension for pores in size range of few nanometers, which are theorized to form during electroporation [58]. Hence, we discuss the influence of actin networks on the edge tension below.

As long-lived micron-sized pores have to be created for measuring edge tension, the reported values of measured edge tension were only obtained from experiments utilizing GUVs [59–62]. Since there are currently no visualizations of electropores in the cell membrane, a direct estimate of the edge tension is not available for the cell membranes with intact actin networks. Considering that the essence of edge tension is the energy required to bend the lipid bilayer at the rim of the pore, we can make estimates of edge tension from measurements of bending modulus ( $\kappa$ ) of the cell membrane [28, 63]. Assuming that the transmembrane pore is much larger than the membrane thickness ( $d = 5$  nm),  $\gamma$  can be related to the  $\kappa$  as  $\gamma \sim \pi\kappa/2d$ ; which means that the edge tension ( $\gamma$ ) is directly proportional to the bending modulus ( $\kappa$ ) [28]. The measurement of bending modulus in HeLa cells has suggested that the bending modulus is approximately ten times higher in the presence of a cortical actin network compared to a bleb devoid of actin networks [64]. Similarly, experiments show that elastic modulus, a property often related to bending modulus, is shown to be halved when actin networks are depolymerized [65, 66]. A lower bending modulus or a lower edge tension means that the pore energy is lower for the treated cells compared to the control cells. Hence, a lower energy barrier of pore formation for the treated cells, which we measure, could be attributed to a reduced bending modulus of the cell membrane when the actin networks are disrupted. As seen from eq. 2.8, a lower energy barrier of electroporation is associated with an increased number of pores in the membrane, which is consistent with our estimate that total area occupied by the pores in the membrane of the treated cells is higher

than the control cells. However, we cannot completely exclude the possibility that the average size of individual pores is also higher in the treated cells. For instance, studies on cell fusion have proposed that actin networks restrict the growth of fusion pores and that the fusion pores are accompanied by disassembly of the actin cortex under the pores [67], and theoretical models have suggested that cytoskeletal networks may stabilize the membrane against pore growth[68].

## 2.5. CONCLUSION

The role of actin in electroporation is studied in living cells by monitoring the uptake of propidium iodide to CHO cells. The disruption of actin networks causes higher uptake during electroporation. The uptake of propidium iodide to cells depend on the temperature in the range studied (11 °C to 37 °C), and uptake of propidium iodide increases with increasing temperature. The cells with disrupted actin networks show a weaker temperature dependence compared to the control cells. These results are analyzed using the nucleation theory of electroporation, and we conclude that the cells with disrupted actin networks have a reduced energy barrier of electropore formation. To approach towards better electroporation models, we thus suggest to consider the contribution of actin networks in the molecular description of electropore formation kinetics. In addition, it will be fruitful to test the effect of actin disruption on the uptake of biologically relevant molecules (e.g. siRNA and DNA) in the future studies [48, 69].

## AUTHOR CONTRIBUTIONS

A.M. and P.E.B designed the research; A.M. performed the research with contributions from L.R.; A. M. analyzed the data; A. M. wrote the chapter with contributions from L.R. and P.E.B.; P.E.B and M.T.K supervised the project.

## CHAPTER COVER

A confocal microscopy image of actin networks in NIH 3T3 cells stained with phalloidin-FITC.

## APPENDIX

## 2.A. PROPIDIUM IODIDE UPTAKE AT DIFFERENT LEVELS OF DISRUPTION OF ACTIN

2

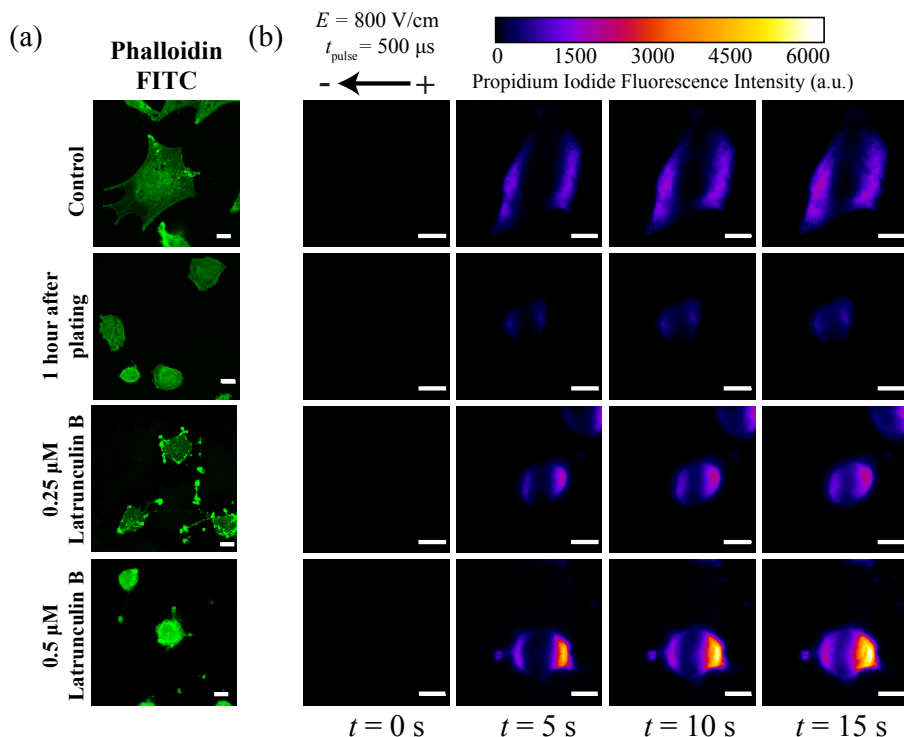


Figure 2.7: (a) Representative confocal images showing the intracellular structure of the actin network (before electroporation) for the control cells (top row), cells plated one hour prior to electroporation to obtain a spherical morphology (second row), cells treated with 0.25  $\mu\text{M}$  latrunculin B (third row) and 0.5  $\mu\text{M}$  latrunculin B to disrupt actin networks (bottom). The cells were fixed in formaldehyde and actin networks are stained with phalloidin FITC. The images are obtained by using the same imaging settings. (b) Representative fluorescence intensity profiles (bound propidium signal) for the corresponding cells at different times after electroporation. A single electric pulse with an amplitude of 800 V/cm and a pulse duration of 500  $\mu\text{s}$  was applied for these uptake experiments. Scale bars represent 10  $\mu\text{m}$ .

We performed electroporation experiments on CHO cells treated by latrunculin B (0.25  $\mu\text{M}$ ) leading to a lower level of actin disruption. The time sequence of the propidium iodide uptake (100  $\mu\text{M}$ ) by cells treated with latrunculin B (0.25  $\mu\text{M}$ ) during electroporation ( $E = 800$  V/cm,  $t_{\text{pulse}} = 500$   $\mu\text{s}$ ) is presented in Fig. 2.7 (third row). These cells continue to show the asymmetric uptake profiles similarly seen in the uptake experiments on cells in which actin was disrupted by latrunculin B (0.5  $\mu\text{M}$ ).

We also performed propidium iodide (100  $\mu\text{M}$ ) uptake experiments on CHO cells plated one hour before electroporation to decouple the effect of cell shape and actin disruption.

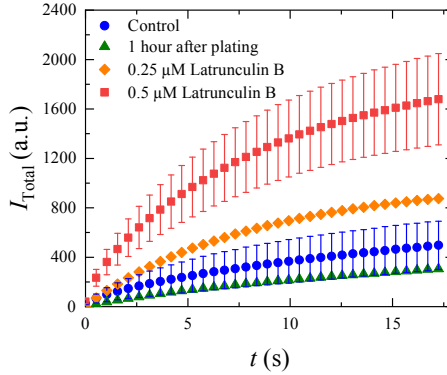


Figure 2.8: Temporal evolution of the total fluorescence intensity divided by the number of pixels in the region of interest both the control cells and the treated cells at room temperature. A representative uptake profile from a single experiment is shown for the cells treated with  $0.25 \mu\text{M}$  latrunculin B and cell plated for 1 hour. The total fluorescence intensity is measured as the sum of the fluorescence intensity inside a region of interest defined by the boundary of the cell. Only one among every fifth data point is shown for improving visibility. One electric pulse of  $800 \text{ V/cm}$  with a duration of  $500 \mu\text{s}$  is applied to obtain this data and the experiments are performed at room temperature.

tion. This allows the cells to adhere to the culture plates while maintaining a roughly spherical morphology. The results are presented in Fig. 2.7 (second row) and Fig. 2.8. These figures demonstrate that the cells with intact actin networks and a roughly spherical morphology have similar propidium uptake profiles as our control cells, and more importantly, a lower uptake than the latrunculin treated cells. We further quantify the uptake profiles and plot the time series of uptake for the control cells, plated cells with spherical morphology, and different levels actin disruption in Fig. 2.8. The plot shows that the actin disruption using latrunculin B ( $0.25 \mu\text{M}$ ) also increases the permeability of the CHO cells after electroporation compared to the control cells. The uptake in cells treated by latrunculin B ( $0.25 \mu\text{M}$ ) is lower than that of the cells disrupted by latrunculin B ( $0.5 \mu\text{M}$ ). This provides definite proof that increase in permeability of the cells after electroporation is coupled to the level of actin network disruption before the application of the electric pulse.

## 2.B. FLUORESCENCE INTENSITY DUE TO PROPIDIUM IODIDE UPTAKE ALONG THE CENTERLINE OF THE CELLS

In this section, we provide the fluorescent intensity profiles along the centerline of the cell, which is parallel to the electric field. In the Fig. 2.9, we provide the fluorescent intensity of different cells measure at time  $t = \tau$ . From Fig. 2.9(a), it can be observed that for the majority of the cells, transport of propidium iodide occurs from both the poles of the cell facing the electrodes. We see slightly higher transport from the pole facing the positive electrode, which could be due to the electrophoretic transport during the electric pulse. From Fig. 2.9(b), we can make the following observations. The transport of propidium iodide to treated cells is significantly higher at the pole facing the positive

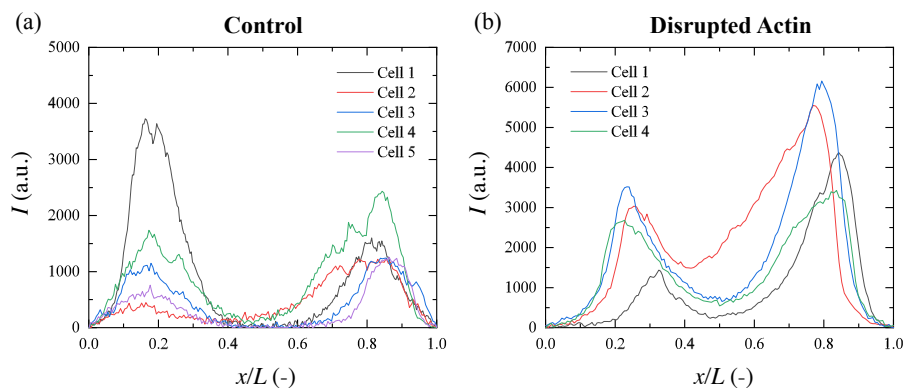


Figure 2.9: Fluorescent intensity across the centerline (similar to Fig. 2.2(b)) of the cell at time  $t = \tau$  for the experimentally tested (a) control cells, (b) treated cells at the room temperature. The point 0 corresponds to the first point on the cell from the side of the anode which emits a fluorescent intensity signal and 1 corresponds to the last point which emits a fluorescent intensity signal.

electrode. Besides, almost two-fold higher fluorescence intensity is emitted at the pole facing the positive electrode in all the treated cells compared to the control cells. A second striking difference between the measurements from the control cells and the treated cells is the extend of transport of propidium iodide. the propidium iodide fails to diffuse to the center of the cell by the time  $t = \tau$  in the control cells. In contrast, for all the treated cells, a fluorescent signal was emitted from the center, albeit small, which could be due to a higher intracellular diffusion coefficient for the treated cells.

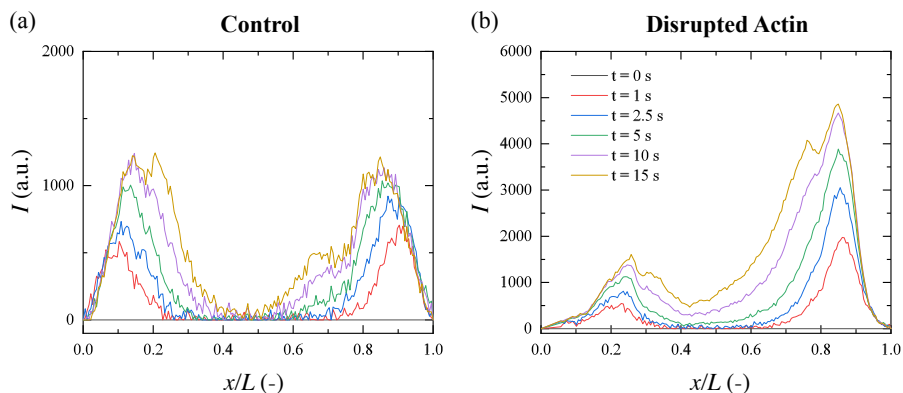


Figure 2.10: Fluorescent intensity across the centerline (similar to Fig. 2.2(b)) of the cell at different times for representative (a) control cells, (b) treated cells at the room temperature. The cells for which the intensity is displayed are the same cells shown in Fig. 2.1(b) and 2.2(b). The point 0 corresponds to the first point on the cell from the side of the anode which emits a fluorescent intensity signal and 1 corresponds to the last point which emits a fluorescent intensity signal.

We also provide the fluorescent intensity profiles across the centerline for different

time points after electroporation for a representative cell in Fig. 2.10. We can make the following observations. The fluorescent intensity along the centerline increases with time for both control cells (Fig. 2.10(a)) and treated cells (Fig. 2.10(b)). As time progresses, the penetration depth of propidium ions increases for both control and treated cells. The extent of the penetration of propidium ions is more in the treated cells. The propidium ions manage to penetrate through the entire centerline of the treated cell within the first five seconds which could either be due to the smaller size of the treated cell, or the higher intracellular diffusion coefficient.

## 2.C. PROPIDIUM IODIDE UPTAKE DURING ELECTROPORATION AT LOWER MAGNIFICATION (20X)

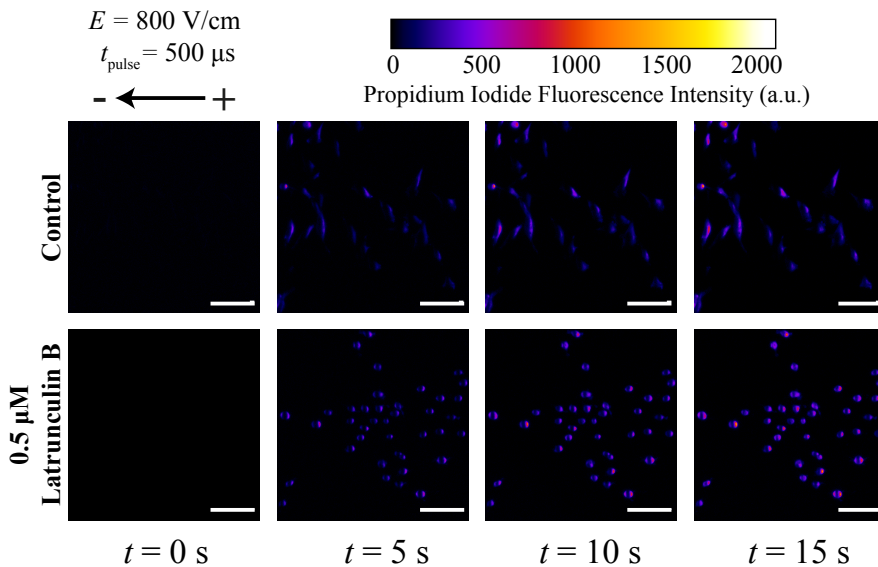


Figure 2.11: Representative time evolution of the fluorescence intensity profiles (bound propidium signal) for control cells and treated cells (with 0.5  $\mu\text{M}$  latrunculin B) after electroporation (imaged at 20x magnification). A single electric pulse with an amplitude of 800 V/cm and a pulse duration of 500  $\mu\text{s}$  was applied for these uptake experiments. Scale bars represent 100  $\mu\text{m}$ .

## 2.D. ANALYSIS OF PROPIDIUM IODIDE UPTAKE AT DIFFERENT TEMPERATURES INCLUDING TEMPERATURE DEPENDENCE OF $D$ AND $\nu$

Fig. 2.12 shows the fluorescent uptake profiles at all the different temperatures for the uptake experiments done with an electric field of 800 V/cm. eq. 2.4 relates the measurable parameters obtained from the uptake of propidium iodide, i.e., the fluorescent intensity and time constant with temperature. For simplicity, we had excluded the tem-



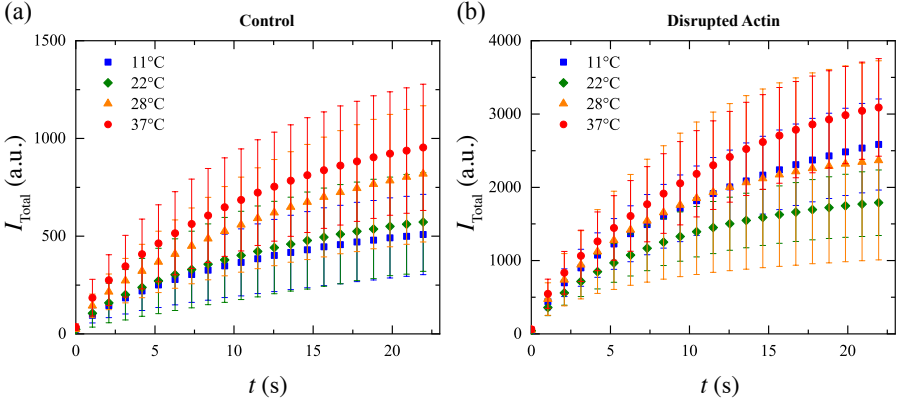


Figure 2.12: Temperature dependence of  $I_{\text{Total}}$  for (a) control cells and (b) cells with disrupted actin. One electric pulse of 800 V/cm with a duration of 500  $\mu\text{s}$  is applied to obtain this data. Data for 11°C, 22°C, 28°C and 37°C are shown in this figure. Only every 15th data point of the time series is shown for better clarity of the data. The symbols correspond to average value and the error bars correspond to standard deviation over measurements from 4-7 cells.

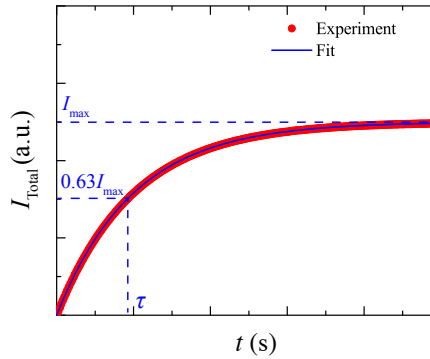


Figure 2.13: A representative plot to display how  $I_{\text{max}}$  and  $\tau$  are extracted from the temporal evolution of fluorescence data.

perature dependence of the diffusion coefficient and attempt rate frequency. Since exact correlations for the diffusion coefficient of propidium iodide through the confinement of electropores and attempt rate frequency are not available, we use the following approach. The simplified temperature dependence of the diffusion coefficient can be included in the calculations through Stokes-Einstein equation, which expresses diffusion coefficient as  $D = k_B T / (6\pi\eta R)$ , where  $\eta$  is the viscosity of the solvent (in our case, water), and  $R$  is the radius of the solute. For the temperature range we study ( $T/T_c < 0.75$ , where  $T_c = 647$  K is the critical temperature of water), the viscosity of water can be approximated by the Vogel equation [70, 71]. This eq. expresses viscosity of water as  $\eta = \exp(-3.72 + 578.92/(T - 137.55)) \times 10^{-3}$  Pa·s [72]. Since we are interested in transport through the electropores, it is reasonable to assume that the diffusion coefficient is

independent of the state of the cytoskeleton.

The description of attempt rate frequency to form electropores is more complex. The attempt rate frequency,  $\nu$  is frequently approximated by the frequency of lateral fluctuation of lipid molecules [17]. In this scenario, the state of the cytoskeleton can influence the magnitude of the  $\nu$ . For simplicity we use the approximation done in the work by Vasilkoski et. al.(2006), which assumes the lipids to behave like an ideal gas [19]. Vasilkoski et. al.(2006) describes the attempt rate frequency to be inversely proportional to the time between collision of two lipid molecules. Assuming 100 lipids are involved in the formation of pores, the attempt rate frequency can be correlated to temperature as  $\nu \sim 1/100 \times (2N_A k_B T / M_{lip} (\Delta x)^2)^{1/2}$ , where  $N_A$  is the Avogadro number,  $M_{lip}$  is the effective molecular weight of the lipids involved in poration,  $\Delta x$  is the distance between the lipid heads. Using these correlations, eq. 2.5 can be expanded as

$$\ln\left(\frac{I_{max}}{\tau}\right) = \ln\left(\frac{mc_e S a_p t_{pore} k_B}{10V d a_0 6\pi R}\right) + \frac{1}{2} \ln\left(\frac{2N_A k_B}{M_{lip} (\Delta x)^2}\right) + 3.72 - \frac{578.92}{T - 137.55} + \frac{3}{2} \ln(T) - \frac{E^*}{k_B T}. \quad (2.9)$$

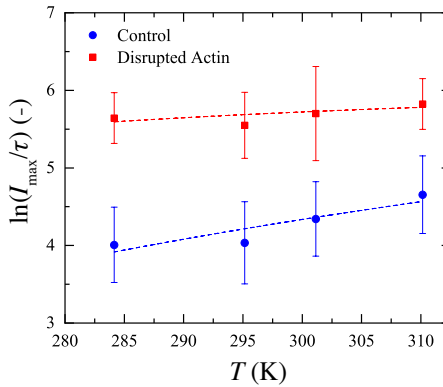


Figure 2.14: Dependence of  $\ln(I_{max}/\tau)$  with temperature. One electric pulse of 800 V/cm for 500  $\mu$ s was applied for obtaining this data. The solid symbols represent average value and the error bars represent standard deviation over 4-6 cells. The dashed lines correspond to the best fit of the experimental data with eq. 2.9.

We can infer that there are three contributing factors that could lead to an increase in uptake of molecules to the cell with increasing temperature, i.e. the increasing diffusion coefficient, increasing attempt rate frequency, and increasing probability of nucleation of pores. These contributions can be studied by looking at how  $\ln(I_{max}/\tau)$  varies with temperature according to eq. 2.9. Fig. 2.14 shows that  $\ln(I_{max}/\tau)$  increases with temperature for control cells and actin disrupted cells. The data is then fitted to eq. 2.9 using OriginPro to obtain the fitting parameters for the non-linear fit. The fit results in an estimated energy barrier for pore creation of  $\sim -255 \pm 696 k_B$  ( $-0.85 \pm 2.32 k_B T$ ) for control cells and  $\sim -1827 \pm 419 k_B$  ( $-6.09 \pm 1.40 k_B T$ ) for actin disrupted cells at the applied electric field of 800 V/cm. Note that we measure the negative energy barrier when we take

all the contributions into account. The temperature dependence used here are all based on approximations and it is uncertain if they are valid for solutions inside the pores. The exact analytical descriptions of the temperature dependence of the diffusion coefficient and attempt rate frequency might be more complex than the ones we use in our analysis. Indeed we notice that the temperature  $\ln(D)$  that we use is much stronger than all the other terms in eq. 2.9. We however use an idealized version of diffusion coefficient, which could indeed overestimate the temperature dependence. In fact it has been reported that molecules that are being delivered during electroporation can interact with the lipids, thereby restricting the diffusion to the cell [73].

## 2.E. TEMPERATURE DEPENDENCE OF PROPIDIUM IODIDE UPTAKE AT 600 V/CM

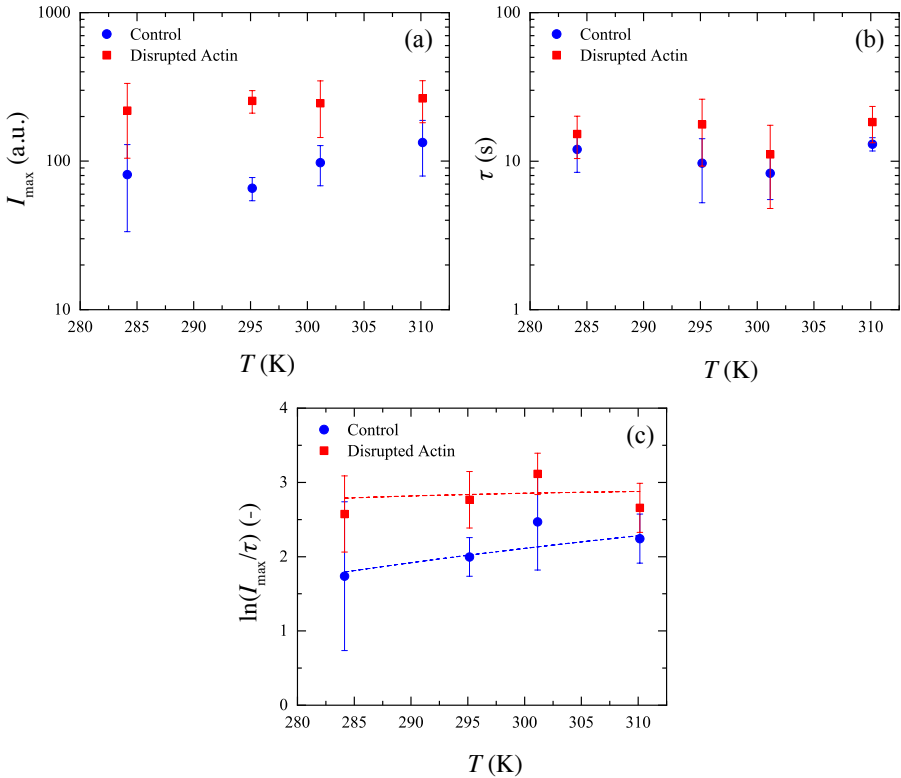


Figure 2.15: Dependence of extracted fitting parameters from the time dependence of propidium fluorescent intensity with temperature. One electric pulse of 600 V/cm for 500  $\mu$ s was applied for obtaining this data. The fluorescent profiles are fitted to the eq.  $I_{\text{Total}} = I_{\text{max}}(1 - \exp(-t/\tau))$ . (a) Dependence of plateau fluorescent intensity  $I_{\text{max}}$  with temperature. (b) Dependence of resealing time,  $\tau$  with temperature. (c) Dependence of  $\ln(I_{\text{max}}/\tau)$  with temperature. The solid symbols represent average value and the error bars represent standard deviation over 4-6 cells. The dashed lines correspond to the best fit of the experimental data with eq. 2.5.

In addition to the experiments performed with an applied electric field of 800 V/cm, we also perform experiments at lower electric field strength. In Fig. 2.15, we present the results we obtained for experiments performed with a pulse amplitude of 600 V/cm. Fig. 2.15(a) shows that the uptake of propidium iodide for cells with a disrupted actin network is higher at all temperatures compared to the control cells. These results are consistent with the observations made in experiments with a pulse amplitude of 800 V/cm. Besides, for both control and disrupted actin display a significantly lower uptake at 600 V/cm compared to their counterparts at 800 V/cm. From Fig. 2.15(b), we see that the average resealing time of cells with disrupted actin is almost 50-60% higher compared to the control cells. However, no conclusive statements can be made regarding the dependence of resealing time as the errors associated with extracting the resealing times from the experiment are large. We can, however, see that the resealing time does not change significantly when the experiments are done at 600 V/cm compared to the experiments performed at 800 V/cm. Hence, the higher uptake observed at the experiments performed at 800 V/cm compared to the ones at 600 V/cm should be a consequence of higher pore area at higher electric fields, which is expected as the permeabilized cap along the cell membrane will be larger at higher applied electric fields.

We further proceed to plotting the dependence of  $\ln(I_{\max}/\tau)$  with temperature in Fig. 2.15(c). We see a similar trend as the one observed at the experiments performed at 800 V/cm. The control cells display a stronger dependence of  $\ln(I_{\max}/\tau)$  with temperature compared to the treated cells. We then proceed to extract the energy barriers of pore creation from the experimental data using the simplified eq. 2.5 of the article. We measure an energy barrier  $\sim 0.97 \pm 5.74 k_B T$  for the treated cells and  $\sim 5.4 \pm 2.99 k_B T$  for the control cells. Similar to experiments performed at 800 V/cm; the average value energy barrier is reduced when the internal actin network is disrupted.

## 2.F. ROBUSTNESS OF THE EXPERIMENTAL FLUORESCENCE DATA

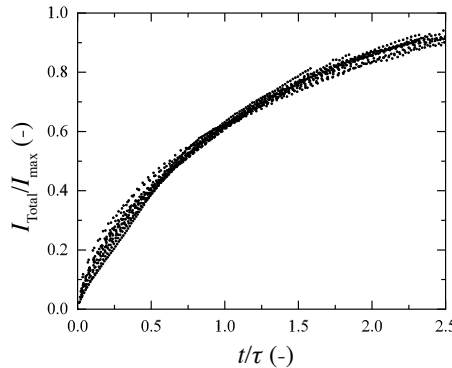


Figure 2.16: Randomly sampled raw time-fluorescence data normalized by the extracted fitting parameters  $I_{\max}$  and  $\tau$  to show the robustness of the fitting used in the study. The data showed here are randomly sampled from experiments conducted at different temperatures, state of cytoskeleton and external concentration of propidium iodide. The experiments shown here use one 500  $\mu$ s electric field of 800 V/cm.

In this study, the parameters  $I_{\max}$  and  $\tau$  are extracted from how the raw fluorescence data evolves with time. In Fig. 2.16, we provide randomly sampled raw data of  $I_{\text{Total}}$  from different experiments. The data is sampled from experiments performed at different temperatures, state of actin filaments inside the cell and different concentrations of propidium iodide. Here, the fluorescence intensity is normalized by  $I_{\max}$  and time is normalized by  $\tau$ , which are both extracted fitting parameters from the experiment. The data collapses reasonably well to the form  $I_{\text{Total}}/I_{\max} = 1 - \exp(-t/\tau)$ .

## 2.G. NUMERICAL CALCULATIONS

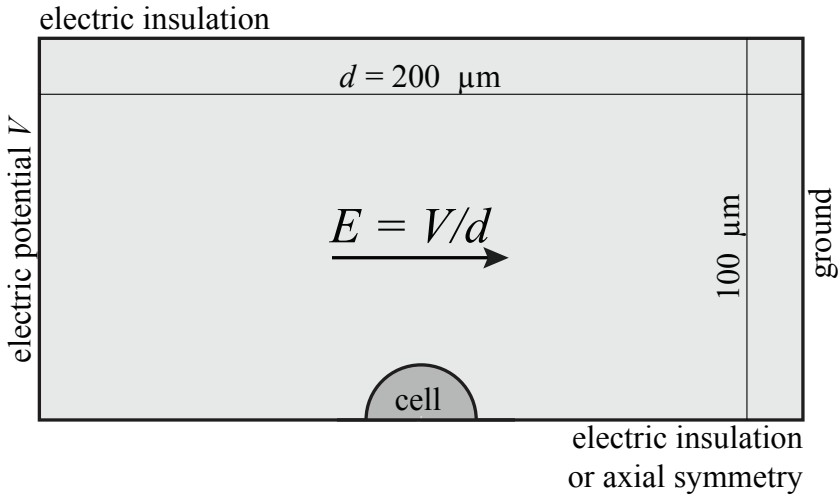


Figure 2.17: Geometry used for numerical calculations in Comsol<sup>®</sup>. The relevant boundary conditions are indicated on the image.

Numerical calculations of the induced transmembrane voltage have been performed in Comsol<sup>®</sup> Multiphysics 5.4. The model of a cell exposed to an electric field  $E$  is built in 2D cylindrical coordinate system. The geometry of a cell is an elliptic cylinder with semi-axes of the ellipse denoted as  $a$  and  $b$ , and the height of the cylinder denoted as  $h$  (Fig. 2.17). The length of the semi-axes and cylinder height were varied, as shown in Table 2.1, keeping the overall volume of the cell equal to the volume of a sphere with radius  $8 \mu\text{m}$ . The cell is positioned in a rectangular domain representing the extracellular medium, as shown in Fig. 2.17. In addition, we have also performed calculations for spheroidal cells with the same combination of semi-axes  $a$  and  $b$  as shown in Table 2.1, by using 2D axisymmetric coordinate system (instead of cylindrical). In this case, cells with larger semi-axes have larger volume.

The electroporation model has been constructed based on previously published models [15, 19, 78]. To model cell electroporation we need to calculate (i) the induced transmembrane voltage, for which we need to calculate the electric potential distribution outside and inside the cells (ii) formation of pores in the membrane and the corresponding

<b>a(μm)</b>	<b>b(μm)</b>	<b>h(μm)</b>
8	8	10.7
10	10	6.8
10	20	3.4
20	10	3.4
20	20	1.7

Table 2.1: Combinations of semi-axes and cylinder height used to create different geometries for the numerical calculations in Comsol®

<b>Parameter</b>	<b>Label</b>	<b>Value</b>	<b>Reference</b>
Extracellular conductivity	$\sigma_e$	0.15 S/m	[74]
Extracellular permittivity	$\epsilon_e$	80	[15]
Intracellular conductivity	$\sigma_i$	0.5 S/m	[15]
Intracellular permittivity	$\epsilon_i$	80	[15]
Membrane thickness	$d$	5 nm	[15]
Passive membrane conductance	$G_m$	2 S/m <sup>2</sup>	[15]
Passive membrane capacitance	$C_m$	0.01 F/m <sup>2</sup>	[15]
Resting potential	$V_{rest}$	-60 mV	[75]
Minimum pore radius	$r_{p,min}$	0.8 nm	[15]
Maximum pore radius	$r_{p,max}$	50 nm	[76]
Pore diffusion coefficient	$D_p$	$5 \times 10^{-14}$ m <sup>2</sup> /s	[15]
Pore edge tension	$\gamma$	$2 \times 10^{-11}$ N	[15]
Membrane tension without pores	$\Gamma_0$	$10^{-6}$ N/m	[15]
Tension of the hydrocarbon-water interface	$\Gamma'$	0.02	[15]
Parameter in electric pore energy	$F_{max}$	$7 \times 10^{-10}$ N/V <sup>2</sup>	[15]
Parameter in electric pore energy	$r_h$	0.97 nm	[15]
Parameter in electric pore energy	$r_t$	0.31 nm	[15]
Pore creation rate coefficient	$\alpha$	$10^9$ m <sup>-2</sup> s <sup>-1</sup>	[15]
Characteristic voltage of electroporation	$V_{ep}$	0.16 V	[77]
Equilibrium pore density	$N_{eq}$	$1.5 \times 10^9$ m <sup>-2</sup>	[15]
Parameter in pore creation rate	$q$	2.46	[15]
Temperature	$T$	298 K	

Table 2.2: List of values of model parameters used in the numerical calculations in Comsol®

increase in the membrane conductance, through which a feedback loop influences the electric potential distribution and the transmembrane voltage. The values of all parameters of the electroporation model are given in Table 2.2.

### 2.G.1. CALCULATION OF THE INDUCED TRANSMEMBRANE VOLTAGE

The electric potential distribution  $V$  in the intracellular and extracellular space is calculated by

$$\nabla \cdot [(\sigma_{i,e} + \epsilon_{i,e}) \nabla V_{i,e}] = 0 \quad (2.10)$$

where  $\sigma_{i,e}$  and  $\epsilon_{i,e}$  denote, respectively, the conductivity and the dielectric permittivity of the intracellular (subscript i) or extracellular (subscript e) medium. The cell membrane is modelled via a boundary condition, which describes the continuity of the normal component of the electric current density  $\mathbf{J}$  across the membrane

$$\mathbf{n} \cdot \mathbf{J} = G_m (V_m - V_{\text{rest}}) + G_{\text{ep}} V_m + C_m \frac{\partial V_m}{\partial t} \quad (2.11)$$

where  $\mathbf{n}$  denotes the unit vector normal to the membrane surface, whereas  $G_m$ ,  $G_{\text{ep}}$ , and  $C_m$  denote the passive membrane conductance, conductance due to formation of pores in the membrane, and membrane capacitance, respectively. The transmembrane voltage  $V_m$  corresponds to the difference between the electric potentials on the two sides of the membrane  $V_m = V_i - V_e$ .  $V_{\text{rest}}$  is the resting potential.

## 2.G.2. MODEL OF MEMBRANE ELECTROPORATION

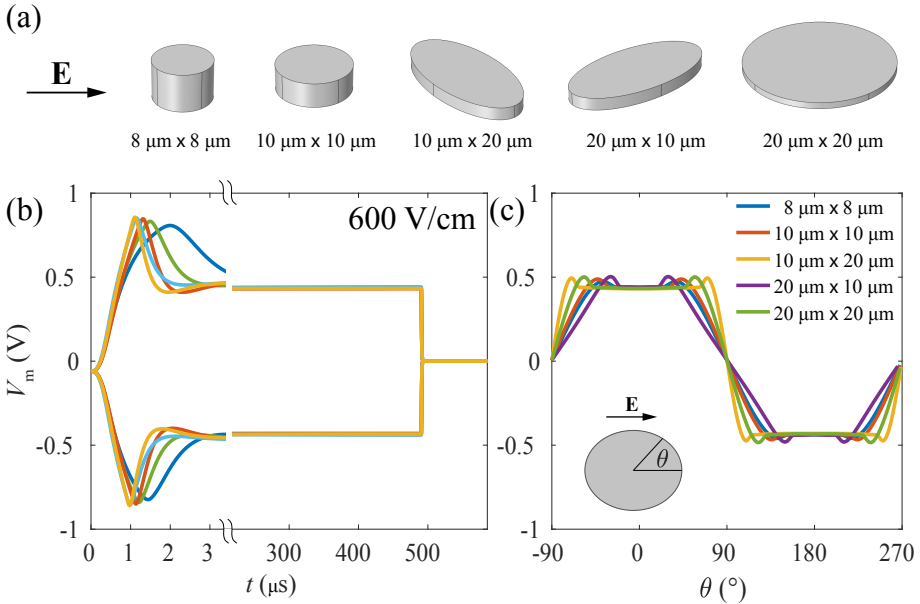


Figure 2.18: Calculations of the induced transmembrane voltage for cylindrical cells. (a) 3D representation of the cell geometry considered. (b) Time course of the transmembrane voltage at the anodic and cathodic pole of the cell (at  $\theta = 0$  and  $\theta = \pi$ ). (c) Profile of the induced transmembrane voltage along the cell membrane at the end of a  $500 \mu\text{s}$ ,  $600 \text{ V/cm}$  pulse.

Membrane electroporation is included in the model with the following mathematical description. The population of pores, which forms in the membrane under the influence of the induced transmembrane voltage, is described by a distribution function  $n$  in the space of the pore radii such that  $ndr_p$  corresponds to the number of pores between radii  $r_p$  and  $r_p + dr_p$ . The size dynamics of the population of pores  $n$  is described by the

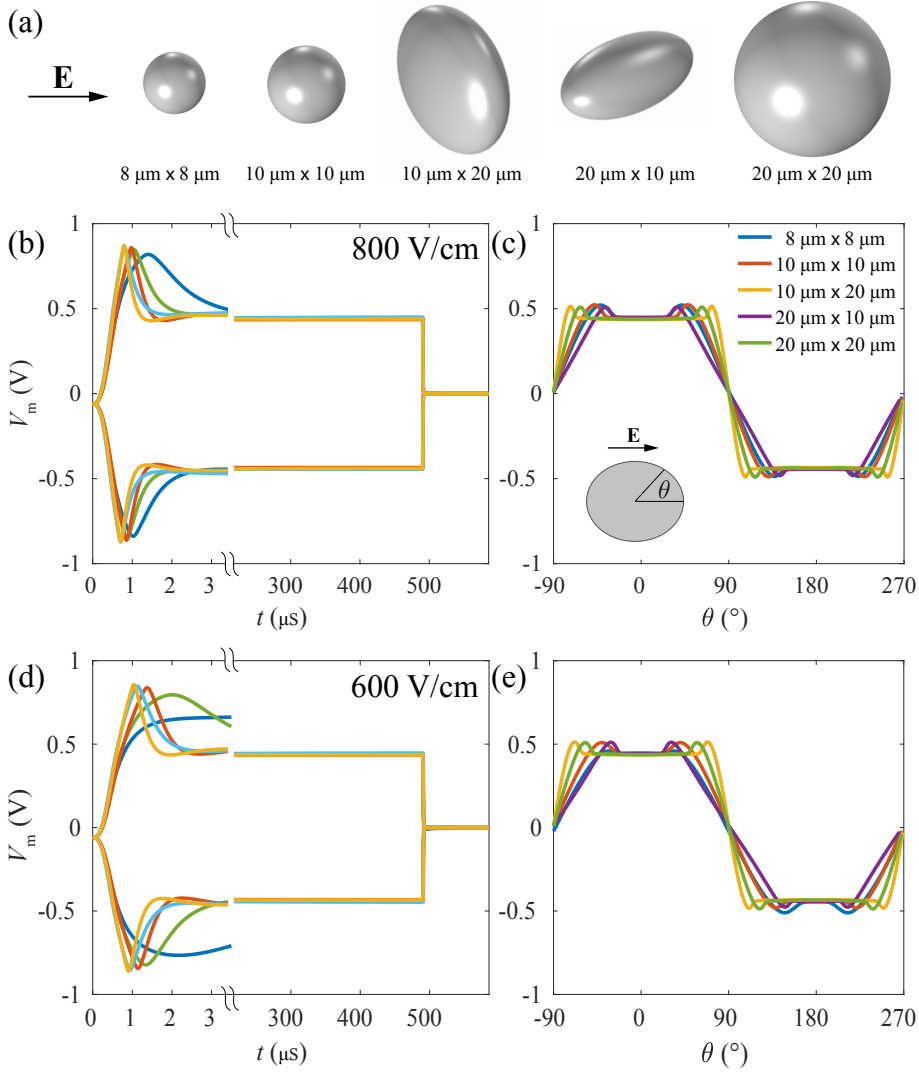


Figure 2.19: Calculations of the induced transmembrane voltage for spheroidal cells. (a) 3D representation of the cell geometry considered. Calculations in (b-c) and (d-e) are, respectively, for  $500 \mu\text{s}$ ,  $800 \text{ V/cm}$  pulse and  $500 \mu\text{s}$ ,  $600 \text{ V/cm}$  pulse. (b) Time course of the transmembrane voltage at the anodic and cathodic pole of the cell (at  $\theta = 0$  and  $\theta = \pi$ ). (c) Profile of the induced transmembrane voltage along the cell membrane at the end of the pulse.

### Smoluchowski equation

$$\frac{\partial n}{\partial t} = -\frac{\partial J_p}{\partial r_p} \quad (2.12a)$$

$$J_p = -D_p \frac{\partial n}{\partial r_p} - \frac{D_p}{k_B T} n \frac{\partial E^*}{\partial r_p} \quad (2.12b)$$



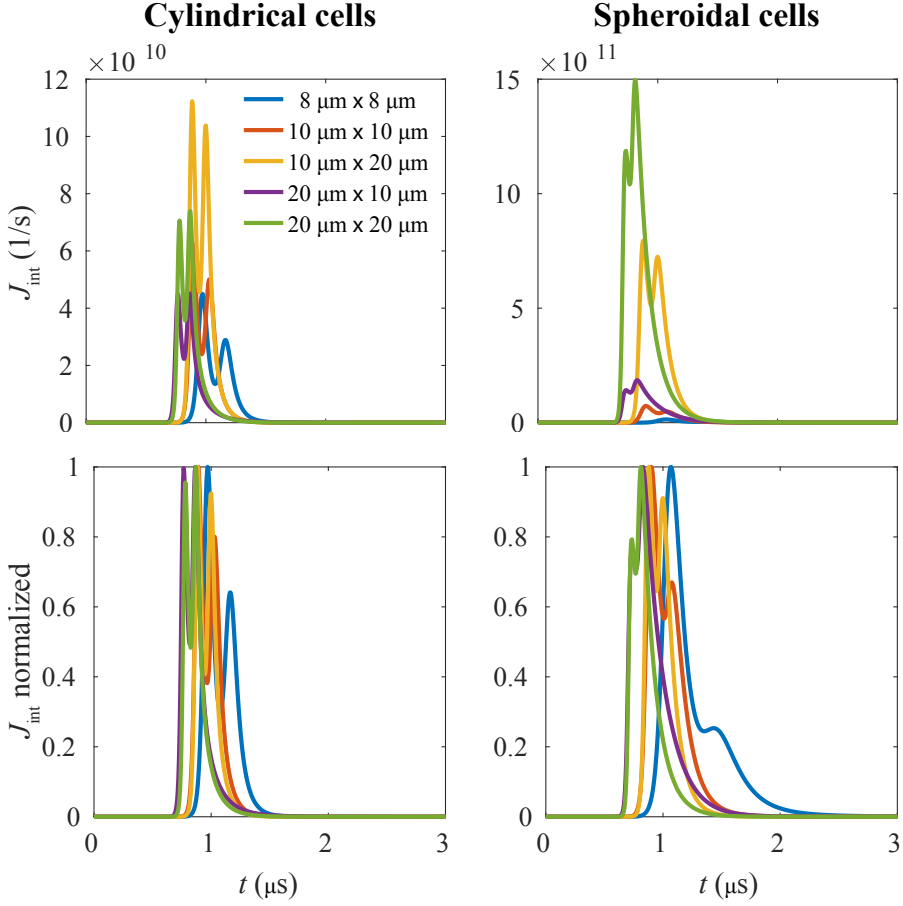


Figure 2.20: Pore creation rate integrated over the entire cell membrane for cylindrical and spheroidal cells exposed to 500  $\mu\text{s}$ , 600 V/cm pulse. Most pores are created within about 200-ns-long interval the first 2  $\mu\text{s}$  of the pulse, when the transmembrane voltage reaches its peak absolute value. The profile of the pore creation rate does not depend much on cell geometry. In bottom two graphs the curves are normalized to their peak value.

where  $J_p$  denotes the flux of pores in the space of their radii,  $D_p$  the pore diffusion coefficient,  $E^*$  the pore energy,  $k_B$  the Boltzmann constant, and  $T$  the temperature. The derivative  $\partial E^*/\partial r_p$  corresponds to the force, which acts to expand or shrink a pore and is given by

$$\frac{\partial E^*}{\partial r_p} = 2\pi\gamma - 2\pi r_p \Gamma_{\text{eff}} - \frac{F_{\text{max}} V_m^2}{1 + r_h/(r_p + r_t)} \quad (2.13)$$

where  $\gamma$  and  $\Gamma_{\text{eff}}$  denote the pore edge tension and the effective membrane surface ten-

sion respectively. The last term is an analytical fit to the numerical solution for the force actin to expand the pore due to Maxwell stress at the lipid-water interface [79]. The effective surface tensions is given by

$$\Gamma_{\text{eff}} = 2\Gamma' - \frac{2\Gamma' - \Gamma_0}{(1 - \text{PAD})^2} \quad (2.14a)$$

$$\text{PAD} = \int_{r_{p,\min}}^{r_{p,\max}} n dr_p \quad (2.14b)$$

where  $\Gamma_0$ ,  $\Gamma'$ , and PAD denote the tension of the membrane without pores, energy per area of the hydrocarbon-water interface, and the pore area density, respectively [15].

The Smoluchowski eq. is solved in the space of pore radii on the interval  $[r_{p,\min}, r_{p,\max}]$ . At the maximum pore radius  $r_{p,\max} = 50$  nm we use zero flux boundary condition

$$J_p(r_{p,\max}) = 0. \quad (2.15)$$

At the minimum pore radius  $r_{p,\min} = 0.8$  nm, we use the description for pore creation and destruction rate, derived by Neu and Krassowska (1999)

$$J_p(r_{p,\min}) = \alpha \exp\left(\frac{V_m^2}{V_{\text{ep}}^2}\right) \left(1 - \frac{n}{N_{\text{eq}}} \exp\left(-q \frac{V_m^2}{V_{\text{ep}}^2}\right)\right) \quad (2.16a)$$

$$N_{\text{eq}} \approx N_{\text{eq}} \frac{2\pi\gamma}{k_B T} \quad (2.16b)$$

where  $\alpha$ ,  $V_{\text{ep}}$ , and  $N_{\text{eq}}$  are pore creation rate coefficient, characteristic voltage of electroporation, and equilibrium pore density, respectively [58].

Pores allow transport of ions; therefore, their formation and expansion increases membrane ionic conductance. The increase in the membrane conductance due to pores  $G_{\text{ep}}$  is obtained by integrating the product of the distribution  $n$  and the conductance of a single pore  $G_p$ , whereby the latter varies with the pore radius

$$G_{\text{ep}} = \int_{r_{p,\min}}^{r_{p,\max}} n G_p dr_p. \quad (2.17)$$

For cylindrical pores, the conductance of a single pore can be derived analytically [80] and is given by

$$G_p = \frac{2\pi\sigma_p r_p^2}{\pi r_p + 2d} \quad (2.18a)$$

$$\sigma_p = \frac{\sigma_e - \sigma_i}{\ln(\sigma_e/\sigma_i)} \quad (2.18b)$$

Since the transmembrane voltage varies with position on the membrane, and since the dynamics of pore population depends on the transmembrane voltage, we need to calculate equations 2.12-2.18 at multiple points over the entire membrane. To do so, we divide the cell membrane into 160 parts (each part with angle  $\pi/80$  rad), and for each of

these parts, we define a separate pore radius space where we calculate equations 2.12-2.18.

Additional results from numerical calculations are presented in Fig. 2.18-2.20. Fig. 2.18 shows the same calculations as Fig. 2.6, but for lower applied electric field of 600 V/cm. Note that with 600 V/cm, cell membranes still become electroporated, therefore, the profiles of the induced transmembrane voltage are very similar to those obtained for 800 V/cm. Fig. 2.19 shows calculations for spheroidal cell instead of cylindrical cells (the calculations were performed in 2D axisymmetric system). In this case the cells with different semi-axes  $a$  and  $b$  have considerably different volumes, as shown in Fig. 2.19(a). Nevertheless, the profiles of the transmembrane voltage are similar to those presented for cylindrical cells in Fig. 6 and Fig. 2.18, indicating that the geometry and size of the cells does not influence much the time course and magnitude of the induced transmembrane voltage, provided that the electric field is sufficiently higher than the threshold for electroporation. Fig. 2.20 shows the flux  $J_p$ , which is given in eq. 2.16 and corresponds to pore creation and destruction, integrated over the entire membrane surface. Calculations are performed for all combinations of semi-axes  $a$  and  $b$ , in cylindrical coordinate system (cylindrical cells) and axisymmetric coordinate system (spheroidal cells). The results show that regardless of the cell size and geometry, most of the pores are created within about 200 ns long interval at the beginning of the pulse, when the induced transmembrane voltage reaches its peak value. This is due to the exponential dependence of  $J_p$  on the induced transmembrane voltage, as given in eq. 2.16. The duration for which the pore creation rate is high is similar for all cells regardless of their geometry, therefore we consider reasonable to approximate the pore creation time as  $t_{\text{pore}}$ , as we do in eq. 2.3.

## 2.H. JOULE HEATING

The adiabatic temperature increase from a single electric pulse of duration  $t_{\text{pulse}}$ , and amplitude  $E$  is given by

$$\Delta T = \frac{\sigma_e}{\rho C} E^2 t_{\text{pulse}} \quad (2.19)$$

where  $\Delta T$  is the temperature increase of the electroporation buffer,  $\rho$  is the density of the electroporation buffer ( $\approx 1000 \text{ kg/m}^3$ ),  $C$  is specific heat capacity of the electroporation buffer ( $\approx 4 \text{ kJ/kg K}$ ) and  $\sigma$  is the electric conductivity [81]. The conductivity of the pulsing buffer was measured to be 0.127 S/m with a Mettler toledo S230 (sevencompact) conductivity meter equipped with an inlab 731 ISM electrode. For a 500  $\mu\text{s}$  electric pulse of amplitude 800 V/cm, the estimated temperature increase is  $\approx 0.1 \text{ K}$ .

## REFERENCES

- [1] A. Muralidharan, L. Rems, M. T. Kreutzer, and P. E. Boukany, *Actin networks regulate the cell membrane permeability during electroporation*, *Biochimica et Biophysica Acta (BBA)-Biomembranes* **1863**, 183468 (2021).
- [2] H. Lodish, A. Berk, C. A. Kaiser, M. Krieger, M. P. Scott, A. Bretscher, H. Ploegh, P. Matsudaira, *et al.*, *Molecular Cell Biology* (Macmillan, 2008).
- [3] D. A. Fletcher and R. D. Mullins, *Cell mechanics and the cytoskeleton*, *Nature* **463**, 485 (2010).
- [4] M. P. Stewart, R. Langer, and K. F. Jensen, *Intracellular delivery by membrane disruption: mechanisms, strategies, and concepts*, *Chemical Reviews* **118**, 7409 (2018).
- [5] K. Kinoshita Jr and T. Y. Tsong, *Formation and resealing of pores of controlled sizes in human erythrocyte membrane*, *Nature* **268**, 438 (1977).
- [6] T. Kotnik, L. Rems, M. Tarek, and D. Miklavčič, *Membrane electroporation and electroporabilization: mechanisms and models*, *Annual Review of Biophysics* **48**, 63 (2019).
- [7] L. C. Heller and R. Heller, *In vivo electroporation for gene therapy*, *Human Gene Therapy* **17**, 890 (2006).
- [8] D. Miklavčič, B. Mali, B. Kos, R. Heller, and G. Serša, *Electrochemotherapy: from the drawing board into medical practice*, *Biomedical Engineering Online* **13**, 29 (2014).
- [9] M. L. Yarmush, A. Golberg, G. Serša, T. Kotnik, and D. Miklavčič, *Electroporation-based technologies for medicine: principles, applications, and challenges*, *Annual Review of Biomedical Engineering* **16**, 295 (2014).
- [10] B. Geboers, H. J. Scheffer, P. M. Graybill, A. H. Ruarus, S. Nieuwenhuizen, R. S. Puijk, P. M. van den Tol, R. V. Davalos, B. Rubinsky, T. D. de Gruijl, *et al.*, *High-voltage electrical pulses in oncology: irreversible electroporation, electrochemotherapy, gene electrotransfer, electrofusion, and electroimmunotherapy*, *Radiology* **295**, 254 (2020).
- [11] C. L. Trimble, M. P. Morrow, K. A. Kravnyak, X. Shen, M. Dallas, J. Yan, L. Edwards, R. L. Parker, L. Denny, M. Giffear, *et al.*, *Safety, efficacy, and immunogenicity of vgx-3100, a therapeutic synthetic DNA vaccine targeting human papillomavirus 16 and 18 e6 and e7 proteins for cervical intraepithelial neoplasia 2/3: a randomised, double-blind, placebo-controlled phase 2b trial*, *The Lancet* **386**, 2078 (2015).
- [12] K. Modjarrad, C. C. Roberts, K. T. Mills, A. R. Castellano, K. Paolino, K. Muthumani, E. L. Reuschel, M. L. Robb, T. Racine, M.-d. Oh, *et al.*, *Safety and immunogenicity of an anti-middle east respiratory syndrome coronavirus DNA vaccine: a phase 1, open-label, single-arm, dose-escalation trial*, *The Lancet Infectious Diseases* **19**, 1013 (2019).

- [13] E. Maor, A. Sugrue, C. Witt, V. R. Vaidya, C. V. DeSimone, S. J. Asirvatham, and S. Kapa, *Pulsed electric fields for cardiac ablation and beyond: A state-of-the-art review*, *Heart Rhythm* **16**, 1112 (2019).
- [14] J. Teissie, M. Golzio, and M. Rols, *Mechanisms of cell membrane electroporation: a minireview of our present (lack of?) knowledge*, *Biochimica et Biophysica Acta (BBA)-General Subjects* **1724**, 270 (2005).
- [15] W. Krassowska and P. D. Filev, *Modeling electroporation in a single cell*, *Biophysical Journal* **92**, 404 (2007).
- [16] I. Abidor, V. Arakelyan, L. Chernomordik, Y. A. Chizmadzhev, V. Pastushenko, and M. Tarasevich, *Electric breakdown of bilayer lipid membranes: I. the main experimental facts and their qualitative discussion*, *Journal of Electroanalytical Chemistry and Interfacial Electrochemistry* **104**, 37 (1979).
- [17] R. W. Glaser, S. L. Leikin, L. V. Chernomordik, V. F. Pastushenko, and A. I. Sokirko, *Reversible electrical breakdown of lipid bilayers: formation and evolution of pores*, *Biochimica et Biophysica Acta (BBA)-Biomembranes* **940**, 275 (1988).
- [18] J. C. Weaver and Y. A. Chizmadzhev, *Theory of electroporation: a review*, *Bioelectrochemistry and Bioenergetics* **41**, 135 (1996).
- [19] Z. Vasilkoski, A. T. Esser, T. Gowrishankar, and J. C. Weaver, *Membrane electroporation: The absolute rate equation and nanosecond time scale pore creation*, *Physical Review E* **74**, 021904 (2006).
- [20] D. L. Perrier, L. Rems, and P. E. Boukany, *Lipid vesicles in pulsed electric fields: fundamental principles of the membrane response and its biomedical applications*, *Advances in Colloid and Interface Science* **249**, 248 (2017).
- [21] J. T. Sengel and M. I. Wallace, *Imaging the dynamics of individual electropores*, *Proceedings of the National Academy of Sciences* **113**, 5281 (2016).
- [22] J. T. Sengel and M. I. Wallace, *Measuring the potential energy barrier to lipid bilayer electroporation*, *Philosophical Transactions of the Royal Society B: Biological Sciences* **372**, 20160227 (2017).
- [23] T. Portet, F. C. i Febrer, J.-M. Escoffre, C. Favard, M.-P. Rols, and D. S. Dean, *Visualization of membrane loss during the shrinkage of giant vesicles under electropulsation*, *Biophysical Journal* **96**, 4109 (2009).
- [24] K. A. Riske and R. Dimova, *Electro-deformation and poration of giant vesicles viewed with high temporal resolution*, *Biophysical Journal* **88**, 1143 (2005).
- [25] M. Tarek, *Membrane electroporation: a molecular dynamics simulation*, *Biophysical Journal* **88**, 4045 (2005).
- [26] D. P. Tieleman, *The molecular basis of electroporation*, *BMC Biochemistry* **5**, 10 (2004).

- [27] A. K. Majhi, S. Kanchi, V. Venkataraman, K. Ayappa, and P. K. Maiti, *Estimation of activation energy for electroporation and pore growth rate in liquid crystalline and gel phases of lipid bilayers using molecular dynamics simulations*, *Soft Matter* **11**, 8632 (2015).
- [28] J. Wohrlert, W. K. den Otter, O. Edholm, and W. J. Briels, *Free energy of a transmembrane pore calculated from atomistic molecular dynamics simulations*, *The Journal of Chemical Physics* **124**, 154905 (2006).
- [29] C. L. Ting, N. Awasthi, M. Müller, and J. S. Hub, *Metastable prepores in tension-free lipid bilayers*, *Physical Review Letters* **120**, 128103 (2018).
- [30] M.-P. Rols and J. Teissie, *Electropermeabilization of mammalian cells. quantitative analysis of the phenomenon*, *Biophysical Journal* **58**, 1089 (1990).
- [31] R. Shirakashi, V. L. Sukhorukov, I. Tanasawa, and U. Zimmermann, *Measurement of the permeability and resealing time constant of the electroporated mammalian cell membranes*, *International Journal of Heat and Mass Transfer* **47**, 4517 (2004).
- [32] E. Tekle, R. Astumian, W. Friauf, and P. Chock, *Asymmetric pore distribution and loss of membrane lipid in electroporated dopc vesicles*, *Biophysical Journal* **81**, 960 (2001).
- [33] S. Sachdev, A. Muralidharan, D. K. Choudhary, D. L. Perrier, L. Rems, M. T. Kreutzer, and P. E. Boukany, *DNA translocation to giant unilamellar vesicles during electroporation is independent of DNA size*, *Soft Matter* **15**, 9187 (2019).
- [34] R. L. Knorr, M. Staykova, R. S. Gracià, and R. Dimova, *Wrinkling and electroporation of giant vesicles in the gel phase*, *Soft Matter* **6**, 1990 (2010).
- [35] D. L. Perrier, L. Rems, M. T. Kreutzer, and P. E. Boukany, *The role of gel-phase domains in electroporation of vesicles*, *Scientific Reports* **8**, 1 (2018).
- [36] I. van Uitert, S. Le Gac, and A. van den Berg, *The influence of different membrane components on the electrical stability of bilayer lipid membranes*, *Biochimica et Biophysica Acta (BBA)-Biomembranes* **1798**, 21 (2010).
- [37] D. L. Perrier, A. Vahid, V. Kathavi, L. Stam, L. Rems, Y. Mulla, A. Muralidharan, G. H. Koenderink, M. T. Kreutzer, and P. E. Boukany, *Response of an actin network in vesicles under electric pulses*, *Scientific Reports* **9**, 8151 (2019).
- [38] M.-P. Rols and J. Teissie, *Experimental evidence for the involvement of the cytoskeleton in mammalian cell electropermeabilization*, *Biochimica et Biophysica Acta (BBA)-Biomembranes* **1111**, 45 (1992).
- [39] J. Teissie and M.-P. Rols, *Manipulation of cell cytoskeleton affects the lifetime of cell membrane electropermeabilization*, *Annals of the New York Academy of Sciences* **720**, 98 (1994).

- [40] C. Blangero, M. Rols, and J. Teissie, *Cytoskeletal reorganization during electric-field-induced fusion of chinese hamster ovary cells grown in monolayers*, *Biochimica et Biophysica Acta (BBA)-Biomembranes* **981**, 295 (1989).
- [41] C. Kanthou, S. Kranjc, G. Sersa, G. Tozer, A. Zupanic, and M. Cemazar, *The endothelial cytoskeleton as a target of electroporation-based therapies*, *Molecular Cancer Therapeutics* **5**, 3145 (2006).
- [42] L. Chopinet, C. Roudit, M.-P. Rols, and E. Dague, *Destabilization induced by electroporation analyzed by atomic force microscopy*, *Biochimica et Biophysica Acta (BBA)-Biomembranes* **1828**, 2223 (2013).
- [43] J. Dinic, P. Ashrafzadeh, and I. Parmryd, *Actin filaments attachment at the plasma membrane in live cells cause the formation of ordered lipid domains*, *Biochimica et Biophysica Acta (BBA)-Biomembranes* **1828**, 1102 (2013).
- [44] R. Reigada, *Electroporation of heterogeneous lipid membranes*, *Biochimica et Biophysica Acta (BBA)-Biomembranes* **1838**, 814 (2014).
- [45] P. M. Graybill and R. V. Davalos, *Cytoskeletal disruption after electroporation and its significance to pulsed electric field therapies*, *Cancers* **12**, 1132 (2020).
- [46] H. B. Kim, S. Lee, J. H. Chung, S. N. Kim, C. K. Sung, and K. Y. Baik, *Effects of actin cytoskeleton disruption on electroporation in vitro*, *Applied Biochemistry and Biotechnology* **191**, 1545 (2020).
- [47] A. T. Esser, K. C. Smith, T. Gowrishankar, Z. Vasilkoski, and J. C. Weaver, *Mechanisms for the intracellular manipulation of organelles by conventional electroporation*, *Biophysical Journal* **98**, 2506 (2010).
- [48] C. Rosazza, J.-M. Escoffre, A. Zumbusch, and M.-P. Rols, *The actin cytoskeleton has an active role in the electrotransfer of plasmid DNA in mammalian cells*, *Molecular Therapy* **19**, 913 (2011).
- [49] T. D. Pollard, W. C. Earnshaw, J. Lippincott-Schwartz, and G. Johnson, *Cell Biology* (Elsevier Health Sciences, 2016).
- [50] T. B. Napotnik and D. Miklavčič, *In vitro electroporation detection methods—an overview*, *Bioelectrochemistry* **120**, 166 (2018).
- [51] G. Pucihar, T. Kotnik, D. Miklavčič, and J. Teissié, *Kinetics of transmembrane transport of small molecules into electroporated cells*, *Biophysical Journal* **95**, 2837 (2008).
- [52] J. Dermol, O. N. Pakhomova, A. G. Pakhomov, and D. Miklavčič, *Cell electrosensitization exists only in certain electroporation buffers*, *PloS One* **11**, e0159434 (2016).
- [53] E. Dauty and A. Verkman, *Actin cytoskeleton as the principal determinant of size-dependent DNA mobility in cytoplasm a new barrier for non-viral gene delivery*, *Journal of Biological Chemistry* **280**, 7823 (2005).

- [54] Z. Fan, H. Liu, M. Mayer, and C. X. Deng, *Spatiotemporally controlled single cell sonoporation*, Proceedings of the National Academy of Sciences **109**, 16486 (2012).
- [55] T. Kotnik, G. Pucihar, and D. Miklavčič, *Induced transmembrane voltage and its correlation with electroporation-mediated molecular transport*, The Journal of Membrane Biology **236**, 3 (2010).
- [56] B. Valič, M. Golzio, M. Pavlin, A. Schatz, C. Faurie, B. Gabriel, J. Teissié, M.-P. Rols, and D. Miklavčič, *Effect of electric field induced transmembrane potential on spheroidal cells: theory and experiment*, European Biophysics Journal **32**, 519 (2003).
- [57] J. Litster, *Stability of lipid bilayers and red blood cell membranes*, Physics Letters A **53**, 193 (1975).
- [58] J. C. Neu and W. Krassowska, *Asymptotic model of electroporation*, Physical Review E **59**, 3471 (1999).
- [59] O. Sandre, L. Moreaux, and F. Brochard-Wyart, *Dynamics of transient pores in stretched vesicles*, Proceedings of the National Academy of Sciences **96**, 10591 (1999).
- [60] P.-H. Puech, N. Borghi, E. Karatekin, and F. Brochard-Wyart, *Line thermodynamics: adsorption at a membrane edge*, Physical Review Letters **90**, 128304 (2003).
- [61] E. Karatekin, O. Sandre, H. Guitouni, N. Borghi, P.-H. Puech, and F. Brochard-Wyart, *Cascades of transient pores in giant vesicles: line tension and transport*, Biophysical Journal **84**, 1734 (2003).
- [62] T. Portet and R. Dimova, *A new method for measuring edge tensions and stability of lipid bilayers: effect of membrane composition*, Biophysical Journal **99**, 3264 (2010).
- [63] M. M. Kozlov and L. V. Chernomordik, *Membrane tension and membrane fusion*, Current Opinion in Structural Biology **33**, 61 (2015).
- [64] G. T. Charras, M. Coughlin, T. J. Mitchison, and L. Mahadevan, *Life and times of a cellular bleb*, Biophysical Journal **94**, 1836 (2008).
- [65] J.-Y. Tinevez, U. Schulze, G. Salbreux, J. Roensch, J.-F. Joanny, and E. Paluch, *Role of cortical tension in bleb growth*, Proceedings of the National Academy of Sciences **106**, 18581 (2009).
- [66] G. Salbreux, G. Charras, and E. Paluch, *Actin cortex mechanics and cellular morphogenesis*, Trends in Cell Biology **22**, 536 (2012).
- [67] A. Chen, E. Leikina, K. Melikov, B. Podbilewicz, M. M. Kozlov, and L. V. Chernomordik, *Fusion-pore expansion during syncytium formation is restricted by an actin network*, Journal of Cell Science **121**, 3619 (2008).
- [68] W. Sung and P. Park, *Dynamics of pore growth in membranes and membrane stability*, Biophysical Journal **73**, 1797 (1997).



- [69] S. Sachdev, S. F. Moreira, Y. Keehnen, L. Rems, M. T. Kreutzer, and P. E. Boukany, *DNA-membrane complex formation during electroporation is DNA size-dependent*, *Biochimica et Biophysica Acta (BBA)-Biomembranes* **1862**, 183089 (2020).
- [70] J. H. Perry, *Chemical engineer's handbook*, (1984).
- [71] R. C. Reid, J. M. Prausnitz, and B. E. Poling, *The properties of gases and liquids*, (1987).
- [72] *Liquid dynamic viscosity, calculation by vogel equation*, .
- [73] E. B. Sözer, Z. A. Levine, and P. T. Vernier, *Quantitative limits on small molecule transport via the electroporeome—measuring and modeling single nanosecond perturbations*, *Scientific Reports* **7**, 1 (2017).
- [74] G. Pucihar, T. Kotnik, M. Kandušer, and D. Miklavčič, *The influence of medium conductivity on electroporeabilization and survival of cells in vitro*, *Bioelectrochemistry* **54**, 107 (2001).
- [75] B. Gabriel and J. Teissie, *Time courses of mammalian cell electroporeabilization observed by millisecond imaging of membrane property changes during the pulse*, *Biophysical Journal* **76**, 2158 (1999).
- [76] K. C. Smith, R. S. Son, T. Gowrishankar, and J. C. Weaver, *Emergence of a large pore subpopulation during electroporating pulses*, *Bioelectrochemistry* **100**, 3 (2014).
- [77] M. Yu and H. Lin, *Quantification of propidium iodide delivery with millisecond electric pulses: a model study*, arXiv preprint arXiv:1401.6954 (2014).
- [78] J. Li and H. Lin, *Numerical simulation of molecular uptake via electroporation*, *Bioelectrochemistry* **82**, 10 (2011).
- [79] J. C. Neu, K. C. Smith, and W. Krassowska, *Electrical energy required to form large conducting pores*, *Bioelectrochemistry* **60**, 107 (2003).
- [80] J. Li and H. Lin, *The current-voltage relation for electropores with conductivity gradients*, *Biomicrofluidics* **4**, 013206 (2010).
- [81] J. C. Weaver, K. C. Smith, A. T. Esser, R. S. Son, and T. Gowrishankar, *A brief overview of electroporation pulse strength–duration space: A region where additional intracellular effects are expected*, *Bioelectrochemistry* **87**, 236 (2012).

A fluorescence microscopy image of a cell, likely a yeast, showing intracellular DNA transport. The cell is stained with a blue dye (likely DAPI) to highlight the nucleus and other cellular structures. Several bright, magenta-colored spots are visible within the cell, representing the transport of DNA. The text "Intracellular DNA transport" is overlaid on the image in a white, italicized serif font.

*Intracellular DNA  
transport*

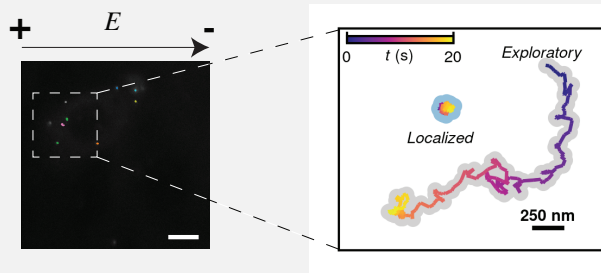


# 3

## COEXISTING ERGODIC AND NON-ERGODIC INTRACELLULAR TRANSPORT OF ELECTROTRANSFERRED DNA CARGO

### Highlights

- Trajectories of electrotransferred DNA cargo of different sizes is directly visualized in different cell lines.
- Intracellular electrotransferred DNA cargo is governed by coexisting ergodic and non-ergodic anomalous diffusion.
- The anomalous exponent of electrotransferred DNA cargo is strongly correlated to the cell's cancer state.



A preprint of this chapter is available as A. Muralidharan, H. Uitenbroek, and P.E. Boukany in *bioRxiv* [1].

*The ability of exogenous DNA cargo to overcome the active and viscoelastic eukaryotic cytoplasm is a principal determinant for the gene delivery efficacy. During DNA electrotransfer, DNA forms complexes with the membrane (DNA cargo) which is transported through the cytoplasm by passive diffusion and active mechanisms. However, this process is poorly understood limiting rational optimization of DNA cargo to be delivered to different cell types. We have investigated the intracellular transport of DNA cargo (of sizes 100 bp, 250 bp and 500 bp) delivered by electrotransfer to non-cancerous and cancerous mammalian cells. We demonstrate that intracellular DNA cargo transport is governed by coexisting ergodic and non-ergodic anomalous diffusion for all the tested DNA sizes and cell types. The apparent diffusion coefficient of the electrotransferred DNA cargo in the cytoplasm decreases when the DNA size is increased from 100 bp to 500 bp. Interestingly, the electrotransferred DNA cargo (500 bp) transport is strongly dependent on the cell's cancer state. Intracellular electrotransferred DNA cargo transport has a higher probability of superdiffusive transport and lower probability of caging in metastatic cells compared to malignant cells followed by benign cells.*

### 3.1. INTRODUCTION

Intracellular transport of exogenous cargo such as nucleic acids through the dense and active intracellular barrier is an indispensable step in biological processes such as cell transfection, up/down-regulation of gene expression, and gene editing [2–4]. Several physical and chemical strategies are currently employed for cell transfection by delivering nucleic acids such as RNA and DNA [5]. One of the safest and simplest physical methods to introduce the negatively charged nucleic acids to living cells is using pulsed electric fields (also called electrotransfer), which transiently disrupts the cell membrane [4, 5]. During the electrotransfer to living cells, small nucleic acids like naked siRNA [6] and DNA fragments [7] (15–22 base pair or bp) freely translocate across the permeabilized cell membrane while DNA fragments with size above 25 bp [7] and plasmid DNA (4.7 kbp) [8] form DNA-membrane complexes (or DNA cargo). Direct visualization of electrotransferred plasmid DNA cargo trajectories in the Chinese Hamster Ovary (CHO) cell cytoplasm demonstrated the presence of fast active transport alongside slow passive diffusion in the DNA cargo transport [9]. Classical endocytotic pathways facilitate subsequent transport of the DNA cargo through the cytoplasm [10–12]. Understanding the DNA cargo's intracellular transport is key to obtaining precise control over DNA electrotransfer efficacy.

What strategies does a cell employ to transport the mesoscopic cargo with a similar size as DNA cargo (0.1 - 0.5  $\mu\text{m}$  [8]) through the cytoplasm? Observations from the intracellular motion of exogenous cargo such as spherical beads [13, 14], carbon nanotubes [15] and nanoparticles [16, 17], and endogenous organelles such as endosomes [18, 19] and insulin granules [20] provide the basis for our current understanding of intracellular mesoscopic cargo transport [21–23]. Geometric constraints such as the cargo size, macromolecule crowding in the cytoplasm, and binding of the cargo to the cytoskeleton hinder diffusion [17, 24–26]. On the other hand, active forces generated by molecular motors on the cargo and cytoplasmic fluctuations can enhance diffusion and often facilitate directed motion [13–15, 19]. Hence, mesoscopic cargo's intracellular motion often deviates from Brownian motion and is classified as subdiffusive or su-

perdiffusive (or broadly as anomalous diffusion) depending on the randomness of the trajectory [27]. Such classifications, however, are often insufficient to characterize the cargo's complex motion in the cytoplasm. Mesoscopic cargo such as beads, insulin granules, chromosomal loci, and RNA-protein particles in both eukaryotic and prokaryotic cytoplasm perceive the cytoplasm as a viscoelastic media [13, 17, 28, 29]. Furthermore, the intracellular motion of insulin granules, nanoparticles, and quantum dots in non-cancer and cancer cell lines display ergodicity breaking, or non-equivalence between long-time-averaged motion and ensemble-averaged motion as the cargo can bind to the cytoplasmic components [17, 20, 27, 30]. To rationally optimize the intracellular DNA cargo transport, we should understand its intracellular transport across different DNA sizes (to mimic the geometric constraints) and cell types (with different intracellular activity levels).

In this work, we propose a unified framework for electrotransferred DNA cargo transport in the cytoplasm across different DNA sizes (100 bp, 250 bp, 500 bp) and cell types (animal cell line, benign, malignant, and metastatic breast carcinoma cell line). We demonstrate that the intracellular DNA cargo transport is composed of both ergodic and non-ergodic anomalous diffusion processes (with anomalous exponent  $\alpha$ ) for all tested DNA sizes and cell types. Increasing the size of the DNA from 100 bp to 500 bp decreases mean apparent intracellular (CHO-K1 cells) diffusion coefficient of the DNA cargo from  $1.8 \times 10^{-2} \mu\text{m}^2\text{s}^{-\alpha}$  to  $1.1 \times 10^{-2} \mu\text{m}^2\text{s}^{-\alpha}$ . The anomalous exponent of 500 bp DNA cargo motion in cytoplasm is strongly correlated to the cell's cancer state while the apparent diffusion coefficient is not. Electrotransferred DNA cargo in the cytoplasm has a higher probability to undergo superdiffusive motion in metastatic breast cancer cells compared to malignant followed by benign breast cancer cells.

## 3.2. MATERIALS AND METHODS

### 3.2.1. CELL CULTURE

The Chinese Hamster Ovary cells, CHO-K1 (DSMZ), were grown in T-flasks containing culture medium consisting of Nutrient Mixture Ham's F-12 (Sigma Aldrich) supplemented with  $\sim 10\%$  fetal bovine serum (Sigma Aldrich). MCF-7 (DSMZ) cells were cultured in Dulbecco's minimal essential medium (Sigma Aldrich) supplemented with  $\sim 10\%$  fetal bovine serum and 0.01 mg/ml human recombinant insulin (Gibco). MCF10A (ATCC) cells were cultured in DMEM/F12 Ham's Mixture (Gibco) supplemented with  $\sim 5\%$  horse serum (Gibco), 20 ng/ml human epidermal growth factor (EGF) recombinant protein (Invitrogen), 10  $\mu\text{g}/\text{ml}$  human recombinant insulin (Gibco), 0.5  $\mu\text{g}/\text{ml}$  hydrocortisone (Sigma Aldrich), 0.1  $\mu\text{g}/\text{ml}$  cholera toxin (Sigma Aldrich). MDA-MB-231 (ATCC) cells were cultured in DMEM supplemented with  $\sim 10\%$  fetal bovine serum.

The cells were incubated at  $37^\circ\text{C}$  with  $5\% \text{CO}_2$  and were sub-cultured every two days. Twenty-four hours before the electrotransfer of DNA,  $1 \times 10^4$  cells suspended in 500  $\mu\text{l}$  of culture medium were plated in one well of a four-well glass-bottom chambered coverslip ( $\mu$ -slide, Ibidi) with a growth area per well of  $2.5 \text{cm}^2$ .

### 3.2.2. DNA STAINING AND ELECTROTRANSFER PROTOCOL

10  $\mu\text{g}$  of DNA fragments (NoLimits DNA, Thermofisher) at a concentration of 0.5  $\mu\text{g}/\mu\text{l}$  in 10 mM Tris-HCl (pH 7.6) and 1 mM EDTA is stained using YOYO-1 dye (1 mM in DMSO, Thermofisher) at a bp:YOYO-1 dye molecule staining ratio of 5:1. The stained DNA fragments are then dissolved in the pulsing buffer (10 mM  $\text{Na}_2\text{HPO}_4/\text{KH}_2\text{PO}_4$ , 1 mM  $\text{MgCl}_2$ , 250 mM sucrose, pH 7.0-7.4) at a concentration of 3.33  $\mu\text{g}/\text{ml}$ .

The culture media from the chambered coverslips containing the cells is removed just before DNA electrotransfer. The cells are then washed three times with 500  $\mu\text{l}$  of pulsing buffer. 500  $\mu\text{l}$  of the stained DNA solution in the pulsing buffer (3.33  $\mu\text{g}/\text{ml}$ ) is added to each of the chambered coverslips. 10 electric pulses of 350 V/cm amplitude and 5 ms duration were applied at a frequency of 1 Hz through stainless steel electrodes placed parallel to each other 3 mm apart. The electrode configuration above is expected to provide uniform electric field lines. The electrodes are connected to a pulse generator (BETA tech) to deliver the electric pulses. After the electric pulses are delivered, the electrodes are removed and left to rest in the room temperature ( $\sim 22^\circ\text{C}$ ) for 10 minutes to allow resealing of the cell membrane. 500  $\mu\text{l}$  of culture media is then added to the cells (now in the DNA suspension). 500  $\mu\text{l}$  of the resulting solution is removed and the process is repeated three times to dilute the amount of free DNA in the solution. The cells are then placed back in the incubator for 15 minutes.

### 3.2.3. DNA TRACKING EXPERIMENTS

The fluorescence imaging experiments for tracking DNA cargo are performed on an inverted fluorescence microscope (Zeiss Axio-Observer Z1) coupled with an EMCCD camera (Andor ixon3) with a resolution of  $512 \times 512$  pixels. The stage of the microscope is coupled to an incubation system (Ibidi) which maintains the cells at  $37^\circ\text{C}$ , 5%  $\text{CO}_2$ , and  $> 90\%$  humidity. A  $100\times/1.2$  oil immersion objective (Zeiss Acroplan) magnifies the image to a field of view of  $81.92 \times 81.92 \mu\text{m}^2$ . An HXP 120C lighting unit (Zeiss, Germany) coupled with a ET-EGFP filter set (excitation: 470 nm/emission: 525 nm) is used as the light source for fluorescence imaging of YOYO-1 stained DNA. The trajectory of internalized DNA is recorded as a time series of 350 images (14 bit) with an exposure time of 100 ms at a camera streaming mode, resulting in a frequency of 10 frames per second. The images were acquired by focusing on a plane with sharp fluorescent DNA cargo. The recorded trajectory is a two dimensional projection of the trajectory of the DNA cargo. The tracking experiments are done between 20 minutes and 1 hour after the application of electric pulses.

### 3.2.4. DATA ANALYSIS

One to five DNA aggregates were observed per cell after electrotransfer. The background noise and larger particles in the image time series is removed by applying an appropriate band pass filter through a home-made script written in Python. The position  $\mathbf{r}$  of the individual DNA cargo are detected using customized version of Trackpy package written in Python [31]. The analysis of the data is then performed by home-made scripts written in Python. The following packages in Python were used in this research: Trackpy, Numpy, Scipy, Pandas and Matplotlib.

### 3.2.5. STATISTICAL ANALYSIS

The statistical analysis was performed using one way analysis of variance (ANOVA) in Python. The statistical analysis was further confirmed using two sided T tests in Python. \*:  $P < 0.05$ , \*\*:  $P < 0.01$ , \*\*\*:  $P < 0.001$ , \*\*\*\*:  $P < 0.0001$ .

## 3.3. RESULTS AND DISCUSSIONS

### 3.3.1. ANALYSIS OF INTRACELLULAR DNA CARGO TRAFFICKING

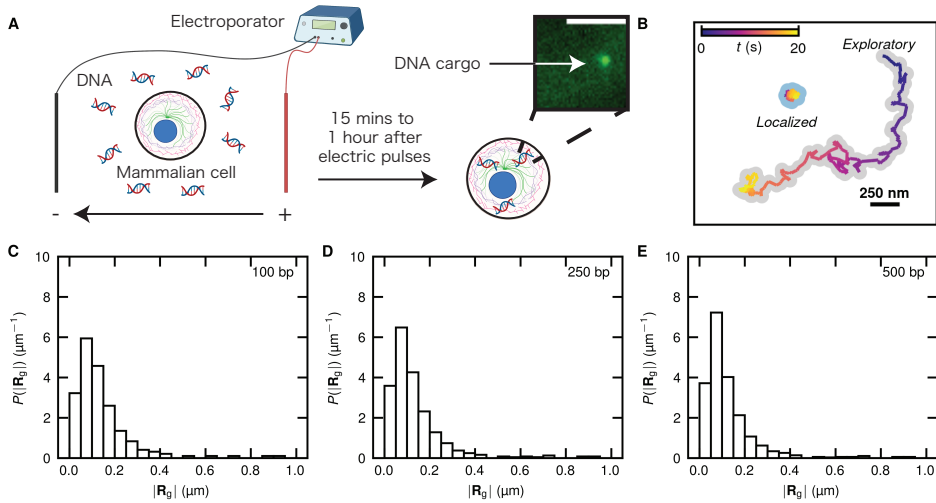


Figure 3.1: Different intracellular DNA cargo transport modes. (A) A schematic of delivery of DNA cargo to mammalian cells. Ten electric pulses of 350 V/cm with a duration of 5 ms and a frequency of 1 Hz are applied to deliver YOYO-1 labelled DNA fragment to mammalian cells. DNA-membrane complexes (DNA cargo) are formed and internalized by the cell. The direct visualization of the intracellular DNA cargo transport is performed by fluorescent microscopy between 15 minutes and 1 hour after the electric pulses are applied. A representative fluorescent image of 100 bp DNA cargo inside a CHO-K1 cell is shown. The scale bar represents 5  $\mu\text{m}$ . The schematic is created with BioRender. (B) Two example trajectories displaying localized motion covering small distances and exploratory motion covering larger distances. The trajectories are colored according to the time from the starting position. (C)-(E) The probability density distribution (bin size = 0.05  $\mu\text{m}$ ) of the radius of gyration  $R_g$  ( $T = 20$  s) of the DNA cargo trajectories for (C) 100 bp ( $n = 191$  trajectories from 38 cells), (D) 250 bp ( $n = 99$  trajectories from 39 cells), (E) 500 bp ( $n = 210$  trajectories from 34 cells) DNA in CHO-K1 cell cytoplasm.

To understand the intracellular DNA cargo transport, we study the DNA cargo trajectories after they are internalized (between 20 to 60 minutes after electrotransfer) by the CHO-K1 cells. A representative example of Chinese Hamster Ovary cells (CHO-K1, DSMZ) with internalized fluorescently labeled DNA cargo is shown in Fig. 3.1A. The steric interactions of the DNA cargo with the cytoplasm results in the confinement of the trajectories within the cytoskeletal meshwork, and the biochemical interactions with molecular motors during active transport lead to distinctly long trajectories (as schematically represented in Fig. 3.1B). As a first step, we used DNA cargo formed by electrotransferred DNA fragments (of sizes 100 bp, 250 bp, and 500 bp) to emulate different levels of



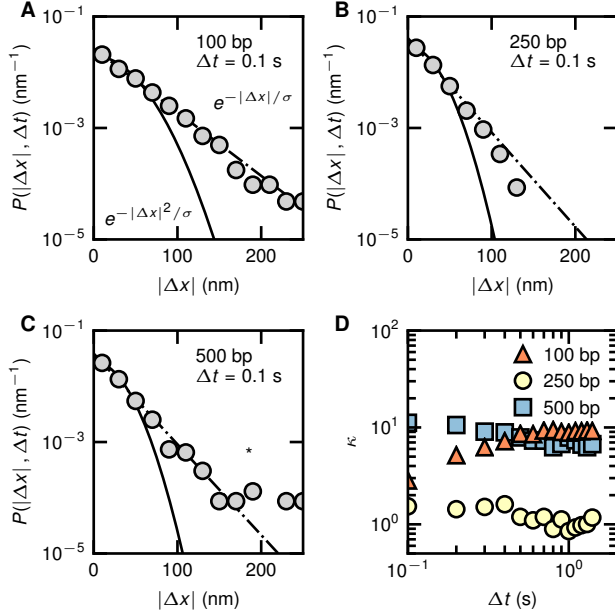


Figure 3.2: Non-Gaussian DNA cargo displacements. Probability density distribution (bin size = 20 nm) for one dimensional intracellular DNA cargo displacement during a time interval of  $\Delta t = 0.1$  s is plotted for (A) 100 bp (B) 250 bp and (C) 500 bp DNA. The displacements in  $x$  and  $y$  directions are collected together for better statistics. The solid line represents a Gaussian fit to the center of the distribution while the dash-dot line represents a Laplacian fit to the entire distribution. The asterisk (\*) in (C) represents the location where the distribution deviates from the Laplacian distribution. (D) Deviation from Gaussianity is represented by excess kurtosis  $\kappa$  for different  $\Delta t$  for the 100, 250 and 500 bp DNA.

steric interactions with the cytoplasm. To quantify the different length scales explored by the DNA cargo, we estimate the radius of gyration  $\mathbf{R}_g(T)$  of the individual trajectories, where  $\mathbf{R}_g^2(T) = N^{-1} \sum_{i=1}^N |\mathbf{r}_i(T) - \mathbf{r}_{\text{com}}(T)|^2$  and  $T$  is the measurement time [32]. The individual trajectories were sampled as  $N$  points with positions  $\mathbf{r}_i$  and have a center of mass  $\mathbf{r}_{\text{com}}$  (assuming same mass at all points). The probability densities of  $|\mathbf{R}_g|$  at  $T = 20$  s of the DNA cargo trajectories for different DNA fragment sizes are plotted in Fig. 3.1 C-E. The majority of the DNA cargo display localized displacements ( $|\mathbf{R}_g| \sim 75$  nm) for all DNA sizes. The peak of the probability density distribution from  $|\mathbf{R}_g|$  of the trajectories is close to the characteristic actin mesh size (100-200 nm) in a living cell [33]. The DNA cargo traverse up to  $|\mathbf{R}_g| \sim 950$  nm within 20 seconds for all DNA fragment sizes. The localized and exploratory intracellular electrotransferred DNA cargo transport was previously reported in plasmid DNA cargo delivered to CHO cells and is dependent on the cell's cytoskeleton state [9].

Having established that the DNA cargo can explore different length scales, we investigate its one dimensional displacement at different lag times. For a particle performing ideal random Brownian walk in a simple Newtonian fluid, the probability density of one dimensional displacement  $P(|\Delta x|, \Delta t)$  exhibits a Gaussian distribution ( $P(|\Delta x|) \sim$

$\exp(-|\Delta x|^2/\sigma)$ , where  $\sigma$  is a scale parameter) by the virtue of the central limit theorem [34]. One-dimensional displacement  $\Delta x$  is defined as  $x(t + \Delta t) - x(t)$ , where  $x(t)$  is the DNA position at time  $t$  (in either  $x$  or  $y$  direction), and  $\Delta t$  is the time interval between the DNA position measurements. The displacements in  $x$  and  $y$  directions are combined to improve statistics. We plot the probability density of the absolute value of the intracellular one dimensional DNA cargo displacements,  $P(|\Delta x|, \Delta t)$ , for  $\Delta t = 0.1$  s is plotted in Figs. 3.2A-C.  $P(|\Delta x|, \Delta t)$  follows a Laplacian distribution ( $P(|\Delta x|) \sim \exp(-|\Delta x|/\sigma)$ ) for the majority of the distribution, displaying enhanced probability for the cargo to make large displacements compared to a regular Brownian motion. The cytoplasmic heterogeneity (which results in a broad distribution of diffusivities of DNA cargo within the cytoplasm), non-thermal active fluctuations and fast active endocytotic transport of DNA cargo [10] results in a deviation from Gaussianity reflecting the coexistence of fast and slow DNA cargo [29]. We quantify the deviation from Gaussian behavior by excess kurtosis,  $\kappa = \langle \Delta x^4 \rangle / \langle \Delta x^2 \rangle^2 - 3$ . For a Gaussian distribution,  $\kappa = 0$ , and distribution with longer tails compared to Gaussian display  $\kappa > 0$ .  $P(|\Delta x|, \Delta t)$  remains leptokurtic ( $\kappa > 0$ ) for all DNA sizes. If the long exponential tails in the displacement probability distribution arise from continuous drift ( $\sim \Delta t$ ) due to active transport,  $\kappa$  would grow with lag time as the exponential tails would grow faster compared to its passive diffusion counterpart represented by a Gaussian ( $\sqrt{\Delta t}$ ). Fig. 3.2D shows that non-Gaussian statistics is maintained even at longer lag times. 100 bp DNA cargo showed an increase in  $\kappa$  with  $\Delta$ , while 250 bp DNA cargo showed no visible correlation with  $\Delta t$ , and 500 bp DNA cargo showed a decrease in  $\kappa$  with  $\Delta t$ . We find that the larger displacements appear as intermittent spikes rather than continuous drift with the same velocity from the DNA cargo trajectories (Fig. 3.6, appendix). Such bursts of large active transport are consistent with the view that endosomal transport involves stress buildup in the cytoskeleton followed by a rapid release and can explain the weak correlation of  $\kappa$  with  $\Delta t$  [18]. We conclude that the physical mechanism that can describe the intracellular DNA cargo transport should have non-Gaussian displacements. We investigate the influence of the DNA size on the DNA cargo's cytoplasmic mobility in the following section.

### 3.3.2. INTRACELLULAR ANOMALOUS DIFFUSION OF DNA CARGO

To evaluate how the cytoplasmic mobility of DNA cargo varies with DNA size, we estimate the relation between mean square displacement

$$\overline{\Delta \mathbf{r}^2(\Delta t, T)} = \frac{1}{T - \Delta t} \int_0^{T - \Delta t} [\Delta \mathbf{r}(t + \Delta t) - \Delta \mathbf{r}(t)]^2 dt \quad (3.1)$$

and lag time  $\Delta t$ .  $\overline{\Delta \mathbf{r}^2(\Delta t, T)}$  is plotted against  $\Delta t$  for  $T = 10$  s in Figs. 3.3A-C to characterize the intracellular transport. Individual  $\overline{\Delta \mathbf{r}^2(\Delta t, T)}$  trajectories for all the sizes of DNA (colored in gray) is spread over two orders of magnitude demonstrating that the cargo trajectories are heterogeneous.  $\overline{\Delta \mathbf{r}^2(\Delta t, T)}$  increases with  $\Delta t$  and deviates from linearity. Furthermore,  $\overline{\Delta \mathbf{r}^2(\Delta t, T)}$  display two distinct scaling with  $\Delta t$ , with  $\overline{\Delta \mathbf{r}^2(\Delta t, T)} \sim \Delta t^{\alpha_1}$  when  $\Delta t < 1$  s, and  $\overline{\Delta \mathbf{r}^2(\Delta t, T)} \sim \Delta t^{\alpha_2}$  when  $\Delta t > 1$  s.  $\alpha_1$  and  $\alpha_2$  are power law exponents and  $\Delta t \sim 1$  s is a characteristic cross-over lag time. Mean square displacement from individual trajectories are fitted to  $\overline{\Delta \mathbf{r}^2(\Delta t, T)} = D_{\text{app},i} \Delta t^{\alpha_i}$  ( $i = 1, 2$ ) to determine the appar-

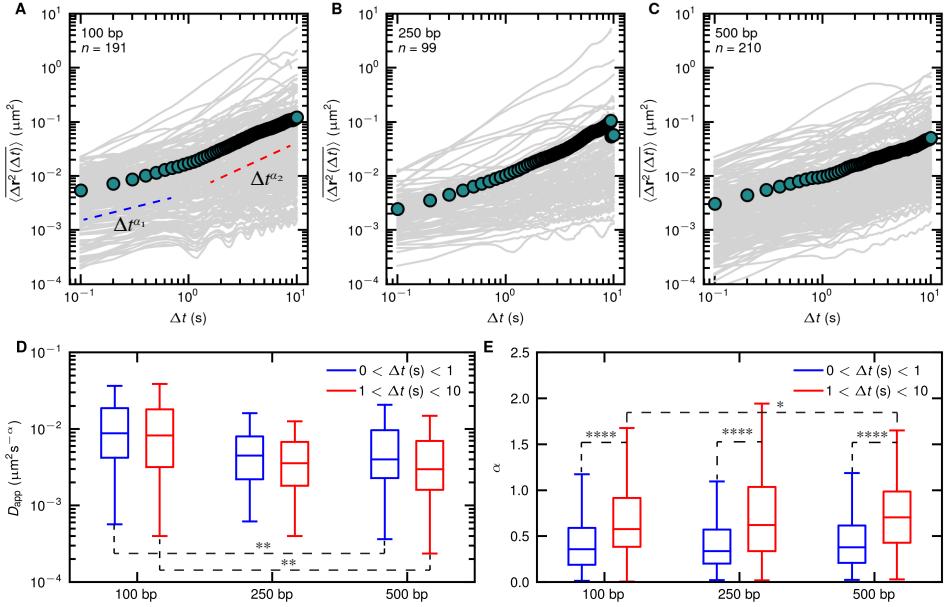


Figure 3.3: Intracellular anomalous DNA cargo transport. Individual time averaged mean square displacements  $\langle \Delta r^2(\Delta t, T) \rangle$  are plotted in solid gray color for (A) 100 bp (B) 250 bp (C) 500 bp DNA against the lag time  $\Delta t$ , for a measurement time  $T = 10$  s. The green circles represent the ensemble and time average mean square displacement  $\langle \overline{\Delta r^2(\Delta t, T)} \rangle$ . (D) The apparent diffusion coefficient  $D_{\text{app}}$ , and (E) anomalous exponent  $\alpha$  obtained by fitting the individual  $\overline{\Delta r^2(\Delta t, T)}$  to  $\overline{\Delta r^2(\Delta t, T)} = D_{\text{app}} \Delta t^\alpha$  before and after the cross-over  $\Delta t = 1$  s is plotted as a box plot for different DNA sizes. Statistical significance of difference of the mean was tested using one way analysis of variance. \*:  $P < 0.05$ , \*\*:  $P < 0.01$ , \*\*\*:  $P < 0.001$ , \*\*\*\*:  $P < 0.0001$ . Non significant differences between the datasets were not displayed for better clarity of the figure.

ent diffusion coefficient  $D_{\text{app}}$  and the anomalous power-law exponent using non-linear regression.  $\alpha_1$  is determined during the interval  $\Delta t = 0.1$  s and  $\Delta t = 0.8$  s and  $\alpha_2$  is determined during the interval  $\Delta t = 2$  s and  $\Delta t = 5$  s to avoid biases at the edge of the cross-over lag time. Fig. 3.3D-E shows that the trajectories display marked heterogeneity in both  $D_{\text{app},i}$  and  $\alpha_i$  estimated before and after the cross-over lag time.  $D_{\text{app},i}$  is spread over two to three orders of magnitude as seen in Fig. 3.3D (the whole population is presented in Fig. 3.9, appendix as a 2D density plot) for all DNA sizes. Fig. 3.3D shows that there is no statistically significant ( $P > 0.05$ ) difference between  $D_{\text{app},1}$  and  $D_{\text{app},2}$  within each DNA size. The arithmetic mean,  $\langle D_{\text{app},1} \rangle$  decreases from  $\sim 1.8 \times 10^{-2} \mu\text{m}^2\text{s}^{-\alpha}$  (standard error of the mean, s.e.m.  $\sim 2 \times 10^{-3} \mu\text{m}^2\text{s}^{-\alpha}$ ) for 100 bp DNA to  $\sim 1.1 \times 10^{-2} \mu\text{m}^2\text{s}^{-\alpha}$  (s.e.m.  $\sim 1.4 \times 10^{-3} \mu\text{m}^2\text{s}^{-\alpha}$ ) for 500 bp DNA ( $P < 0.01$ ). Similarly, the arithmetic mean of the diffusion coefficient  $\langle D_{\text{app},2} \rangle$  decreases from  $\sim 2 \times 10^{-2} \mu\text{m}^2\text{s}^{-\alpha}$  (standard error of the mean, s.e.m.  $\sim 3.8 \times 10^{-3} \mu\text{m}^2\text{s}^{-\alpha}$ ) for 100 bp DNA to  $\sim 1.2 \times 10^{-2} \mu\text{m}^2\text{s}^{-\alpha}$  (s.e.m.  $\sim 2.7 \times 10^{-3} \mu\text{m}^2\text{s}^{-\alpha}$ ) for 500 bp DNA ( $P < 0.01$ ). No significant differences in  $D_{\text{app},i}$  were observed between 100 bp and 250 bp DNA cargo, and 250 bp and 500 bp DNA cargo. Our results suggest that viscous dissipation due to increasing DNA cargo size might be

responsible for reduction in the diffusion coefficient.

To classify the randomness of the trajectory, we then analyse the anomalous exponents  $\alpha_i$  for the different DNA fragment sizes. The value of  $\alpha_i$  contains information about the driving forces of the cargo transport. For Brownian motion  $\alpha_i = 1$  [35]. The motion of the cargo in a viscoelastic or crowded environment like the cytoplasm result in  $\alpha_i < 1$ . Only motion with non-thermal driving force, for e.g., active forces can lead to superdiffusive motion with an anomalous exponent  $\alpha_i > 1$ . Both  $\alpha_1$  and  $\alpha_2$  display trajectory to trajectory fluctuations for all sizes of DNA, and showed either caged ( $\alpha_i < 0.4$ ), subdiffusive ( $0.4 < \alpha_i < 1$ ) and superdiffusive power law scaling as seen in Fig. 3.3E. Approximately 60 % of the trajectories are caged and  $\sim 35$  % subdiffusive when  $\Delta t < 1$  s as shown in Fig. S5 (appendix) for all sizes of DNA. For all the DNA sizes, the anomalous exponent showed a significant ( $P < 0.0001$ ) increase after the cross-over lag time of 1 s. The anomalous exponent before  $\Delta t \sim 1$  s was independent of DNA size. After the cross-over, the majority of the trajectories ( $\sim 60\%$ ) are subdiffusive,  $\sim 20\%$  caged and  $\sim 20\%$  superdiffusive. Furthermore, there was a significant ( $P < 0.05$ ) increase in the anomalous exponent between 100 bp DNA cargo and 250 bp DNA cargo after the crossover. No significant differences were observed between other combinations of DNA size. The arithmetic mean of the anomalous exponents  $\langle \alpha_1 \rangle \sim 0.42$  (s.e.m.  $< 0.03$ ) for all the DNA sizes and  $\langle \alpha_2 \rangle \sim 0.61$  (s.e.m.  $\sim 0.03$ ) for 100 bp,  $\sim 0.64$  (s.e.m.  $\sim 0.05$ ) for 250 bp and  $\sim 0.72$  (s.e.m.  $\sim 0.03$ ) for 500 bp DNA. Fig. 3.3E shows that the median  $\alpha$  increases from  $\sim 0.4$  to  $\sim 0.7$  after the cross-over  $\Delta t \sim 1$  s.

What mechanisms lead to the observed anomalous diffusion of the DNA cargo? Multiple molecular motors drag the DNA cargo encapsulated in endosomes [10] along microtubule tracks through viscoelastic cytoplasm [19]. The intracellular motion of endosomes therefore involve stress buildup in the cytoplasm followed by bursts of active motion [18]. The increasing size of the cargo is reported to increase the resistance faced from the cytoplasm and can stall the motion while the cooperative action of molecular motors facilitates directionality [19]. Increasing DNA size from 100 bp to 500 bp showed a decrease ( $\sim 64\%$ ) in the apparent diffusion coefficient  $D_{app,1}$  (and  $D_{app,2}$ ). A plausible explanation for this observed decrease in  $D_{app,i}$  is the potential increase in the cytoplasmic resistance due to the larger cargo size. In contrast, despite the expectation that the larger cargo enhances the cytoplasm's resistance and decreases the probability for exhibiting directionality and superdiffusive motion, increasing the DNA size from 100 bp to 500 bp increased  $\alpha_2$ . Other combinations of DNA sizes had no statistically significant differences in  $\alpha_i$ . To further investigate the influence of the DNA size on the randomness of the DNA cargo trajectory, we estimate the directional change angle  $\theta(t, \Delta t)$  defined such that

$$\cos\theta(t, \Delta t) = \frac{\Delta \mathbf{r}(t) \cdot \Delta \mathbf{r}(t + \Delta t)}{|\Delta \mathbf{r}(t)| |\Delta \mathbf{r}(t + \Delta t)|}, \quad (3.2)$$

where the lag time  $\Delta t$  represents the temporal coarsening and  $\Delta \mathbf{r}$  is the displacement vector [36]. The directional change probability density distribution is plotted in Fig. 3.8 (appendix). At short temporal coarsening ( $\Delta t = 0.1$  s), the distribution shows a peak at  $\pi$  rad, indicating that an anti-persistent motion is dominant at short time scales and leads to the observed caged like motion before the cross over lag time. Further increasing  $\Delta t$ , the trajectories become more directional, increasing the anomalous exponent after the

cross over lag time (Fig. 3.8D). The directional change probability density distribution and DNA size had no statistically significant correlation. This leads us to conclude that the DNA size does not significantly alter molecular motor's ability to overcome the cytoplasm's viscoelastic resistance and actively transport the electrotransferred DNA cargo. We probe into the physical models of anomalous diffusion which can best describe DNA cargo transport in the following section. To do so, we check for ergodicity breaking in the DNA cargo dynamics.

## 3

### 3.3.3. COEXISTENCE OF NON-ERGODIC AND ERGODIC PROCESSES IN THE INTRACELLULAR DNA CARGO DYNAMICS

To understand if the statistical properties obtained from individual trajectories during the observation time represent the ensemble behavior, we test if the DNA cargo motion is ergodic. As a first step towards checking for ergodicity, we plot the time-averaged mean squared displacement for individual trajectories for different measurement times  $T$  and lag time  $\Delta t = 0.1$  s in Figs. 3.4A-C [37]. We use overlines to denote time averages and angular brackets to denote ensemble averages. The mean square displacements of different cargo trajectories at the 0.1 s interval are scattered over three orders of magnitude for all tested DNA sizes. The scatter of mean square displacement is more pronounced at short measurement times due to the lower denoising strength from lower degree of averaging. As the measurement time increases, the number of points per sample in averaging increases reducing the noise in the mean square displacement. The dependence of  $\overline{\Delta r^2(\Delta t, T)}$  on the measurement time  $T$  is analyzed by fitting the data to a power law of the form  $T^\beta$  for each trajectory, where  $\beta$  is the power-law exponent. The fitting is performed between  $T = 0.8$  s and  $T = 10$  s to avoid errors due to noise in the data at low measurement times. The probability distribution of  $\beta$  for the different sizes of DNA is provided in Fig. 3.7 (appendix). For most of the trajectories for all DNA sizes,  $P(\beta) \sim T^0$ . Some of the trajectories display a decrease while some display an increase in  $\overline{\Delta r^2(\Delta t, T)}$  with  $T$ . Despite the strong heterogeneity at the single trajectory level, the ensemble average  $\langle \overline{\Delta r^2(\Delta t, T)} \rangle$  is independent of the measurement time ( $\sim T^0$ ). The power-law dependence of the mean square displacement with measurement time is often seen in non-ergodic systems. To quantify the degree of amplitude fluctuations of individual  $\overline{\Delta r^2(\Delta t, T)}$ , the ergodicity breaking parameter

$$EB = \frac{\langle (\overline{\Delta r^2(\Delta t, T)})^2 \rangle - \langle \overline{\Delta r^2(\Delta t, T)} \rangle^2}{\langle \overline{\Delta r^2(\Delta t, T)} \rangle^2} \quad (3.3)$$

is calculated [37–39].  $EB$  represents the spread of individual  $\overline{\Delta r^2(\Delta t, T)}$  and hence, the heterogeneity in the intracellular DNA cargo diffusion. For an ergodic process,  $EB = 0$  when  $T \rightarrow \infty$  as there is no amplitude fluctuations in  $\overline{\Delta r^2(\Delta t, T)}$  [27]. Fig. 3.4D shows that  $EB$  converges to  $EB \sim 1$  with increasing measurement time for 100 bp and 250 bp DNA and  $EB \sim 2$  for 500 bp DNA, showing that intracellular DNA motion after electroporation is non-ergodic.

Can a unified framework describe the DNA cargo's non-ergodic anomalous diffusion with non Gaussian displacements? Simple Brownian walk slowed down by molecular crowding in the cytoplasm is insufficient to explain the observed heterogeneity in the

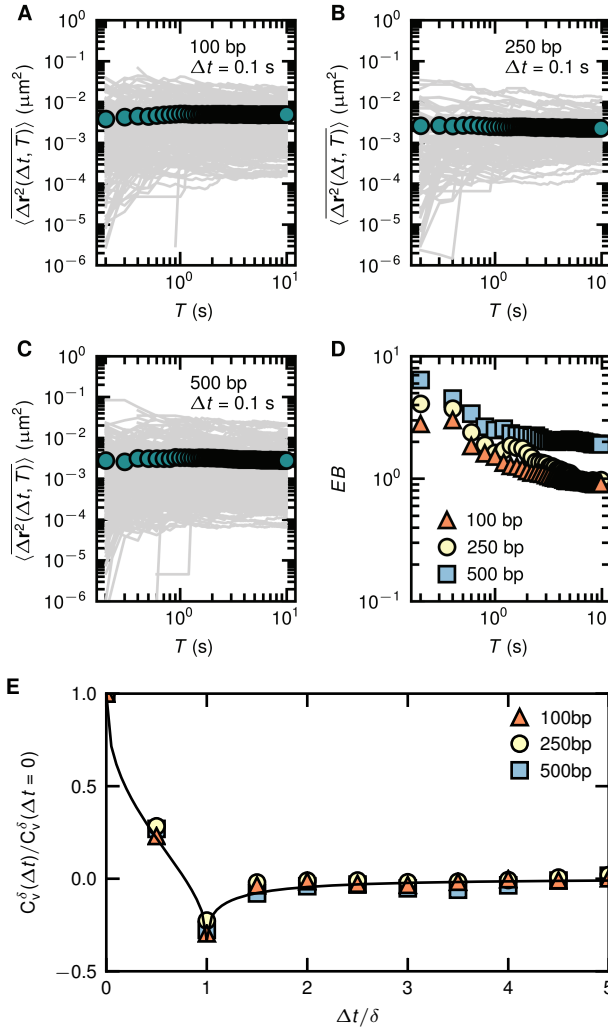


Figure 3.4: Coexistence of ergodic and non-ergodic processes in the intracellular DNA cargo dynamics. (A)-(C) Individual time averaged mean square displacements  $\langle \Delta r^2(\Delta t, T) \rangle$  are plotted in solid gray color for (A) 100 bp (B) 250 bp (C) 500 bp DNA against the measurement time  $T$ , for a lag time  $\Delta t = 0.1$  s. The green circles represent the ensemble and time average mean square displacement  $\langle \langle \Delta r^2(\Delta t, T) \rangle \rangle$ . (D) The ergodicity breaking parameter  $EB$  is plotted against the measurement time  $T$ . (E) Velocity auto-correlation function  $C_v^{\delta}(\Delta t) = \langle \mathbf{v}(t + \Delta t) \cdot \mathbf{v}(t) \rangle$ , where  $\mathbf{v}(t) = [\mathbf{r}(t + \delta) - \mathbf{r}(t)]/\delta$  normalized by  $C_v^{\delta}(\Delta t = 0)$  plotted against the lag time  $\Delta t$  normalized by the discretization time interval  $\delta = 0.2$  s for 100, 250 and 500 bp DNA. The solid line is the analytical prediction from fractional Brownian motion (FBM), Eq. 3.5 with  $\langle \alpha \rangle = 0.42$ .

mean square displacement. Continuous time random walk [27] (CTRW), where the trajectories consist of random steps which are broadly distributed in time, or fractional Brownian motion [40] (FBM), where the trajectories consist of random steps which are

broadly distributed in space are often used to model heterogeneous intracellular mesoscopic cargo motion. A distinguishing statistical property of CTRW from FBM is that CTRW is non-ergodic. During biological processes like intracellular insulin granule transport in pancreatic  $\beta$ -cells [20] and membrane diffusion of voltage-gated potassium channels in human embryonic kidney cells [41], ergodic FBM and non-ergodic CTRW coexist. While the ergodicity breaking suggests that DNA cargo motion follows a CTRW, the DNA cargo mean square displacement does not plateau with  $\Delta t$  as typically observed in a CTRW. Furthermore, we did not find any evidence for intermittent stalling in our trajectories (Fig. 3.6, appendix) which is a signature of CTRW. These observations lead us to hypothesise that an ergodic FBM process coexists with the CTRW. To check whether our data can be described by ergodic FBM, we proceed to calculate the velocity autocorrelation function

$$C_v^\delta(\Delta t) = \overline{\langle \mathbf{v}(t + \Delta t) \cdot \mathbf{v}(t) \rangle}, \quad (3.4)$$

where  $\mathbf{v}(t) = [\mathbf{r}(t + \delta) - \mathbf{r}(t)] / \delta$ , for discretization time interval  $\delta = 0.2$  s [28, 42, 43]. Fig. 3.4E shows that all the DNA sizes have a negative autocorrelation ( $C_v^\delta(\Delta t) / C_v^\delta(\Delta t = 0) \sim -0.28$ ) or memory at  $\Delta t / \delta = 1$  before levelling off at zero. The velocity autocorrelation is independent of the DNA size used. Such anti-correlated motion is exhibited by cargo undergoing ergodic fractional Brownian walk (FBM) [44]. Fig. 3.4E shows that the velocity anticorrelation function shows good agreement (root mean square error = 0.29) with the analytical predictions of FBM [26, 27]

$$C_v^\delta(\epsilon) = [(\epsilon + 1)^\alpha + |\epsilon - 1|^\alpha - 2\epsilon^\alpha] / 2 \quad (3.5)$$

where  $\epsilon = \Delta t / \delta$ , with  $\alpha = \langle \alpha_1 \rangle = 0.42$  (obtained in the previous section). The velocity autocorrelation function is self similar over discretization time interval as shown in Fig. 3.11 (appendix). The directional change distribution plotted in Fig. S3A (appendix) which shows a peak directional change of  $\pi$  rad at  $\Delta t = 0.1$  s corroborates the short lag time ( $\sim \Delta t = 0.1$  s) anti-persistent motion. At further temporal coarsening ( $\Delta t = 0.5$  s and  $\Delta t = 1$  s), the peak shifts towards 0 rad and  $2\pi$  rad indicating emergence of directional inertial motion at long lag times (Fig. S3B-D, appendix).

Overall, our data presents evidence that ergodic and non-ergodic processes coexist in intracellular electrotransferred DNA cargo transport. Non-ergodic processes like CTRW originate from transient binding and unbinding of the molecular motors which are attached to the cargo with different components of the cytoplasm. Our experiments display characteristic signatures of CTRW including ergodicity breaking and non-Gaussianity. The ergodic FBM characteristics exhibited by the DNA cargo potentially originates from the intracellular fluctuations. Hence, both the cargo and the cytoplasmic environment potentially govern the intracellular DNA cargo dynamics. To keep the permeabilization area during electroporation constant in our studies, we did not chemically perturb the cytoskeleton and the molecular motors [45]. In the following section, we study the influence of different levels of cytoplasmic activity (by using breast cancer cells at different stages of cancer) on the intracellular DNA cargo transport.

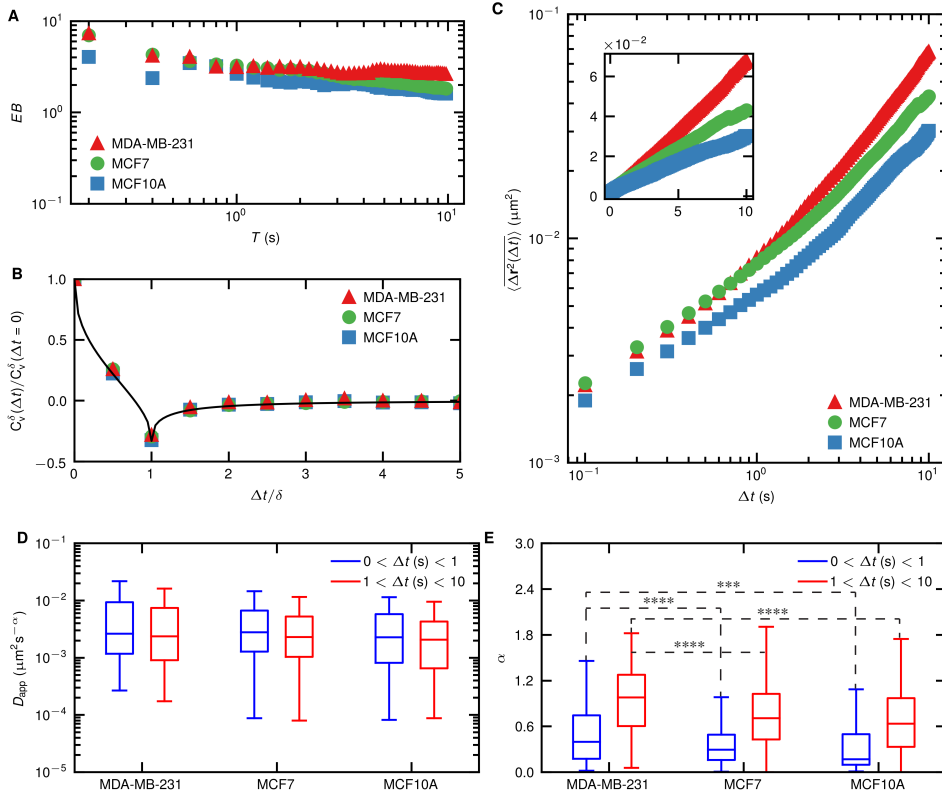


Figure 3.5: Influence of the cell's cancer state on the intracellular 500 bp DNA cargo dynamics. MCF10A cells are benign, MCF7 are malignant and MDA-MB-231 cells are metastatic breast cancer cells. (A) Ergodicity breaking parameter  $EB$  estimated for  $\Delta t = 0.1$  s is plotted against measurement time  $T$ . (B) Velocity auto-correlation function  $C_v^\delta(\Delta t) = \langle \mathbf{v}(t + \Delta t) \cdot \mathbf{v}(t) \rangle$ , where  $\mathbf{v}(t) = [\mathbf{r}(t + \delta) - \mathbf{r}(t)]/\delta$  normalized by  $C_v^\delta(\Delta t = 0)$  plotted against the lag time  $\Delta t$  normalized by the discretization time interval  $\delta = 0.2$  s for the cancer cell lines. The solid line is the analytical prediction from fractional Brownian motion (FBM), Eq. 3.5. (C) Ensemble and time averaged mean square displacement  $\Delta r^2(\Delta t, T)$  is plotted against the lag time  $\Delta t$  for the cancer cell lines (measurement time  $T = 10$  s). The plot is shown in linear scale in the inset. (D) The apparent diffusion coefficient  $D_{app}$ , and (E) anomalous exponent  $\alpha$  obtained by fitting the individual  $\Delta r^2(\Delta t, T)$  to  $\Delta r^2(\Delta t, T) = D_{app} \Delta t^\alpha$  before and after the cross-over  $\Delta t = 1$  s is plotted as a box plot for different cancer cell lines. Statistical significance of difference of the mean was tested using one way analysis of variance. \*:  $P < 0.05$ , \*\*:  $P < 0.01$ , \*\*\*:  $P < 0.001$ , \*\*\*\*:  $P < 0.0001$ .  $\alpha$  between the two time scales are significantly different for all cell lines ( $P < 0.0001$ ) but are not shown for better clarity. Non significant difference between the datasets were not displayed for better clarity of the figure. 133 trajectories (from 63 cells) were analyzed for MDA-MB-231 cells, 628 trajectories (from 98 cells) were analyzed for MCF7 cells, and 130 trajectories (from 60 cells) were analyzed for MCF10A cells.

### 3.3.4. INFLUENCE OF CELL'S STATE ON THE ELECTROTRANSFERRED DNA CARGO TRANSPORT

To understand the influence of the cell's cancer state on the DNA cargo transport, we studied the intracellular transport of 500 bp DNA cargo through breast cancer cells of



varying activity. We chose the following cell lines, which have an increasing level of intracellular activity: MCF10A (benign), MCF7 (malignant), and MDA-MB-231 (metastatic) [14, 46]. Ergodicity breaking in the DNA cargo transport is present in all the cancer cell lines with varying activity levels in Fig. 3.5A. Like CHO-K1 cells,  $EB$  for 500 bp DNA cargo trajectories of all the cancer cell lines studied converges to  $EB \sim 2 - 3$ . The FBM analytical solution describes the velocity autocorrelation function well for the DNA cargo transport in the cancer cells as shown in Fig. 3.5B. Our combined results from animal and human breast cancer (at different cancer states) cell lines lead us to propose that coexisting ergodic, and non-ergodic transport could be a universal strategy employed by eukaryotic adherent cell lines for intracellular transport of electrotransferred DNA cargo.

To study the influence of the cell's intrinsic activity on the cytoplasmic mobility of the DNA cargo we plot the  $\langle \overline{\Delta r^2(\Delta t)} \rangle$  for with measurement time  $T = 10$  s in Fig. 3.5C.  $\langle \overline{\Delta r^2(\Delta t)} \rangle$  increases from  $\sim 3 \times 10^{-2} \mu\text{m}^2$  in benign cells to  $\sim 4 \times 10^{-2} \mu\text{m}^2$  in malignant cells and  $\sim 7 \times 10^{-2} \mu\text{m}^2$  in metastatic cells at  $\Delta t = 10$  s. This shows that electrotransferred DNA cargo traverse longer distances in the cytoplasm of the cells with higher activity. The individual time averaged mean squared displacement show strong heterogeneity over different cell lines as shown in Fig. 3.12 (appendix). The two distinct scaling with  $\Delta t$  with a cross-over  $\Delta t \sim 1$  s is present for the  $\langle \overline{\Delta r^2(\Delta t)} \rangle$  of DNA cargo in cancer cell lines similar to the experiments performed with CHO-K1 cells.  $D_{\text{app},i}$  and  $\alpha_i$  govern the relation of  $\langle \overline{\Delta r^2(\Delta t)} \rangle$  with  $\Delta t$ . To understand why cells with higher intracellular activity have higher  $\langle \overline{\Delta r^2(\Delta t)} \rangle$ , we estimate  $D_{\text{app},i}$  and  $\alpha_i$  for the cancer cell lines. The ensemble average  $\langle D_{\text{app},1} \rangle$  for the 500 bp DNA cargo is  $\sim 8.1 \times 10^{-3} \mu\text{m}^2\text{s}^{-\alpha}$  (s.e.m  $\sim 1.2 \times 10^{-3} \mu\text{m}^2\text{s}^{-\alpha}$ ) for MDA-MB-231 cells,  $\sim 7.4 \times 10^{-3} \mu\text{m}^2\text{s}^{-\alpha}$  (s.e.m  $\sim 0.7 \times 10^{-3} \mu\text{m}^2\text{s}^{-\alpha}$ ) for MCF7 cells, and  $\sim 5.7 \times 10^{-3} \mu\text{m}^2\text{s}^{-\alpha}$  (s.e.m  $\sim 0.8 \times 10^{-3} \mu\text{m}^2\text{s}^{-\alpha}$ ) for MCF10A cells. The ensemble average  $\langle D_{\text{app},2} \rangle$  for the 500 bp DNA cargo is  $\sim 8.9 \times 10^{-3} \mu\text{m}^2\text{s}^{-\alpha}$  (s.e.m  $\sim 1.5 \times 10^{-3} \mu\text{m}^2\text{s}^{-\alpha}$ ) for MDA-MB-231 cells,  $\sim 7.6 \times 10^{-3} \mu\text{m}^2\text{s}^{-\alpha}$  (s.e.m  $\sim 0.7 \times 10^{-3} \mu\text{m}^2\text{s}^{-\alpha}$ ) for MCF7 cells, and  $\sim 5.3 \times 10^{-3} \mu\text{m}^2\text{s}^{-\alpha}$  (s.e.m  $\sim 0.7 \times 10^{-3} \mu\text{m}^2\text{s}^{-\alpha}$ ) for MCF10A cells. There is no significant difference ( $P > 0.05$ ) in  $D_{\text{app},i}$  between the different cancer cell lines as shown in Fig. 3.5D. On the other hand,  $\alpha_i$  is dependent on the cell's intrinsic activity as shown in Fig. 3.5E. Both  $\alpha_1$  ( $\alpha$  when  $0 < \Delta t$  (s)  $< 1$ ) and  $\alpha_2$  ( $\alpha$  when  $1 < \Delta t$  (s)  $< 10$ ) is the highest for MDA-MB-231 cells, followed by MCF7 cells and MCF10A cells respectively. The ensemble average  $\langle \alpha_1 \rangle$  is 0.49 (s.e.m.  $\sim 0.03$ ) for MDA-MB-231 cells, 0.36 (s.e.m.  $\sim 0.01$ ) for MCF7 cells and 0.33 (s.e.m.  $\sim 0.03$ ) for MCF10A cells. The ensemble average  $\langle \alpha_2 \rangle$  is 0.88 (s.e.m.  $\sim 0.04$ ) for MDA-MB-231 cells, 0.7 (s.e.m.  $\sim 0.02$ ) for MCF7 cells and 0.67 (s.e.m.  $\sim 0.04$ ) for MCF10A cells. These observations provide direct evidence that intracellular DNA cargo trajectories are less subdiffusive in metastatic cell cytoplasm followed by malignant and benign cells, respectively. The DNA cargo from all the cell lines experience a short time scale caging (before  $\Delta t \sim 1$  s) followed by escape from the cage ( $\Delta t \sim 1$  s). The percentage of trajectories which follow caged, subdiffusive and superdiffusive transport are plotted in Fig. 3.15 (appendix). Before  $\Delta t \sim 1$  s,  $\sim 50\%$  of the DNA cargo trajectories are caged,  $\sim 40\%$  are subdiffusive and  $\sim 10\%$  are superdiffusive for MDA-MB-231 cells. After  $\Delta t \sim 1$  s,  $\sim 15\%$  of the DNA cargo trajectories are caged,  $\sim 35\%$  are subdiffusive and  $\sim 50\%$  are superdiffusive for MDA-MB-231 cells. Similarly for MCF7 and MCF10A cells,  $\sim 60\%$  of DNA cargo trajectories are caged,  $\sim 35\%$  are sub-

diffusive and  $\sim 5\%$  are superdiffusive before  $\Delta t \sim 1$  s. For MCF7 cells,  $\sim 20\%$  of the DNA cargo trajectories are caged,  $\sim 55\%$  are subdiffusive and  $\sim 25\%$  are superdiffusive after  $\Delta t \sim 1$  s. For MCF10A cells,  $\sim 30\%$  of the DNA cargo trajectories are caged,  $\sim 50\%$  are subdiffusive and  $\sim 20\%$  are superdiffusive after  $\Delta t \sim 1$  s. Hence, the percentage of the DNA cargo trajectories that display superdiffusive behavior is strongly correlated to the cancer state of the cell.

What leads to the differences in the anomalous diffusion between metastatic cells, malignant and benign cells? Metastatic cells have a higher degree of intracellular activity followed by malignant cells and benign cells [14, 46]. Since the size of the DNA cargo is the same (as demonstrated by lack of significant differences in  $D_{\text{app}}$  of 500 bp DNA cargo in different cell lines), the observed behavior is strongly correlated to the forces exerted by the molecular motors [19]. Although the cytoplasm remains viscoelastic (as demonstrated by the velocity autocorrelation function) for the DNA cargo for all the cancer cells tested, the values of  $\alpha_1$  suggest that the intracellular fluctuations are significantly higher in metastatic cells compared to malignant and benign cells. This leads to the lower degree of caging observed in metastatic cells followed by malignant and benign cells. The long time scale behavior (after  $\Delta t \sim 1$  s) suggests that the forces exerted by the molecular motors on the DNA cargo is higher in the metastatic cells followed by malignant cells and benign cells and leads to a higher fraction of DNA cargo trajectories displaying superdiffusive behavior. The ergodicity breaking of the DNA cargo motion supports the molecular motor's involvement in the intracellular DNA cargo trajectories. Our results show that the intracellular DNA cargo trajectories in cancerous and non-cancerous cell lines can be described by coexisting ergodic and non-ergodic anomalous diffusion. The intracellular mobility differences across various cell types for a fixed size DNA cargo arise from the cell's intracellular activity. Overall, our results strongly suggest that the transport of DNA cargo is governed by active stresses in the cell cytoplasm (which depends on the cell's cancer state) and viscous drag in the cytoplasm (which depends on the DNA size).

### 3.4. CONCLUSIONS

We demonstrate that the electrotransferred DNA cargo undergoes coexisting ergodic and non-ergodic anomalous diffusion for different DNA sizes (100 bp, 250 bp, 500 bp) and non-cancerous and cancerous cell lines (CHO-K1, MCF10A, MCF7, and MDA-MB-231). The DNA cargo trajectories can be described by anomalous diffusion consisting of two characteristic scalings with lag time with a crossover lag time  $\sim 1$  s. The apparent diffusion coefficient of the DNA cargo in CHO cell cytoplasm decreased when we increased the DNA size from 100 bp to 500 bp. At short lagtimes, most of the DNA cargo trajectories are caged and subdiffusive, while at long lag times, the DNA cargo trajectories are caged, subdiffusive, or superdiffusive. The fraction of DNA cargo trajectories displaying caged, subdiffusive, or superdiffusive behavior has no visible correlation with the DNA size in CHO cell cytoplasm but strongly correlates with the cell's cancer state. 500 bp DNA cargo in metastatic cytoplasm experience a higher percentage of superdiffusive transport and lowest degree of caging in comparison to malignant cells and benign cancer cell cytoplasm. Hence the viscous drag and active cytoplasmic forces are important factors in electrotransferred DNA cargo's intracellular motion. Our findings provide guidelines to

develop new theoretical models to rationally design and optimize DNA electrotransfer protocols for different DNA sizes and cell types.

### AUTHOR CONTRIBUTIONS

A.M. and P.E.B designed the research; A.M. performed the research with contributions from H.U.; A. M. analyzed the data; A. M. wrote the chapter with contributions from P.E.B.

## 3

### CHAPTER COVER

A confocal microscopy image of CHO cells with internalized Cy3 labelled DNA (in red) and Coumarin labelled polymer (in blue).

## APPENDIX

## 3.A. INTRACELLULAR TRANSPORT OF DIFFERENT SIZED DNA CARGO IN CHO-K1 CELLS

## 3.A.1. SAMPLE TRAJECTORIES

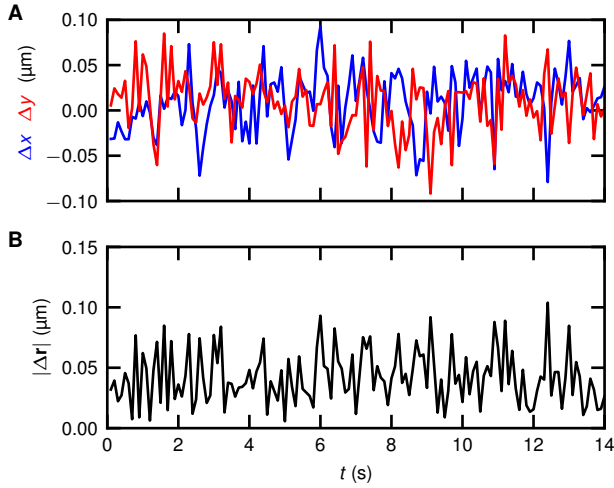


Figure 3.6: Representative intracellular DNA cargo displacements in CHO cells. (A) Representative  $x$  (blue) and  $y$  displacements (time interval of 0.1 s) during a measurement. (B) Corresponding magnitude of the two dimensional displacement defined as  $\Delta \mathbf{r} = |\sqrt{\Delta x^2 + \Delta y^2}|$ .

An example of representative intracellular DNA cargo displacement in CHO cells is plotted in Fig. 3.6. The one dimensional displacements is shown in Fig. 3.6A and the Fig. 3.6B shows the magnitude of the two dimensional displacement defined as  $\Delta \mathbf{r} = |\sqrt{\Delta x^2 + \Delta y^2}|$  during a time interval of 0.1 s. We see no evidence of stalling events (zero displacement) that would be seen in a CTRW.

### 3.A.2. ERGODICITY BREAKING

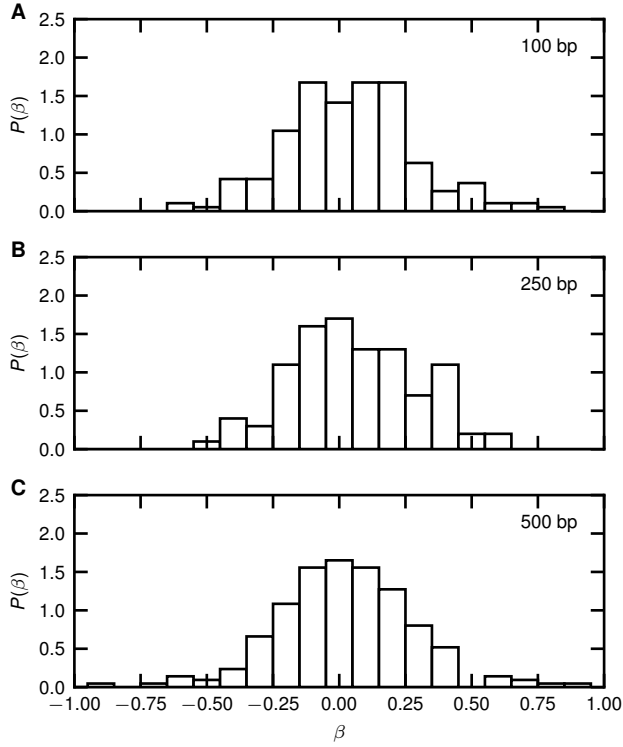


Figure 3.7: Probability density distributions of power law exponent  $\beta$  obtained by fitting  $\overline{\Delta r^2(\Delta t, T)} \propto T^\beta$  is plotted for (A) 100 bp, (B) 250 bp, (C) 500 bp DNA. The fitting is performed between measurement time  $T = 0.8$  s and 10 s to avoid errors due to poor statistics at short time scales.

The dependence of the time averaged mean square displacement  $\overline{\Delta r^2(\Delta t, T)}$  with measurement time  $T$  is then tested.  $\overline{\Delta r^2(\Delta t, T)}$  was evaluated for different values of  $T$  and was plotted in Figs. 4A-C for different DNA sizes. We extract the power law dependence of  $\overline{\Delta r^2(\Delta t, T)}$  with  $T$  by fitting data with the equation  $\overline{\Delta r^2(\Delta t, T)} = AT^\beta$ , where  $\beta$  is the power law exponent and  $A$  is a dummy variable. The fitting is performed between  $T = 0.8$  s and 10 s to avoid noise at the short time scales due to poor statistics. While the peak of probability density distributions plotted in Fig. 3.7 is at  $\overline{\Delta r^2(\Delta t, T)} \sim T^0$ , non zero power law exponents are present.

### 3.A.3. DIRECTIONAL CHANGE DISTRIBUTION

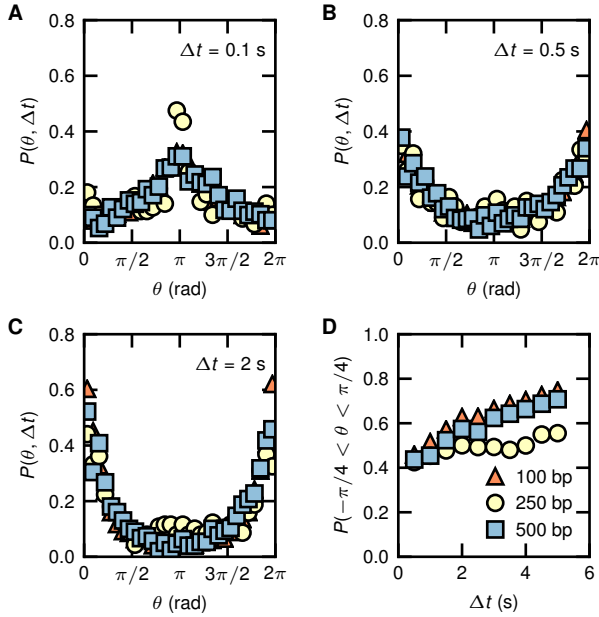


Figure 3.8: Directional change distribution for 100 bp, 250 bp and 500 bp DNA for different degrees of temporal coarsening (A)  $\Delta t = 0.1$  s, (B)  $\Delta t = 0.5$  s, and (C)  $\Delta t = 2$  s. (D) Probability of increase in directionality ( $-\pi/4 < \theta < \pi/4$ ) for different DNA sizes is plotted as a function of increasing temporal coarsening  $\Delta t$ .

We plot the directional change probability density distribution between steps for the different sizes of DNA in Figs. 3.8A-C. The relative angle  $\theta(t, \Delta t)$  is defined as

$$\cos\theta(t, \Delta t) = \frac{\Delta\mathbf{r}(t) \cdot \Delta\mathbf{r}(t + \Delta t)}{|\Delta\mathbf{r}(t)| |\Delta\mathbf{r}(t + \Delta t)|}, \quad (3.6)$$

where the lag time  $\Delta t$  represents the temporal coarsening [36]. At short lag times ( $\Delta t = 0.1$  s), the directional change has a peak centered around  $\pi$  rad indicating that the DNA is trapped within a confining potential [39]. This is expected as the DNA is trapped in the viscoelastic cytoskeletal meshwork. At further temporal coarsening ( $\Delta t = 0.5$  s and  $\Delta t = 1$  s), the peak shifts towards 0 rad and  $2\pi$  rad showing the presence of directional inertial motion as shown in Figs. 3.8B-C. The development of the directionality is then quantified by plotting  $P(-\pi/4 < \theta < \pi/4)$  as a function of temporal coarsening in Fig. 3.8D. We see that for all the DNA fragment sizes, directionality of the trajectories increases with increasing temporal coarsening.

## 3.A.4. APPARENT DIFFUSION COEFFICIENT AND ANOMALOUS EXPONENT

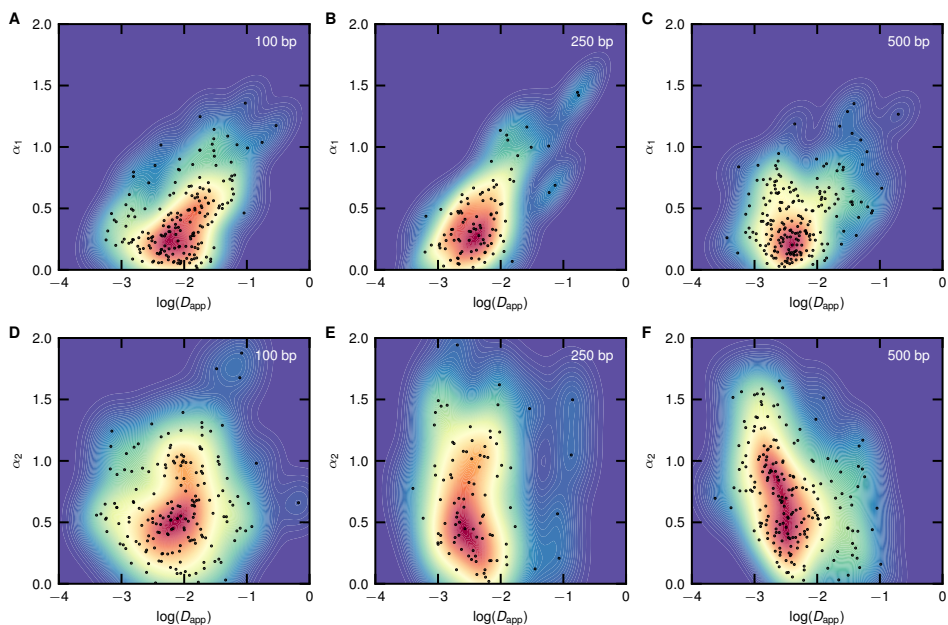


Figure 3.9: Scatter plot of logarithm of the apparent diffusion coefficient ( $D_{app}$ ) and anomalous exponent ( $\alpha$ ) obtained at short lag time (A)-C) and long lag time (D)-F) for (A), (D) 100 bp, (B), (E) 250 bp, and (C), (F) 500 bp DNA. The probability density is plotted as a contour with red indicating high density and blue indicating low density.

The two dimensional probability density of logarithm of the apparent diffusion coefficient ( $D_{app}$ ) and anomalous exponent ( $\alpha$ ) obtained from individual trajectories are plotted in Fig. 3.9. The data is plotted separately for short lag times in Fig. 3.9A-C and long lag times in Fig. 3.9D-F.

### 3.A.5. CLASSIFICATION OF TRAJECTORIES

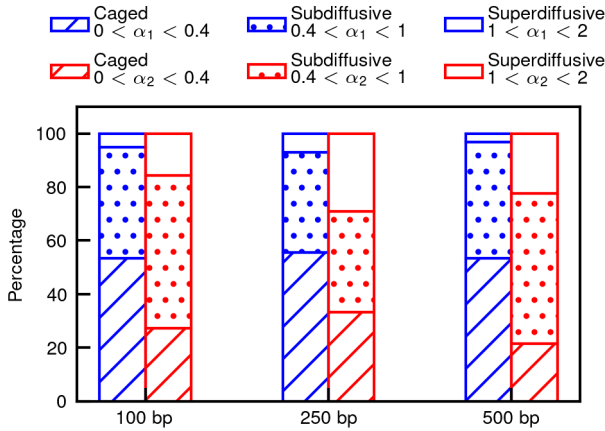


Figure 3.10: Classification of individual trajectories to caged ( $\alpha \leq 0.4$ ), subdiffusive ( $0.4 < \alpha \leq 1$ ), and superdiffusive ( $\alpha > 1$ ) for short lag times (blue) and long times (red) for different DNA sizes.

We classify the trajectories as caged ( $\alpha \leq 0.4$ ), subdiffusive ( $0.4 < \alpha \leq 1$ ), and superdiffusive ( $\alpha > 1$ ) based on value of the anomalous exponent. Fig. 3.10 shows that  $\sim 60\%$  of the trajectories remain caged for all DNA sizes at short lag times. Approximately  $35\%$  of the trajectories are subdiffusive and rest superdiffusive at short lag times. At longer lag times,  $\sim 20\%$  trajectories remain caged,  $\sim 60\%$  trajectories subdiffusive and rest superdiffusive.



### 3.A.6. VELOCITY AUTOCORRELATION

We evaluate  $C_v^\delta(\Delta t) = \overline{\mathbf{v}(t + \Delta t) \cdot \mathbf{v}(t)}$  with different values of  $\delta$  to identify if the negative correlation arises from localization errors, confinement or medium elasticity[47]. The  $C_v^\delta(\Delta t) = \overline{\mathbf{v}(t + \Delta t) \cdot \mathbf{v}(t)}$  for 100 bp DNA cargo with  $\delta = 0.1, 0.2, 0.5$  s is plotted in Fig. 3.11. We observe that the  $C_v^\delta(\Delta t) = \overline{\mathbf{v}(t + \Delta t) \cdot \mathbf{v}(t)}$  is self similar and collapses to a single curve for different values of  $\delta$ . This shows the observed negative correlation does not come from the localization errors but ergodic FBM.

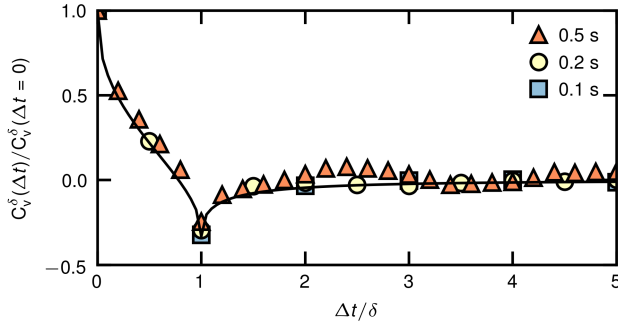


Figure 3.11: Velocity auto-correlation function  $C_v^\delta(\Delta t) = \overline{\mathbf{v}(t + \Delta t) \cdot \mathbf{v}(t)}$ , where  $\mathbf{v}(t) = [\mathbf{r}(t + \delta) - \mathbf{r}(t)] / \delta$  normalized by  $C_v^\delta(\Delta t = 0)$  plotted against the lag time  $\Delta t$  normalized by the discretization time interval  $\delta = 0.1, 0.2, 0.5$  s for 100 bp DNA cargo in CHO-K1 cell cytoplasm. The solid line is the analytical prediction from fractional Brownian motion (FBM)

### 3.B. INTRACELLULAR TRANSPORT OF 500 BP DNA CARGO IN DIFFERENT CANCER CELLS

#### 3.B.1. NON ERGODICITY OF 500 BP DNA CARGO IN DIFFERENT CANCER CELLS

The heterogeneity in  $\overline{\Delta r^2(\Delta t, T)}$  for  $T = 10$  s is presented in Fig. 3.12A-C for MDA-MB-231, MCF7 and MCF10A cells. To understand the origin of observed heterogeneity, we checked for ergodicity breaking. We observe that  $\overline{\Delta r^2(\Delta t, T)}$  as presented by its power law dependence with  $T$  in Fig. 3.13A-C.

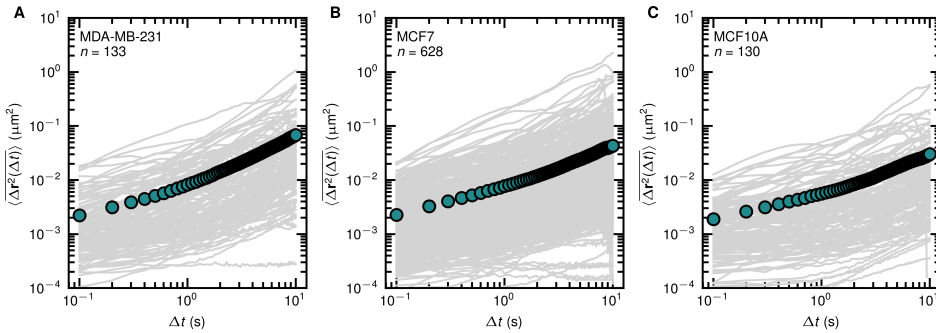


Figure 3.12: Individual time averaged mean square displacements ( $\overline{\Delta r^2(\Delta t, T)}$ ) of 500 bp DNA cargo in cytoplasm are plotted in solid gray color for (A) MDA-MB-231 (B) MCF7 (C) MCF10A cells against the lag time  $\Delta t$ , for a measurement time  $T = 10$  s. The green circles represent the ensemble and time average mean square displacement ( $\langle \overline{\Delta r^2(\Delta t, T)} \rangle$ ).

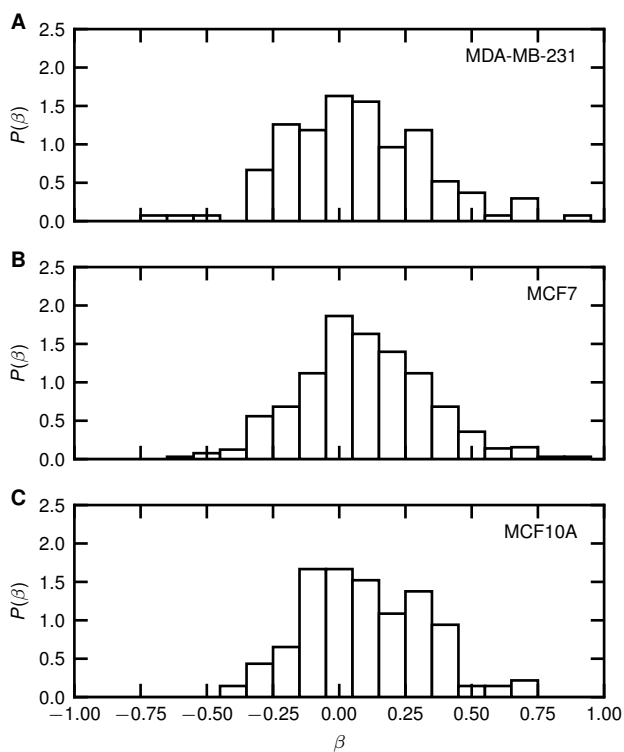


Figure 3.13: Probability density distributions of power law exponent  $\beta$  obtained by fitting  $\overline{\Delta r^2}(\Delta t, T) \propto T^\beta$  of 500 bp DNA cargo in the cytoplasm is plotted for (A) MDA-MB-231, (B) MCF7, (C) MCF10A cells. The fitting is performed between measurement time  $T = 0.8$  s and 10 s to avoid errors due to poor statistics at short time scales.

### 3.B.2. APPARENT DIFFUSION COEFFICIENT AND ANOMALOUS EXPONENT

The two dimensional probability density of logarithm of the apparent diffusion coefficient ( $D_{\text{app}}$ ) and anomalous exponent ( $\alpha$ ) obtained from individual trajectories for different cancer cells are plotted in Fig. 3.14. The data is plotted separately for short lag times in Fig. 3.14A-C and long lag times in Fig. 3.14D-F.

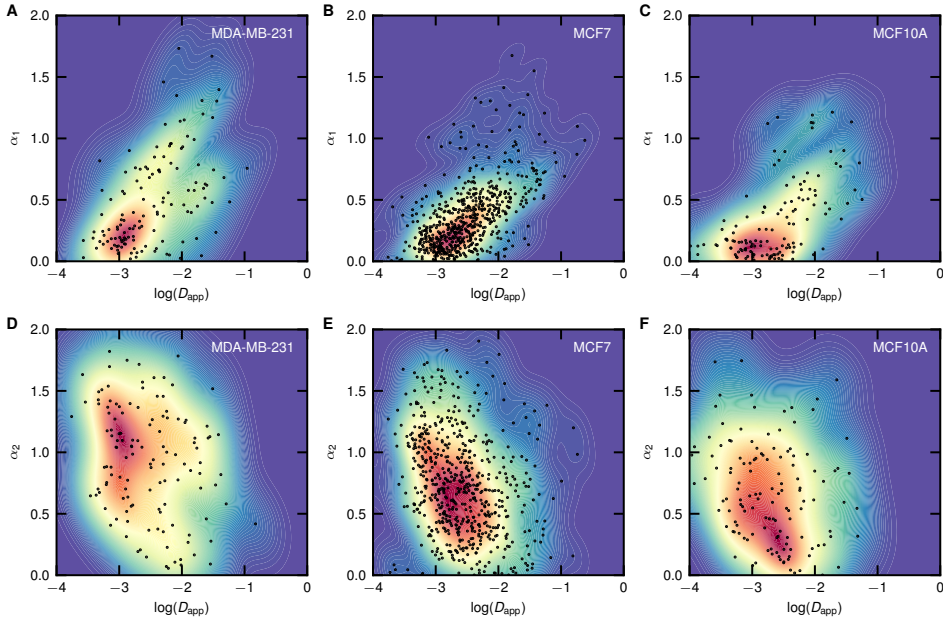


Figure 3.14: Scatter plot of logarithm of the apparent diffusion coefficient ( $D_{\text{app}}$ ) and anomalous exponent ( $\alpha$ ) obtained at short lag time (A)-(C) and long lag time (D)-(F) for (A), (D) MDA-MB-231, (B), (E) MCF7 bp, and (C), (F) MCF10A cells. The probability density is plotted as a contour with red indicating high density and blue indicating low density.

### 3.B.3. CLASSIFICATION OF TRAJECTORIES

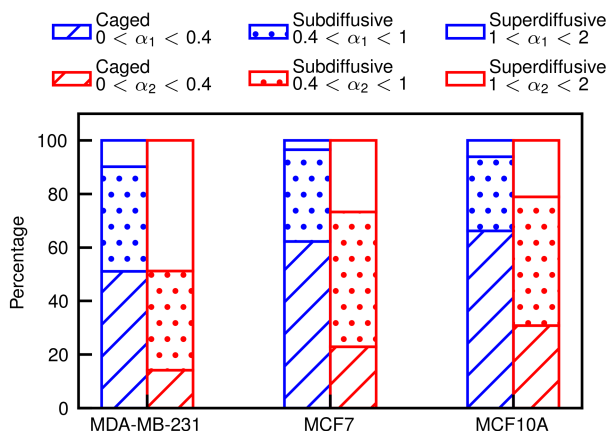


Figure 3.15: Classification of individual trajectories to caged ( $\alpha \leq 0.4$ ), subdiffusive ( $0.4 < \alpha \leq 1$ ), and superdiffusive ( $\alpha > 1$ ) for short lag times (blue) and long times (red) for different cancer cells.

We classify the the trajectories as caged ( $\alpha \leq 0.4$ ), subdiffusive ( $0.4 < \alpha \leq 1$ ), and superdiffusive ( $\alpha > 1$ ) based on value of the anomalous exponent. Fig. 3.15 shows that  $\sim 60\%$  of the 500 bp DNA cargo trajectories for MCF7 and MCF10A cells, and  $\sim 50\%$  of the trajectories and MDA-MB-231 cells remain caged at short lag times. Approximately 35% of the trajectories are subdiffusive and rest superdiffusive at short lag times. At longer lag times,  $\sim 30\%$  trajectories in MCF10A,  $\sim 20\%$  trajectories in MCF7, and  $\sim 15\%$  trajectories for MDA-MB-231 cells remain caged.  $\sim 50\%$  of the 500 bp DNA cargo trajectories in MCF10A and MCF7 and  $\sim 35\%$  in MDA-MB-231 cells are subdiffusive and rest superdiffusive.

### 3.B.4. DIRECTIONAL CHANGE DISTRIBUTION

We plot the directional change distribution for 500 bp DNA cargo for MCF10A, MCF7 and MDA-MB-231 cells at different degree temporal coarsening in Fig. 3.16A-C. We observe similar behavior in all cell lines that at probability of directionality increases with the increasing temporal coarsening.

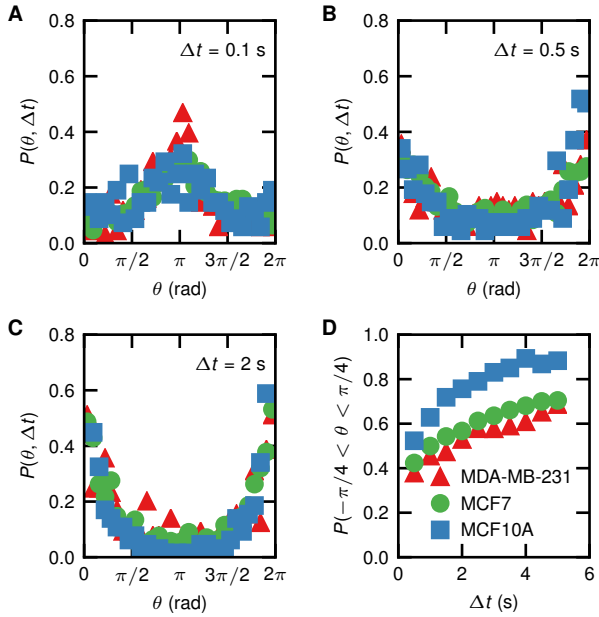


Figure 3.16: Directional change distribution of 500 bp DNA cargo in the cytoplasm of MDA-MB-231, MCF7 and MCF10A cells for different degrees of temporal coarsening (A)  $\Delta t = 0.1$  s, (B)  $\Delta t = 0.5$  s, and (C)  $\Delta t = 2$  s. (D) Probability of increase in directionality ( $P(-\pi/4 < \theta < \pi/4)$ ) for different DNA sizes is plotted as a function of increasing temporal coarsening  $\Delta t$ .

## REFERENCES

- [1] A. Muralidharan, H. Uitenbroek, and P. E. Boukany, *Intracellular transport of electrotransferred DNA cargo is governed by coexisting ergodic and non ergodic anomalous diffusion*, bioRxiv (2021).
- [2] D. W. Pack, A. S. Hoffman, S. Pun, and P. S. Stayton, *Design and development of polymers for gene delivery*, Nature Reviews Drug discovery **4**, 581 (2005).
- [3] G. Sahay, D. Y. Alakhova, and A. V. Kabanov, *Endocytosis of nanomedicines*, Journal of Controlled Release **145**, 182 (2010).
- [4] C. Rosazza, S. Haberl Meglic, A. Zumbusch, M.-P. Rols, and D. Miklavcic, *Gene electrotransfer: a mechanistic perspective*, Current Gene Therapy **16**, 98 (2016).
- [5] M. P. Stewart, R. Langer, and K. F. Jensen, *Intracellular delivery by membrane disruption: mechanisms, strategies, and concepts*, Chemical Reviews **118**, 7409 (2018).
- [6] A. Paganin-Gioanni, E. Bellard, J.-M. Escoffre, M.-P. Rols, J. Teissié, and M. Golzio, *Direct visualization at the single-cell level of siRNA electrotransfer into cancer cells*, Proceedings of the National Academy of Sciences **108**, 10443 (2011).
- [7] S. Sachdev, S. F. Moreira, Y. Keehnen, L. Rems, M. T. Kreutzer, and P. E. Boukany, *DNA-membrane complex formation during electroporation is DNA size-dependent*, Biochimica et Biophysica Acta (BBA)-Biomembranes **1862**, 183089 (2020).
- [8] M. Golzio, J. Teissié, and M.-P. Rols, *Direct visualization at the single-cell level of electrically mediated gene delivery*, Proceedings of the National Academy of Sciences **99**, 1292 (2002).
- [9] C. Rosazza, A. Buntz, T. Rieß, D. Wöll, A. Zumbusch, and M.-P. Rols, *Intracellular tracking of single-plasmid DNA particles after delivery by electroporation*, Molecular Therapy **21**, 2217 (2013).
- [10] C. Rosazza, H. Deschout, A. Buntz, K. Braeckmans, M.-P. Rols, and A. Zumbusch, *Endocytosis and endosomal trafficking of DNA after gene electrotransfer in vitro*, Molecular Therapy-Nucleic Acids **5**, e286 (2016).
- [11] C.-C. Chang, M. Wu, and F. Yuan, *Role of specific endocytic pathways in electrotransfection of cells*, Molecular Therapy-Methods & Clinical Development **1**, 14058 (2014).
- [12] L. Wang, S. E. Miller, and F. Yuan, *Ultrastructural analysis of vesicular transport in electrotransfection*, Microscopy and Microanalysis **24**, 553 (2018).
- [13] A. Caspi, R. Granek, and M. Elbaum, *Enhanced diffusion in active intracellular transport*, Physical Review Letters **85**, 5655 (2000).
- [14] M. Guo, A. J. Ehrlicher, M. H. Jensen, M. Renz, J. R. Moore, R. D. Goldman, J. Lippincott-Schwartz, F. C. Mackintosh, and D. A. Weitz, *Probing the stochastic, motor-driven properties of the cytoplasm using force spectrum microscopy*, Cell **158**, 822 (2014).

- [15] N. Fakhri, A. D. Wessel, C. Willms, M. Pasquali, D. R. Klopfenstein, F. C. MacKintosh, and C. F. Schmidt, *High-resolution mapping of intracellular fluctuations using carbon nanotubes*, *Science* **344**, 1031 (2014).
- [16] J. Suh, D. Wirtz, and J. Hanes, *Efficient active transport of gene nanocarriers to the cell nucleus*, *Proceedings of the National Academy of Sciences* **100**, 3878 (2003).
- [17] F. Etoc, E. Balloul, C. Vicario, D. Normanno, D. Liße, A. Sittner, J. Piehler, M. Dahan, and M. Coppey, *Non-specific interactions govern cytosolic diffusion of nanosized objects in mammalian cells*, *Nature Materials* **17**, 740 (2018).
- [18] B. Wang, J. Kuo, and S. Granick, *Bursts of active transport in living cells*, *Physical Review Letters* **111**, 208102 (2013).
- [19] K. Chen, B. Wang, and S. Granick, *Memoryless self-reinforcing directionality in endosomal active transport within living cells*, *Nature Materials* **14**, 589 (2015).
- [20] S. A. Tabei, S. Burov, H. Y. Kim, A. Kuznetsov, T. Huynh, J. Jureller, L. H. Philipson, A. R. Dinner, and N. F. Scherer, *Intracellular transport of insulin granules is a subordinated random walk*, *Proceedings of the National Academy of Sciences* **110**, 4911 (2013).
- [21] H. C. Berg, *Random walks in biology*, 1st ed. (Princeton University Press, 41 William Street, Princeton, New Jersey 08540, 1993).
- [22] C. P. Brangwynne, G. H. Koenderink, F. C. MacKintosh, and D. A. Weitz, *Intracellular transport by active diffusion*, *Trends in Cell Biology* **19**, 423 (2009).
- [23] K. Norregaard, R. Metzler, C. M. Ritter, K. Berg-Sørensen, and L. B. Oddershede, *Manipulation and motion of organelles and single molecules in living cells*, *Chemical Reviews* **117**, 4342 (2017).
- [24] M. J. Saxton, *Anomalous diffusion due to obstacles: a Monte Carlo study*, *Biophysical Journal* **66**, 394 (1994).
- [25] M. J. Saxton, *Anomalous diffusion due to binding: a Monte Carlo study*, *Biophysical Journal* **70**, 1250 (1996).
- [26] A. Sabri, X. Xu, D. Krapf, and M. Weiss, *Elucidating the origin of heterogeneous anomalous diffusion in the cytoplasm of mammalian cells*, *Physical Review Letters* **125**, 058101 (2020).
- [27] R. Metzler, J.-H. Jeon, A. G. Cherstvy, and E. Barkai, *Anomalous diffusion models and their properties: non-stationarity, non-ergodicity, and ageing at the centenary of single particle tracking*, *Physical Chemistry Chemical Physics* **16**, 24128 (2014).
- [28] S. C. Weber, A. J. Spakowitz, and J. A. Theriot, *Bacterial chromosomal loci move subdiffusively through a viscoelastic cytoplasm*, *Physical Review Letters* **104**, 238102 (2010).



- [29] T. J. Lampo, S. Stylianidou, M. P. Backlund, P. A. Wiggins, and A. J. Spakowitz, *Cytoplasmic RNA-protein particles exhibit non-Gaussian subdiffusive behavior*, *Bio-physical Journal* **112**, 532 (2017).
- [30] C. Manzo, J. A. Torreno-Pina, P. Massignan, G. J. Lapeyre Jr, M. Lewenstein, and M. F. G. Parajo, *Weak ergodicity breaking of receptor motion in living cells stemming from random diffusivity*, *Physical Review X* **5**, 011021 (2015).
- [31] D. Allan, C. van der Wel, N. Keim, T. Caswell, D. Wieker, R. Verweij, C. Reid, L. Grueter, K. Ramos, R. Perry, *et al.*, *soft-matter/trackpy: Trackpy v0. 4.2*, (2019).
- [32] M. Doi, *Soft Matter Physics* (Oxford University Press, 2013).
- [33] F. C. MacKintosh and P. A. Janmey, *Actin gels*, *Current Opinion in Solid State and Materials Science* **2**, 350 (1997).
- [34] J. Perrin, *Mouvement Brownien et réalité moléculaire*, *Annales de Chimie et de Physique* **18**, 5 (1909).
- [35] A. Einstein, *Über die von der molekularkinetischen theorie der wärme geforderte bewegung von in ruhenden flüssigkeiten suspendierten teilchen*, *Annalen der Physik* **4** (1905).
- [36] S. Burov, S. A. Tabei, T. Huynh, M. P. Murrell, L. H. Philipson, S. A. Rice, M. L. Gardel, N. F. Scherer, and A. R. Dinner, *Distribution of directional change as a signature of complex dynamics*, *Proceedings of the National Academy of Sciences* **110**, 19689 (2013).
- [37] J.-H. Jeon, M. Javanainen, H. Martinez-Seara, R. Metzler, and I. Vattulainen, *Protein crowding in lipid bilayers gives rise to non-Gaussian anomalous lateral diffusion of phospholipids and proteins*, *Physical Review X* **6**, 021006 (2016).
- [38] Y. He, S. Burov, R. Metzler, and E. Barkai, *Random time-scale invariant diffusion and transport coefficients*, *Physical Review Letters* **101**, 058101 (2008).
- [39] S. Burov, J.-H. Jeon, R. Metzler, and E. Barkai, *Single particle tracking in systems showing anomalous diffusion: the role of weak ergodicity breaking*, *Physical Chemistry Chemical Physics* **13**, 1800 (2011).
- [40] B. B. Mandelbrot and J. W. Van Ness, *Fractional Brownian motions, fractional noises and applications*, *SIAM Review* **10**, 422 (1968).
- [41] A. V. Weigel, B. Simon, M. M. Tamkun, and D. Krapf, *Ergodic and nonergodic processes coexist in the plasma membrane as observed by single-molecule tracking*, *Proceedings of the National Academy of Sciences* **108**, 6438 (2011).
- [42] M. Di Pierro, D. A. Potoyan, P. G. Wolynes, and J. N. Onuchic, *Anomalous diffusion, spatial coherence, and viscoelasticity from the energy landscape of human chromosomes*, *Proceedings of the National Academy of Sciences* **115**, 7753 (2018).

- [43] J. S. Lucas, Y. Zhang, O. K. Dudko, and C. Murre, *3D trajectories adopted by coding and regulatory DNA elements: first-passage times for genomic interactions*, *Cell* **158**, 339 (2014).
- [44] Y. Meroz and I. M. Sokolov, *A toolbox for determining subdiffusive mechanisms*, *Physics Reports* **573**, 1 (2015).
- [45] A. Muralidharan, L. Rems, M. T. Kreutzer, and P. E. Boukany, *Actin networks regulate the cell membrane permeability during electroporation*, *Biochimica et Biophysica Acta (BBA)-Biomembranes* **1863**, 183468 (2021).
- [46] Y.-L. Liu, C.-K. Chou, M. Kim, R. Vasisht, Y.-A. Kuo, P. Ang, C. Liu, E. P. Perillo, Y.-A. Chen, K. Blocher, *et al.*, *Assessing metastatic potential of breast cancer cells based on EGFR dynamics*, *Scientific Reports* **9**, 1 (2019).
- [47] S. C. Weber, M. A. Thompson, W. E. Moerner, A. J. Spakowitz, and J. A. Theriot, *Analytical tools to distinguish the effects of localization error, confinement, and medium elasticity on the velocity autocorrelation function*, *Biophysical Journal* **102**, 2443 (2012).



The image features a dark blue background with a repeating pattern of small, light blue, irregularly shaped micro-traps. The traps are arranged in a grid-like fashion, with some overlapping. The text "Micro-trap electroporation" is centered in the image in a white, serif font.

*Micro-trap  
electroporation*

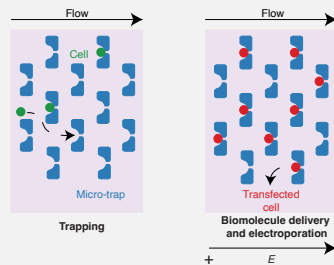


# 4

## MICRO-TRAP ARRAY ON A CHIP FOR LOCALIZED ELECTROPORATION AND ELECTRO-GENE TRANSFECTION

### Highlights

- A localized electroporation device based on microtrap technology was developed.
- Cells are positioned in regions of high electric field by flow.
- Successful delivery of small molecules and plasmid DNA achieved.
- Maintains high cell viability and achieves high electroporation efficiency.



We developed a localized single-cell electroporation chip to deliver exogenous biomolecules with high efficiency while maintaining high cell viability. In our microfluidics device, the

This chapter is published as A. Muralidharan, G. Pesch, H. Hubbe, L. Rems, M. Nouri-Goushki, and P. E. Boukany, *Bioelectrochemistry* (2022) [1].

*cells are trapped in a microtrap array by flow, after which target molecules are supplied to the device and electrotransferred to the cells under electric pulses. The system provides the ability to monitor the electrotransfer of exogenous biomolecules in real-time. We reveal through numerical simulations that localized electroporation is the mechanism of permeabilization in the microtrap array electroporation device. We demonstrate the simplicity and accuracy of this microtrap technology for electroporation by delivery of both small molecule electrotransfer using propidium iodide and large molecule electrotransfer using plasmid DNA for gene expression, illustrating the potential of this minimally invasive method to be widely used for precise intracellular delivery purposes (from bioprocess engineering to therapeutic applications).*

## 4.1. INTRODUCTION

4

Precise intracellular biomolecule delivery in a safe, affordable, and robust way is key to fundamental cell biology research and biomedical applications. Transient permeabilization of cell membranes using pulsed electric fields (electroporation) is a simple non-viral method to deliver exogenous biomolecules to a variety of cell types [2–7]. However, conventional electroporation often suffers from poor efficiency as it relies on bulk stochastic phenomena and poor control over the cell viability due to the strong electric fields used during electroporation [8, 9].

To obtain non-toxic electroporation with controlled biomolecule delivery, it is required to apply electric pulses through miniaturized (small) geometries, which induce localized electroporation at the cell membrane [10–13]. In localized electroporation, the applied electric field is concentrated by utilizing miniaturized structures such as micro/nanochannels [10, 14–24], porous membranes [11, 25], nanostraws [26–28], nanotubes [29], nanopores [30–32], or microneedles [33–35]. This can provide precise control over the dosage of the delivered exogenous cargoes [10, 11]. Localized electroporation is compatible with delivering a variety of exogenous cargo such as molecular beacons [10, 36], lipoplex nanoparticles [37], siRNA [38], mRNA [11], plasmid DNA [10, 11, 23, 25], and Cas9 ribonuclear proteins [11] while maintaining high cell viability. However, the cells should either be adhered to the structures (or substrate) [11, 23, 27] or be micro-manipulated to the structure through an external force (e.g., by optical and magnetic tweezers or a micromanipulator) [10, 32] for successful localized electroporation.

To overcome this limitation, we fabricated a scalable hydrodynamic microtrap array integrated into a microfluidic channel [39, 40] (or microtraps for brevity) to simultaneously immobilize cells at miniaturized constrictions and perform localized electroporation. The cells are trapped in the microtraps through flow and are tightly attached to the trap's aperture, where the applied voltage drop in the channel is concentrated. Our device enables us to electroporate the single trapped cells while maintaining high cell viability (> 90%) and deliver small biomolecules and plasmid DNA encoding functional proteins. The cells can be continuously perfused with the culture media required for maintaining cell viability. We further confirm through numerical calculations that our device enables localized electroporation, with enhanced electroporation at the cell region facing the microtrap aperture and reduced electroporation in the remainder of the cell. Our microtrap electroporation device is a demonstration of a microfluidics approach, wherein single-cell trapping (under gentle flow conditions) and electrical pulses

control the precise delivery of cargoes into the cell. This microtrap localized electroporation device is anticipated to provide new opportunities for accurate and efficient drug delivery, ex vivo and gene editing application in cell biology and medicine.

## 4.2. MATERIALS AND METHODS

### 4.2.1. CELL CULTURE AND PREPARATION FOR MICROTRAP ELECTROPORATION

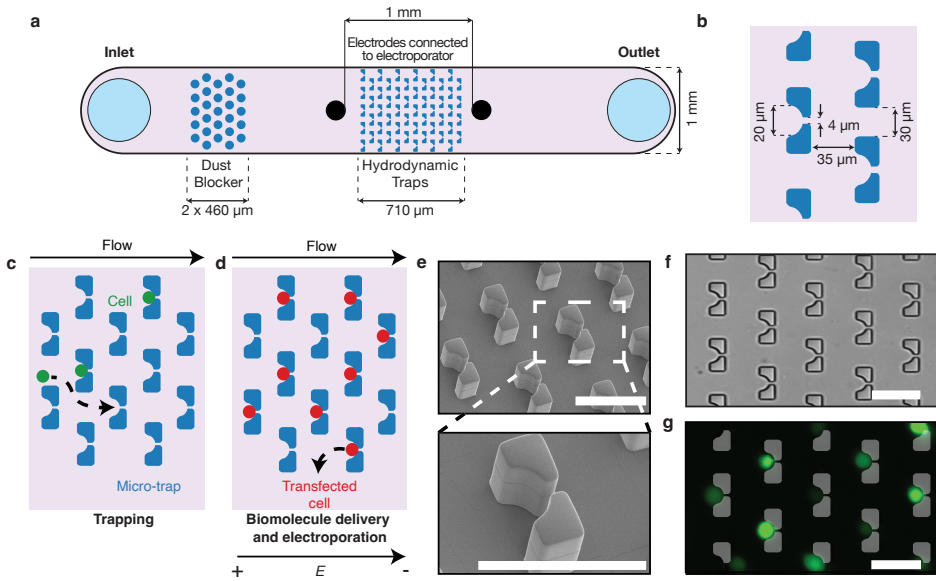


Figure 4.1: Microtrap array on a chip for localized electroporation working principle and design. (a) Schematic representation of the overall setup. Relevant dimensions are denoted in the figure. The fabricated PDMS device consists of a dust blocker to remove large debris near the inlet, an 710 μm long array of microtraps, and two electrodes separated by 1 mm. The device is 35 μm high. (b) The relevant dimensions of the microtraps are provided in this schematic. (c)-(d) Working principle of microtrap electroporation; (c) Stage 1: Hydrodynamic trapping of the cells in the microtraps by flowing cell suspension using a syringe pump, (d) stage 2: biomolecules are then delivered as a solution with a syringe pump and then delivered by application of electric fields. (e) Scanning electron microscopy images of the PDMS device (bottom is the zoomed in view of a single trap) containing the microtraps. (f) Brightfield image showing traps in the microfluidic device without the cells. (g) Calcein stained cells (stained for better clarity during visualization) have been trapped in the microtrap array. Scale bar is 50 μm.

The Chinese Hamster Ovary cells, CHO-K1 (DSMZ), are routinely cultured in T25 flasks containing 5 ml culture medium consisting of Nutrient Mixture Ham's F-12 (Sigma Aldrich) supplemented with ~ 10% Fetal Bovine Serum (Sigma Aldrich).

When the cells attain ~ 80 – 100% confluency, 1 μl of 5 mM Calcein AM or Calcein Red AM (both AAT Bioquest) is added to the T25 flasks to fluorescently label the cells for ease of visualization (final Calcein AM concentration ~ 1 μM). After incubating the cells with Calcein AM for 15-25 minutes in the incubator, cells are harvested by treating with trypsin-EDTA 0.25% (Sigma Aldrich). The cell-trypsin suspension is diluted with



5 ml Opti-MEM serum-free medium (Gibco) and then centrifuged. The supernatant is removed, and the cell pellet is suspended in 45 ml Opti-MEM serum-free medium to transfer to the microtrap electroporation device.

#### 4.2.2. PREPARATION OF FLUORESCENT MOLECULES AND PLASMIDS FOR ASSESSMENT OF ELECTROPORATION

Propidium iodide (PI), a membrane impermeant nucleic acid fluorescent stain, is used to assess the microtrap array electroporation efficacy. The stock solution of PI was diluted to 25  $\mu\text{M}$  in Opti-MEM before electroporation experiments. PI binds to nucleic acids and emits a strong fluorescence signal with an excitation/emission wavelength of 535/615 nm upon successful membrane permeabilization. We pre-stain the CHO cells with Calcein AM with an excitation/emission wavelength of 488/520 nm for PI delivery experiments. The pre-staining of CHO cells with Calcein AM provides a more precise visualization and tracking of the trapped cells inside the microfluidic chip.

To assess the microtrap array electro-gene transfection efficacy, pEGFP-C1 plasmid DNA is used. To prepare the plasmids for electro-gene transfection, DH5 $\alpha$  *E. coli* cultures are transformed with the pEGFP-C1 plasmids using heat shock. The plasmids are then extracted and purified using the GeneJET Plasmid Miniprep Kit. The DNA solution is diluted to 20  $\mu\text{g}/\text{ml}$  in Opti-MEM for microtrap electro-gene transfection experiments. Upon successful transfection, the pEGFP-C1 plasmids express a green fluorescent protein (GFP) with an excitation/emission wavelength of 488/507 nm. We pre-stain the cells with Calcein Red AM with an excitation/emission wavelength of 560/574 nm for the electro-gene transfection experiments.

#### 4.2.3. DEVICE FABRICATION AND EXPERIMENTAL SETUP

To perform microtrap localized electroporation, we designed a device with the following working principle. Single cells supplied to the device should be trapped in the microtraps until the streamlines through the trap aperture are closed, as displayed in Fig. 4.1(c). The applied electric field electroporates the cells trapped in the array. The field is locally amplified in the trap aperture caused by the insulating polydimethylsiloxane (PDMS) constriction. This enables localized electroporation and controlled transfer of cell membrane impermeant (bio-)molecules to cells, as displayed in Fig. 4.1(d).

The microchannels for microtrap array electroporation with the above requirements are fabricated from PDMS (Dow Sylgard 184) using standard soft lithography procedure [41]. The micro master mold is created in silicon using electron-beam lithography and novolac-based resist to pattern a plasma-enhanced chemical vapor deposition (PECVD) SiO<sub>2</sub> hard mask, followed by fluorine-based dry etching of the hard mask and Bosch process deep reactive-ion etching (DRIE) of the silicon to a depth of 35  $\mu\text{m}$ . The microfluidic patterns are transferred from the micro mold to a PDMS block and then cured overnight after mixing with Dow Sylgard 184 curing agent (PDMS to curing agent mixing ratio is 10:1) in the oven at 68 °C. The PDMS device consists of a dust blocker near the inlet and a microtrap array containing 203 traps, each with a trap aperture of 4  $\mu\text{m}$ . Four openings are punched into the PDMS block using biopsy punches for the device's inlet and outlet (diameter 1.5 mm) and two electrodes (diameter 0.5 mm). A glass slide spin-coated with a thin layer of PDMS is used to seal the microfluidic device after

treating both the top and bottom surfaces with air plasma (Harrick Plasma PDC-002). The assembled microfluidic device is then cured in the oven for 12 hours at 68 °C. The fabricated PDMS device and the structures are characterized after gold sputtering for 60 s (with JEOL JFC-1300 auto fine coater) on the PDMS device with a scanning electron microscope (JEOL JSM-2010LA) as shown in Fig. 4.1(e). Fig. 4.1(f) displays a section of the microtrap array (brightfield microscopy image) before trapping the cells. Fig. 4.1(g) shows an example of trapped calcein-stained CHO cells (shown in green).

#### 4.2.4. DELIVERY OF BIOMOLECULES USING MICROTRAP ARRAY ELECTROPORATION

To handle the samples (pre-stained cell suspension, pure Opti-MEM, and fluorescent molecules or plasmids), the required solutions are collected in 5 ml syringes. All the solutions are supplied using syringe pumps (Harvard Apparatus Pump 11 Elite). A 4-way IDEX valve connects the syringes to the microfluidic chip through polytetrafluoroethylene tubing (Kinesis, OD/ID 1.6 mm/0.8 mm). The 4 way connection to the valve is as follows: (i) input cell suspension or the target molecule solution, (ii) pure OptiMEM solution, (iii) inlet to the microtrap array device, (iv) waste. Two 0.5 mm platinum wires are used as electrodes and are connected before and after the microtrap array (spaced approximately 1 mm apart). The platinum wires are connected to a pulse generator (BETA tech Electrocell S20) to deliver the electric pulses. Once the required connections are inserted, the microtrap array device is flushed with pure Opti-MEM (flow rate = 50 ml/h or 833  $\mu\text{l}/\text{min}$ ) to remove the air in the system. Once the system is free of air, the pre-stained cell suspension is added to the microtrap array device at a flow rate of 50  $\mu\text{l}/\text{min}$  by switching the IDEX valve. When the cells trap inside the microtraps, the flow rate is reduced to 10  $\mu\text{l}/\text{min}$  for 10 minutes. Then, the IDEX valve is switched back to pure Opti-MEM supply at 10  $\mu\text{l}/\text{min}$ . Reduction in flow rate maintains the pressure on the cells but avoids uncontrolled cell accumulation. The input syringe containing cell suspension is then replaced by the syringe containing the target molecule, which is supplied at a flow rate of 10  $\mu\text{l}/\text{min}$ . The IDEX valve is now switched again so that the target biomolecule is supplied to the microtrap array device for 10 minutes. The flow is then stopped and the appropriate electric pulses are applied. Opti-MEM supplemented with 20% FBS is supplied to the microtrap array device at a flow rate of 0.01  $\mu\text{l}/\text{min}$  after the electric pulses are delivered during the electro-gene transfection experiments. This allowed us to maintain cell viability for more than 24 hours.

#### 4.2.5. FLUORESCENCE IMAGING OF MOLECULAR UPTAKE DURING MICROTRAP ARRAY ELECTROPORATION

To visualize the uptake of fluorescent molecules and GFP expression, we use an inverted fluorescent microscope (Zeiss Axio-Observer) equipped with a 10 $\times$  objective (Zeiss Plan-Apochromat 10 $\times$ /0.45 M27). This provides a field of view corresponding to  $\sim 1.29 \times 1.29 \text{ mm}^2$ . A light-emitting diode (LED) light source (Zeiss Colibri 7) is used with appropriate single bandpass filters for fluorescence imaging. The images are acquired using an Orca Flash 4.0 V2 (Hamamatsu) digital camera with a resolution of 2048 $\times$ 2048 px. The images are acquired at the following frame rates: (i) the propidium iodide uptake experiments were imaged at 2 Hz, and (ii) the GFP expression in the cells was monitored by imaging

at one frame per hour with an excitation/emission wavelength of 488/507 nm. The propidium iodide uptake and cell viability experiments were performed in triplicate at each voltage. The GFP expression experiments were done once at each voltage.

#### 4.2.6. NUMERICAL SIMULATION OF MICROTRAP ELECTROPORATION

Parameter	Value	Description
$\sigma_{\text{PDMS}}$	$4 \times 10^{-13}$ S/m	PDMS conductivity
$\epsilon_{\text{PDMS}}$	2.75	PDMS permittivity
$\sigma_e$	1.5 S/m	Extracellular conductivity
$\epsilon_e$	80	Extracellular permittivity
$\sigma_i$	0.5 S/m	Intracellular conductivity
$\epsilon_i$	80	Intracellular permittivity
$\epsilon_{\text{cm}}$	5	Cell membrane permittivity
$\sigma_{\text{cm}}$	$3 \times 10^{-7}$ S/m	Cell membrane conductivity
$V_{\text{ep}}$	0.258 V	Threshold electroporation voltage
$\alpha$	$1 \times 10^9$ m <sup>-2</sup> s <sup>-1</sup>	Electroporation parameter
$N_0$	$1.5 \times 10^9$ m <sup>-2</sup>	Equilibrium pore density when $V_m = 0$ V
$q$	2.46	Electroporation constant
$r_p$	$1 \times 10^{-9}$ m	Pore radius
$d_m$	$5 \times 10^{-9}$ m	Membrane thickness
$r$	$10 \times 10^{-6}$ m	Cell radius

Table 4.1: Parameters used for the numerical simulations in this study.

To calculate the electric potential ( $V$ ) distribution in the intracellular and extracellular space, the Laplace equation,

$$\nabla \left[ \frac{\partial \epsilon_{i,e} \nabla V}{\partial t} + (\sigma_{i,e}) \nabla V \right] = 0 \quad (4.1)$$

is solved using COMSOL Multiphysics 5.6 as a 3D time-dependent model. To minimize computational cost, we simulate one unit cell of the periodic array of traps with cells.  $\sigma$  is the electric conductivity,  $\epsilon$  is the dielectric permittivity of the intracellular (subscript i) and extracellular (subscript e) medium. The cell membrane is modelled via a distributed impedance boundary condition

$$\mathbf{n} \cdot \mathbf{J} = \frac{\sigma_m}{d_m} (V_i - V_e) + \frac{\epsilon_m}{d_m} \left( \frac{\partial V_i}{\partial t} - \frac{\partial V_e}{\partial t} \right) \quad (4.2)$$

where  $\mathbf{n}$  is the unit vector normal to the membrane surface,  $\mathbf{J}$  is the electric current density across the membrane, where as  $\sigma_m$ ,  $\epsilon_m$ ,  $d_m$  denote the membrane conductivity, dielectric permittivity and thickness respectively [42].  $V_i$  and  $V_e$  are the electric potential on the interior side and the exterior side of the cell membrane respectively. The transmembrane voltage  $V_m$  corresponds to the difference between the electric potentials on the two sides of the membrane ( $V_m = V_i - V_e$ ).

To numerically describe electroporation, we use the asymptotic model of electroporation [43–46]. The model describes the rate of formation of transient hydrophilic pores in the cell membrane which are permeant to ions and molecules as a function of  $V_m$ . According to the model, hydrophilic pores nucleate in the cell membrane at an initial radius  $r_p$  at a rate described by

$$\frac{dN}{dt} = \alpha e^{\left(\frac{V_m}{V_{ep}}\right)^2} \left(1 - \frac{N}{N_0} e^{-q\left(\frac{V_m}{V_{ep}}\right)^2}\right) \quad (4.3)$$

where  $N$  is the membrane pore density,  $N_0$  is the pore density in the non-electroporated membrane, and  $\alpha$ ,  $q$ , and  $V_{ep}$  are electroporation parameters. Once the cell membrane is porated, the cell membrane conductivity is described as

$$\sigma_{ep} = \frac{2\pi r_p^2 \sigma_p d_m N}{(\pi r_p + 2d_m)} \quad (4.4)$$

where the conductance of single pore  $\sigma_p = (\sigma_e - \sigma_i) / \log(\sigma_e / \sigma_i)$  and  $r_p$  is the radius of a single pore [46]. Membrane conductivity  $\sigma_m$  is thus the sum of the passive membrane conductivity  $\sigma_{cm}$  and  $\sigma_{ep}$ . Equations 4.1–4.4 were solved simultaneously with a linear system solver MUMPS.

The numerical models and AutoCAD designs used in this study are publicly available on [GitHub](https://github.com/aswinmuralidharan/Microtrap-Electroporation) (<https://github.com/aswinmuralidharan/Microtrap-Electroporation>).

## 4.3. RESULTS AND DISCUSSIONS

### 4.3.1. MICROTRAP ARRAY ELECTROPORATION HAS HIGH ELECTROPORATION EFFICIENCY AND MAINTAINS HIGH CELL VIABILITY

To investigate the effect of PDMS microtraps on the applied voltage, the electric potential distribution in the microchannel is estimated by solving the steady-state version of the equation 4.1 in a two-dimensional space using COMSOL Multiphysics, where  $\sigma$  is the conductivity, and  $\epsilon$  is the dielectric permittivity of the extracellular medium. The geometry of the device used for numerical simulations is in accordance with the chip used in the microtrap electroporation experiments (see supplementary information Fig. 4.6). To visualize the electric field amplification provided by the PDMS pillars in the microtrap array, the electric field amplification factor defined as  $E/E_{-traps}$ , where  $E$  is the local electric field and  $E_{-traps}$  is the applied electric field defined as the ratio of the applied voltage to the distance between conventional parallel plate electrodes, which would establish in the absence of the traps, is shown in Fig. 4.2(a). Fig. 4.2(a) demonstrates that the electric field is amplified approximately three times at the aperture of the microtrap. This means, at the center of the trap aperture, the electric field can get as high as 225 V/mm and 810 V/mm for an applied voltage-to-distance ratio of 90 V/mm and 320 V/mm, respectively (detailed figures are presented in the supplementary information Fig. 4.6 and Fig. 4.7). Furthermore, electric fields in each trap are identical, allowing us to perform electroporation of cells at high throughput, with all cells exposed to similar electric fields. The needle electrode configuration does not change the calculated electric field distribution considerably due to the high resistance of the microtrap array (see supplementary information Fig. 4.13).

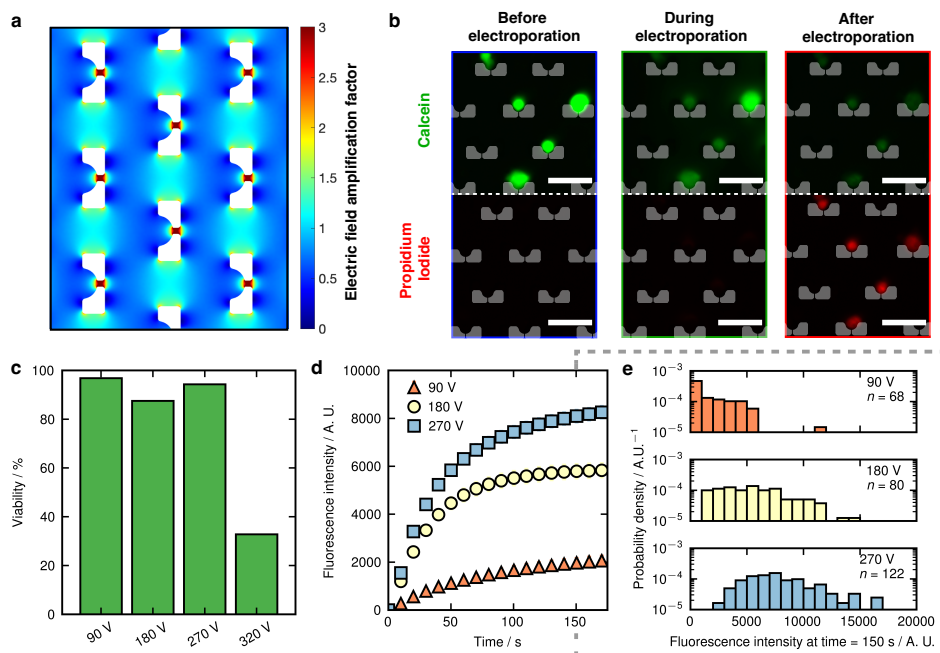


Figure 4.2: Influence of the microtrap array on the electric field, molecular uptake and cell viability. (a) Electric field distribution in the microfluidic device shows locally amplified electric fields near the traps enabling localized electroporation. The region with PDMS microtrap array is not displayed for ease of visualization. (b) *Top* : Efflux of calcein before electroporation (left), during electroporation (middle), and after electroporation (right). *Bottom* : Uptake of propidium iodide before electroporation (left), during electroporation (middle), and after electroporation (right) is shown. (c) Cell viability for different applied voltages is plotted. (d) Average fluorescence intensity of propidium iodide uptake from several cells (number of cells  $n = 68$  for 90 V, 80 for 180 V and 122 for 270 V) is plotted against time for different applied voltages. Raw data is provided in the supplementary information Fig. 4.8. (e) Histogram (bin size = 1000 A.U.) of propidium iodide fluorescence intensity at 150 s showing the cell to cell variability in the uptake of propidium iodide. Scale bar is 50  $\mu\text{m}$ .

To investigate which operating voltages provide reversible electroporation conditions in the microtrap array, we experimentally investigated the influence of the applied voltage on the cell viability and small molecule electrotransfer to CHO-K1 cells. To do so, we trapped Calcein AM (green) stained CHO-K1 cells in the microtrap array and applied single electric pulses with voltages ranging from 90 V to 320 V with a pulse duration of 5 ms. When the cells are electroporated, the Calcein is rapidly expelled from the cells through the electroporated cell membrane as shown in Fig. 4.2(b, top row). The electroporated cell membrane is then allowed to recover for 1 hour. One hour after applying electric pulses, a solution of Calcein Red AM (red) in Opti-MEM is supplied to the microchannel for 20 minutes. The channels are then flushed with Opti-MEM to remove any residual Calcein Red AM. Calcein Red AM is cell membrane permeable and is cleaved by live cells to form fluorescent Calcein molecules, which allows us to estimate the number of live cells after electroporation. We count the number of cells exhibiting red fluorescence to calculate the percentage of viable cells. We estimate between > 90 %

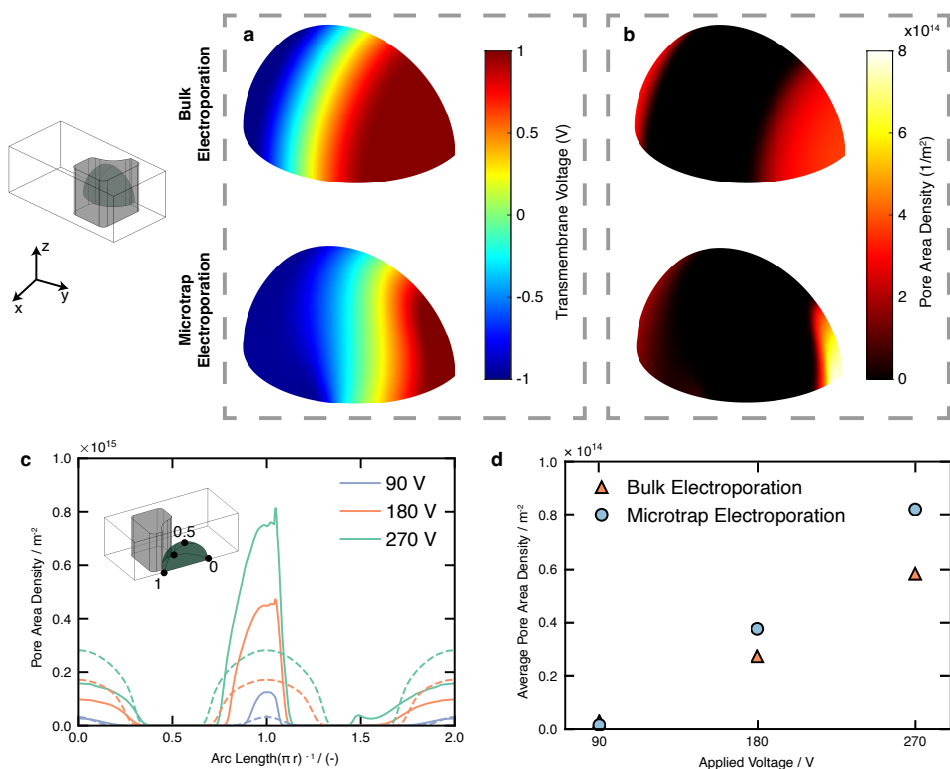


Figure 4.3: Numerical simulations of electroporation in bulk and microtrap array. The orientation of the cell in the displayed results is shown. (a) The induced transmembrane voltage in bulk electroporation (top) and microtrap electroporation (bottom) shows that the microtrap alters the induced transmembrane voltage. (b) Pore area density in bulk electroporation (top) and microtrap electroporation (bottom) demonstrate localized electroporation near the microtrap aperture. These results correspond to an applied voltage drop of 270 V across the electrodes in the experiments. (c) Pore area density is plotted against the arc length normalized by  $\pi r$ . As shown in the inset, 0 in the variable shown in the x-axis corresponds to the point in the cell membrane on the side opposite to the microtrap aperture, 1 to the point in the cell membrane on the side of trap aperture. The voltages shown in the legend correspond to the voltage drop across the electrodes in the experiments. The solid lines correspond to microtrap electroporation while the dashed lines represent equivalent bulk electroporation. (d) Surface average pore area density on the simulated cell surface for different applied voltages for bulk electroporation and microtrap electroporation.

cell viability for applied voltages between 90 V and 270 V, followed by a sharp decrease to  $\sim 30\%$  cell viability at 320 V as shown in Fig. 4.2(c). Hence, we set our operating voltage range for molecular delivery with reversible electroporation between 90 V and 270 V.

#### 4.3.2. ANALYSIS OF SMALL MOLECULES UPTAKE WITH MICROTRAP ARRAY ELECTROPORATION

To study the small molecule electrotransfer to the cell in the microtrap array on a chip, we monitor the electrotransfer of propidium iodide to CHO-K1 cells as a response to

single 5 ms long electric pulse of various applied voltages (90 V to 270 V) *in situ* using an inverted fluorescence microscope. Propidium ions are cell membrane impermeant and emit a strong fluorescence (excitation/emission 535 nm/615 nm) upon entry to a cell by binding to the nucleic acids present inside the cell [47–49]. The enhancement in propidium fluorescence intensity can hence be used as a marker for cell membrane permeabilization as a response to electric pulses, as shown in Fig. 4.2(b) (bottom panels). Fig. 4.2(d) shows that propidium ions enter the cells at voltages from 90 V (lower voltages were not tested). We observed nearly 100% of the cells become permeable to propidium ions upon electroporation in the tested conditions. Suppose  $\tau$  is the resealing time of the cell membrane,  $A_{p0}$  is the initial electroporated area,  $d_m$  is the thickness of the cell membrane,  $D$  is the diffusion coefficient of propidium ions in the electroporation buffer,  $V$  is the volume of the cell, and  $c_e$  is the extracellular propidium concentration. Then, the concentration of bound propidium ions which emit the fluorescence at time  $t$  can be expressed as [47, 49, 50].

$$[\text{PIB}] = \frac{Dc_e A_{p0} \tau}{V d_m} (1 - \exp(-t/\tau)). \quad (4.5)$$

To assess the influence of applied voltage on the cell resealing time during microtrap electroporation, we extracted the resealing time  $\tau$  and  $I_{\max} = Dc_e A_{p0} \tau / V d$  by fitting the bound propidium fluorescence intensity time series with equation 4.5. We observe that the highest resealing time is for the lowest tested voltage (90 V) ( $\sim 62 \pm 4$  s). At higher voltages, we observe lower resealing times ( $\sim 35 \pm 2$  s for 180 V and  $\sim 42 \pm 2$  s for 270 V). The distribution of fluorescence intensity in the electrotransferred cells at time  $t = 150$  s after electrotransfer (i.e., a time point long after the resealing time) is plotted in Fig. 4.2(e). Since the time scale of molecular uptake is much greater than the duration of the electric pulse, post pulse diffusion is the driving force for the molecular uptake for the small molecule electrotransfer in the microtrap array electroporation [47]. The mean propidium fluorescence intensity shifts to higher values with increasing applied voltages, implying that more molecules are electrotransferred at higher voltages despite lower resealing times (see Fig. 4.17). This means that there is a higher degree of electroporation at higher applied voltages. We then extracted  $I_{\max}/\tau = Dc_e A_{p0} / V d$  to estimate the increase in permeabilized area for different applied voltages. We estimate that  $I_{\max}/\tau = 69 \pm 28$  for 90 V,  $208 \pm 16$  for 180 V, and  $298 \pm 34$  for 270 V. Since all the parameters in the definition of  $I_{\max}/\tau$  except the initial permeabilized area is independent of applied voltage, this means that there is  $\sim 4.3$  times more porated area at 270 V compared to 90V in the microtrap electroporation.

We then compared the effectiveness of the microtrap electroporation to the bulk electroporation. To do so, we plated Calcein stained CHO cells suspended in cell culture media on four well-chambered glass slides 1 hour prior to applying electric pulses. The cell culture media was replaced with Opti-MEM, which contained the same concentration of PI (25  $\mu\text{M}$ ) as in microtrap electroporation. The electric pulses were applied through stainless steel electrodes placed parallel to each other and separated by a distance of 3 mm connected to the same pulse generator used for the microtrap electroporation system. We then applied a single 5 ms pulse of 270 V (comparable to the situation in microtrap electroporation with a voltage drop of 90 V since the electrodes in

bulk electroporation are separated by 3 mm while in microtrap electroporation is separated by 1 mm). In contrast to microtrap electroporation, we observed minimal uptake of PI, which shows that the microtrap electroporation device is more effective in electroporating CHO cells than bulk electroporation. We analyzed PI uptake from 280 cells and observed that the fluorescence intensity of the cells 150 seconds after bulk electroporation was  $251 \pm 12$  A.U. (see supplementary information Fig. 4.10), while in microtrap electroporation under the same conditions, it was  $1948 \pm 248$  A.U. Since the PI fluorescence signal after bulk electroporation provided a poor signal to noise ratio, we could not extract the fitting parameters using the equation 4.5. These results demonstrate that microtrap electroporation is more effective in electroporating and transferring exogenous biomolecules than bulk electroporation.

#### 4.3.3. MICROTRAP ARRAY ELECTROPORATION INDUCES LOCALIZED CELL MEMBRANE ELECTROPORATION

To investigate how the application of electric fields across the microtrap array provides a high degree of electroporation, we performed numerical simulations of electroporation using the asymptotic model of electroporation [45] (for the simulation geometry see supplementary information Fig. 4.14). To test the validity of the numerical solutions, we first estimated the electric field distribution and induced transmembrane voltage of an isolated cell in a homogeneous electric field without the pore formation equations. We show that our numerical solution agrees well with the analytical solution for the induced transmembrane voltage,  $V_m = 1.5Er \cos\theta(1 - \exp(-t/\tau_m))$  [51] (see supplementary information Fig. 4.11). Here,  $r$  is the radius of the cell,  $\tau_m$  is the membrane charging time,  $E$  is the electric field, and  $\theta$  is the angle measured from the center of the cell with respect to the direction of the electric field. To estimate which voltage drop to apply across each unit cell in our simulation, we measured the voltage drop across a unit cell of width  $48.8 \mu\text{m}$  (see supplementary information Fig. 4.12) from the 2D model discussed in the previous section. An applied voltage difference of 90 V, 180 V, and 270 V across electrodes in the experiment corresponds to a voltage drop of 3.6 V, 7.36 V, and 11.05 V across the simulation unit cell. One electrode was excited by a 5 ms rectangular pulse of the amplitude corresponding to this measured voltage drop by subtracting two Heaviside step functions. The second electrode was set to ground.

Having established that our numerical solutions capture the induced transmembrane voltage without poration well, we then include the pore formation equations in the model. Fig. 4.3(a) shows that the presence of the microtrap alters the induced transmembrane voltage. The high induced transmembrane voltage regions is localized near the microtrap aperture in microtrap array electroporation than bulk electroporation (see supplementary information Fig. 4.15). As a consequence of the high local induced transmembrane voltage, microtrap electroporation can lead to 2 to 3 times greater local pore area density near the trap aperture compared to the bulk electroporation, as shown in Fig. 4.3(b),(c). Besides the local amplification of pore formation near the trap aperture, the rest of the cell membrane display diminished pore formation as we show in Fig. 4.3(c). As a result, at 90 V, the average pore area density is comparable in both microtrap electroporation and bulk electroporation. Fig. 4.3(d) shows that microtrap electroporation at 180 V and 270 V leads to  $\sim 40\%$  higher pore area density than bulk elec-



troportion and has over three times higher pore area density near the trap aperture. Deformation of the cells in the trap aperture shows no appreciable increase in pore area density (see supplementary information Fig. 4.16).

Our numerical simulations show that the high efficiency of electroporation in the microtrap electroporation is possibly due to the enhanced poration at the trap aperture. The shielding of the cell membrane from the electric field by the PDMS microtrap reduces the poration away from the trap, causing improved cell viability during and after the microtrap electroporation procedure.

#### 4.3.4. PLASMID DNA ELECTROTRANSFER IN MICROTRAP ARRAY INDUCE EFFICIENT GENE TRANSFECTION

4

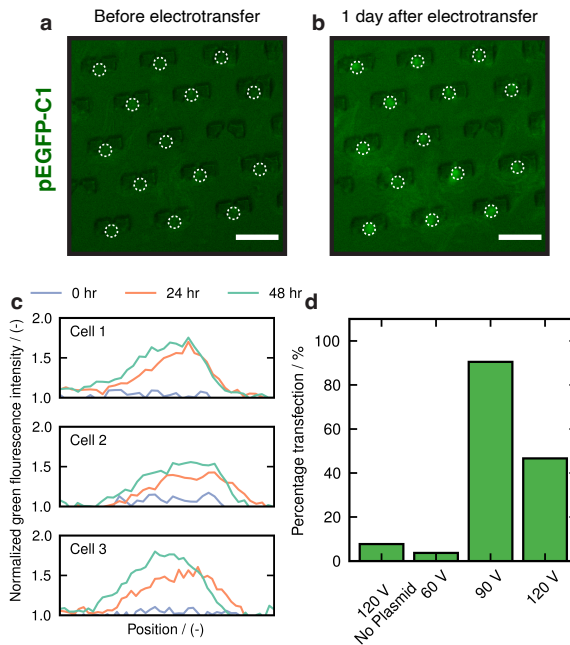


Figure 4.4: GFP expression in microtrap array electroporation device using pEGFP-C1 plasmid DNA. (a),(b) Fluorescence microscopy images of the microtrap array with trapped cells (highlighted by dotted white circles) (a) before electroporation (b) one day after electroporation. The images shown are from experiment where 10 pulses of 90 V, each 5 ms long were applied. (c) Three representative examples of increase in green fluorescence intensity across the cross section of cell after electrotransfer of pEGFP-C1 plasmids are presented. The fluorescence intensity is measured at three time points, 0 hour (immediately after electroporation), 1 day and 2 days after electroporation. These cells are from the experiment with an applied voltage difference of 90 V. The fluorescence intensity is normalized by the fluorescence intensity at time = 0 hr. (d) Percentage of cells showing transfection at different applied voltage conditions (90 V and 120 V, 10 pulses of 5 ms each) one day after electroporation. Scale bar is 50  $\mu$ m.

Our geometry's high local electric fields lead to enhanced delivery of charged macromolecules such as DNA (negatively charged) to the cells. We hypothesize that this lead to better transfection at voltage conditions which do not cause a loss in cell viability. To

test this, we delivered plasmid DNA (pEGFP-C1) encoding a green fluorescent protein (GFP) to CHO-K1 cells at two voltage conditions at which the single cells are permeabilized (90 V, 120 V, ten pulses of 5 milliseconds each at 1 Hz) and one voltage condition at which the single cells are not permeabilized (60 V, ten pulses of 5 milliseconds each at 1 Hz) in the microtrap device. As a negative control, we electroporated cells in the microtrap array without the plasmid DNA (120 V, ten pulses of 5 milliseconds each at 1 Hz). Fig. 4.4(a),(b) shows that upon electroporation of the CHO cells in the presence of the pEGFP-C1 plasmid DNA, cells display an enhanced green fluorescence for an applied voltage condition of 90 V. We measured the fluorescence intensity inside the cells at different time points in Fiji by manually selecting a region of interest that outlines the boundary of the cells (the region of interest are chosen in the first frame based on the Calcein Red channel used to stain the cells). Random shifts in the location of the cells during the time series imaging are manually corrected in Fiji. We observe  $\sim 30\%$  increase in green fluorescence intensity of the cells after one day for an applied voltage of 90 V and 120 V in the microtrap electroporation device (supplementary information Fig. 4.17). To avoid photobleaching and phototoxicity, we used short exposure times, and to get as many cells as possible within the same frame, we used a low magnification ( $10\times$ ). We believe these effects lead to the low increase in fluorescence intensity that we observe. We confirmed that the increase in the fluorescence intensity is more than that of changes in the background fluorescence intensity after evaluating the background fluorescence intensity in randomly selected cell-sized regions of interest (see supplementary information Fig. 4.17). We plot the fluorescence intensity (normalized by the fluorescence intensity at time = 0 hr) across three representative cells (across the cell diameter) before electroporation, one day and two days after electroporation in the microtrap array in Fig. 4.4(c). Fig. 4.4(c) shows that the cells display a markedly higher fluorescence than the background fluorescence intensity. We then quantified the percentage transfection based on the percentage of cells that showed a 20% increase in the green fluorescence intensity (only cells that showed a 20% increase in fluorescence intensity, and more than that of the background level increase were considered as transfected cells). We show in Fig. 4.4(d) that almost  $> 90\%$  of cells express green fluorescent protein at the applied voltage of 90 V and 120 V within 24 hours. For the applied voltage of 120 V,  $\sim 45\%$  are transfected, while for 60 V, only  $\sim 3\%$  cells display an increase in fluorescence intensity after electroporation in the presence of the pEGFP-C1 plasmids. In the negative control performed at 120 V in the absence of plasmid DNA,  $\sim 7\%$  cells showed a 20% increase in green fluorescence intensity.

In contrast to small molecules such as propidium iodide, larger charged plasmid DNA first forms DNA-membrane complexes upon electrotransfer and is later internalized through cellular machinery [52–55]. Since the intracellular release of plasmid DNA is difficult to control without the use of endosomal/nuclear disrupting or redirecting agents [56–58], the amount of plasmid DNA that forms the DNA membrane complex and the cell viability is key to successful cell transfection [59, 60]. We believe, the high local electric fields cause electrophoretic drift of large amounts of plasmid DNA towards the cell membrane upon application of electric pulses. Furthermore, as demonstrated in the previous sections, our device provides improved cell viability. The combination of a high local concentration of plasmid DNA and good cell viability allows the device to transfect

the cells successfully.

#### 4.4. CONCLUSIONS

A microfluidic device that enables localized electroporation in a microtrap array is presented. The simple working mechanism of the device allows the positioning of the cell to locations with high local electric fields by the flow. The device is compatible with delivering membrane-impermeable small molecules such as fluorescent tracer molecules and larger charged molecules such as plasmid DNA. Electroporation in this device enables the transfer of molecules while preserving cell viability. A high degree of gene transfection is obtained when protein-encoding plasmid DNA is electrotransferred with this device. The micro trap electroporation device demonstrated here is expected to open up the possibility for a robust localized electroporation procedure (with perfect cell viability and uniformity) in gene therapy, *ex vivo* applications (based on adoptive immunotherapy), and drug delivery applications.

#### CHAPTER COVER

A scanning electron microscopy image of the microtrap array electroporation device.

## APPENDIX

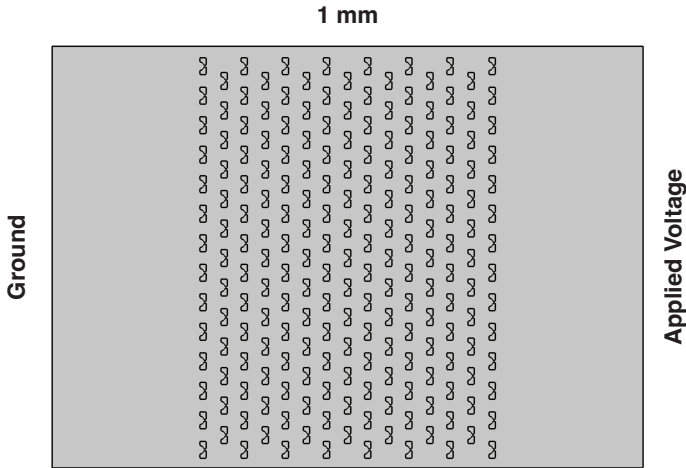
**4.A. NUMERICAL CALCULATIONS OF ELECTRIC FIELD DISTRIBUTIONS IN THE MICROFLUIDIC DEVICE.**

Figure 4.5: Geometry and boundary conditions used for estimating electric field distribution in the microfluidic channel. The microtrap array is modelled with the properties of PDMS and the remaining with that of extracellular medium.

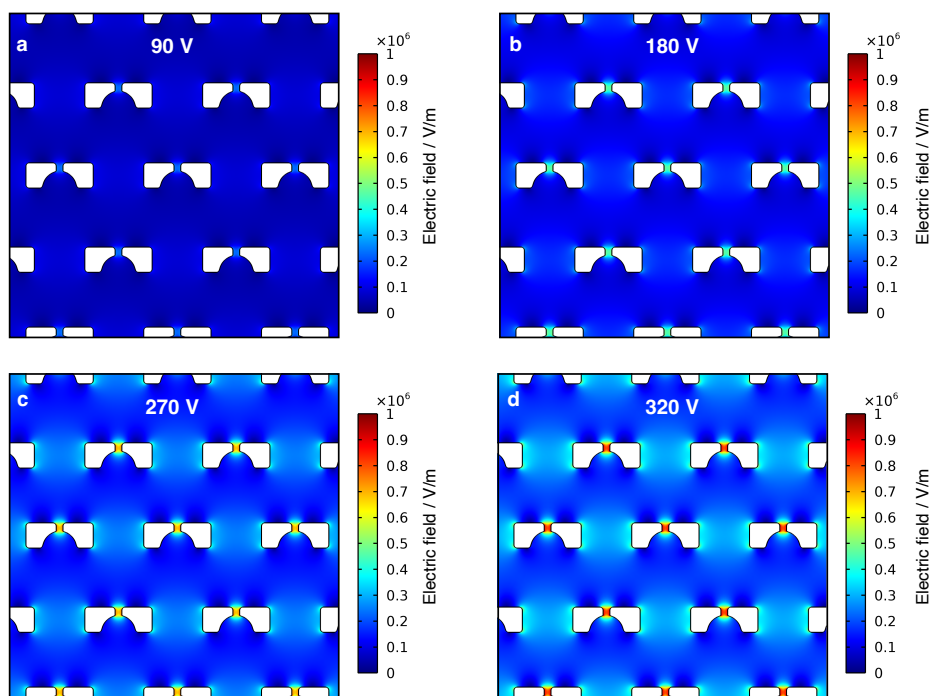


Figure 4.6: Comparison of electric field distribution in the microtrap array for different applied voltages (a) 90 V, (b) 180 V, (c) 270 V, (d) 320 V. The region with PDMS micro trap array is removed for better clarity.

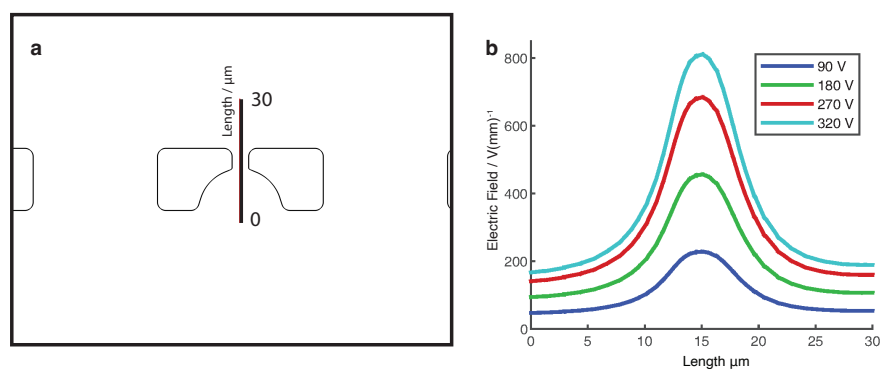


Figure 4.7: Electric field across the cut line shown in (a) shown in (b) shows almost a three fold increase in the electric field in the trap aperture for different applied voltages.

## 4.B. ANALYSIS OF SMALL MOLECULE ELECTROTRANSFER

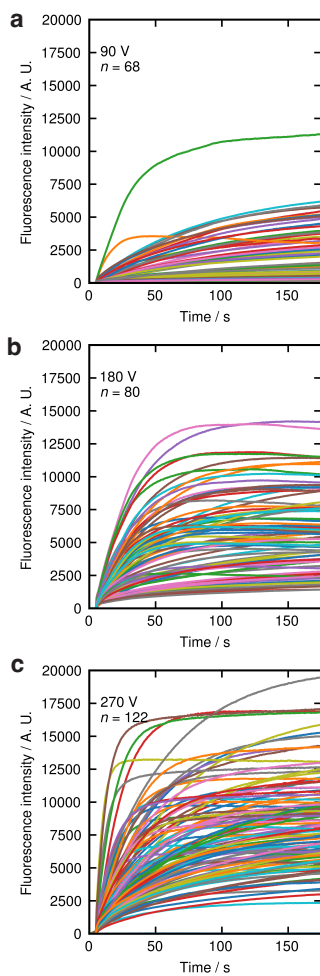


Figure 4.8: Temporal evolution of the total fluorescent intensity in different cells when propidium iodide is electrotransferred to CHO cells using microtrap array electroporation. Individual solid lines represent uptake in individual cells. (a) 90 V, (b) 180 V, (c) 270 V. Only 1 pulse which is 5 ms long is applied in these experiments.

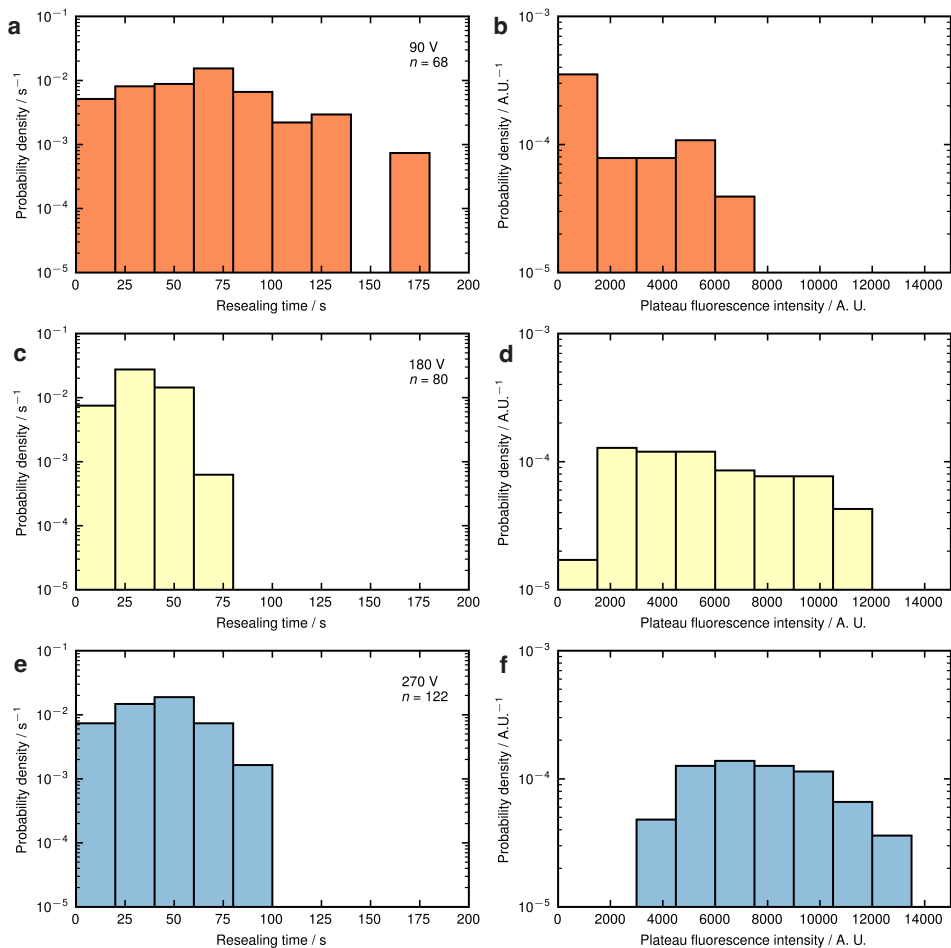


Figure 4.9: (a), (c), (d) Probability density distribution of resealing time (bin size = 20 s) measured from propidium iodide uptake experiments for (a) 90 V, (c) 180 V, and (e) 270 V. (b), (d), (e) Probability density distribution of plateau fluorescence intensity (bin size = 1500 A.U.) measured from propidium iodide uptake experiments for (b) 90 V, (d) 180 V, and (f) 270 V. Only 1 pulse which is 5 ms long is applied in these experiments.

## 4.C. BULK ELECTROPORATION

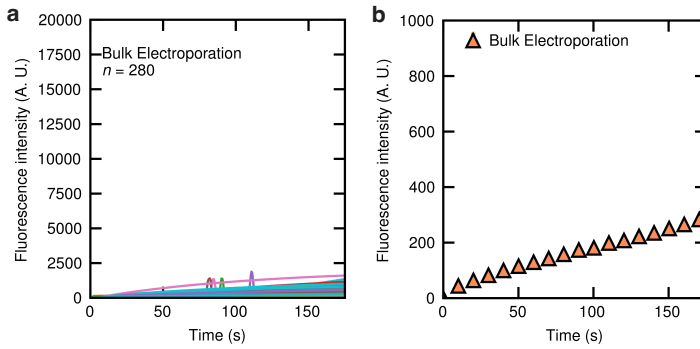


Figure 4.10: (a) Temporal evolution of the total fluorescent intensity in different cells when propidium iodide is electrotransferred to CHO cells using bulk electroporation (applied voltage = 270 V, 1 pulse of 5 ms, which is equivalent to 90 V, 1 pulse of 5 ms in microtrap electroporation). Individual solid lines represent uptake in individual cells. (b) Average fluorescent intensity profile against time for the bulk electroporation (from the same dataset shown in (a)).



#### 4.D. NUMERICAL CALCULATIONS OF ELECTROPORATION

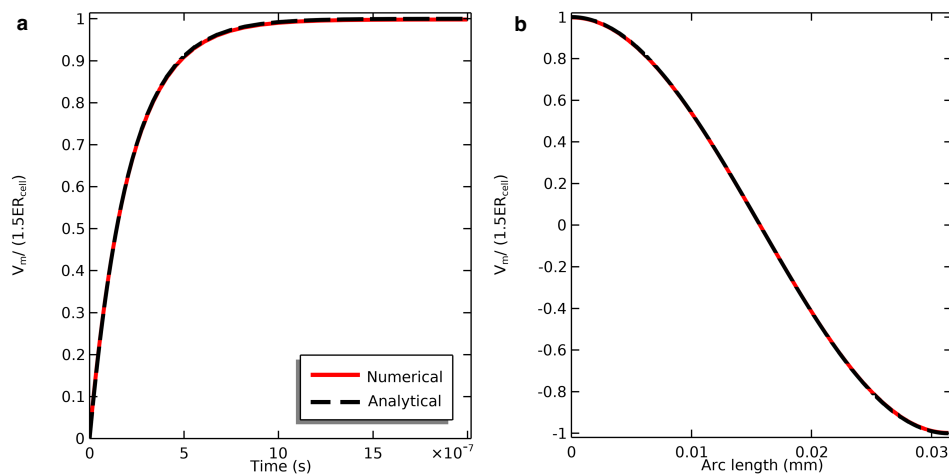


Figure 4.11: Validation of electric field distribution for our simulations in absence of pore formation models. In red numerical calculations are plotted and black lines represent analytical solution mentioned in the main manuscript. (a) The normalized transmembrane voltage is plotted against time. (b) Normalized transmembrane voltage is plotted against the arc length.

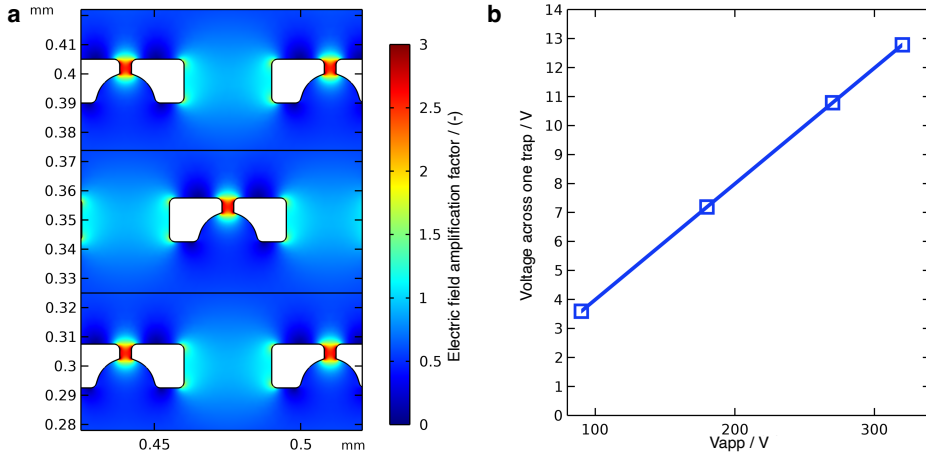


Figure 4.12: Determining the voltage drop across boundaries in each unit cell. (a) Voltage drop was determined across the cutlines (see in black). The cutlines are 48.8  $\mu\text{m}$  apart and represent the width of one unit cell. (b) The corresponding voltage difference across two cut lines for different applied voltages.

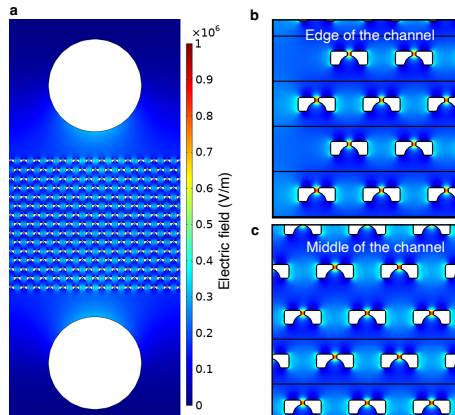


Figure 4.13: (a) Electric field distribution in the microtrap array when needle electrodes are used. The shown contours are for an applied voltage = 270 V. (b) Zoomed in view at the edge of the channel. (c) Zoomed in view at the middle of the channel. The edge to edge distance of the electrodes are set to 1 mm.

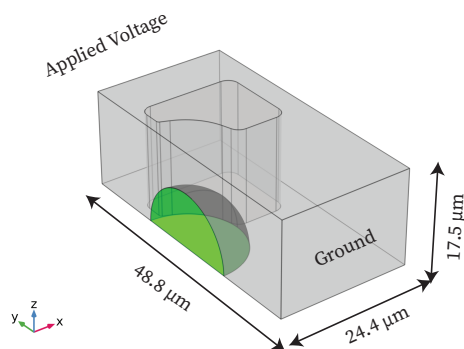


Figure 4.14: Geometry file used for simulating electroporation of a cell in a microtrap array. The plane along center of the cell (in green) is used as a center of symmetry for reducing computational cost. Microtrap (in white) is modelled with the material properties of PDMS. Extracellular medium (in light gray) is modelled with material properties of extracellular medium. The cell membrane (in dark gray) is modelled via a distributed impedance boundary condition.

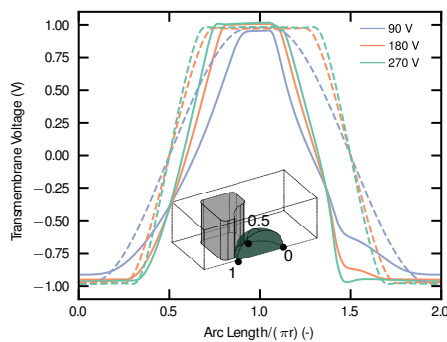


Figure 4.15: Transmembrane voltage is plotted against the arc length normalized by  $\pi r$ . As shown in the inset, 0 in the variable shown in the x-axis corresponds to the point in the cell membrane on the side opposite to the microtrap aperture, 1 to the point in the cell membrane on the side of trap aperture. The voltages shown in the legend correspond to the voltage drop across the electrodes in the experiments.

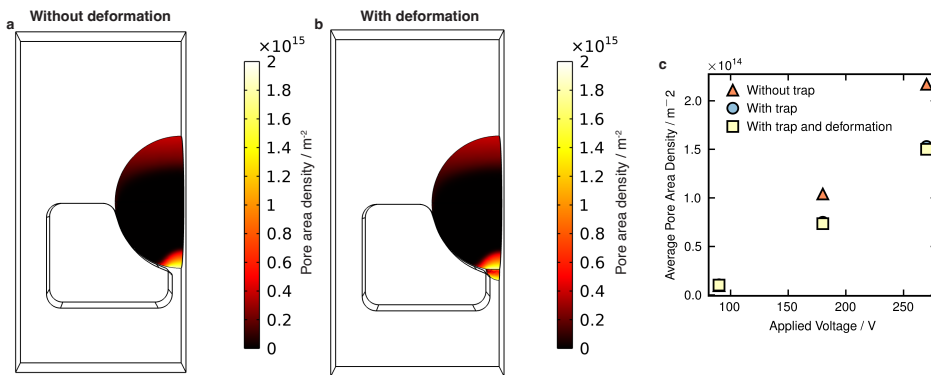


Figure 4.16: Numerical calculations for estimating the influence of the cell deformation on electroporation. (a) Pore area density for a cell with no deformation exposed to applied voltage of 270 V. (b) Pore area density for a deformed cell exposed to applied voltage of 270 V. (c) Average pore area density for different applied voltages are compared under following configurations: bulk electroporation of undeformed cell, an undeformed cell in the microtrap, a deformed cell in the microtrap. These simulations are done under assumption of needle electrode configuration.

## 4.E. ANALYSIS OF GFP EXPRESSION

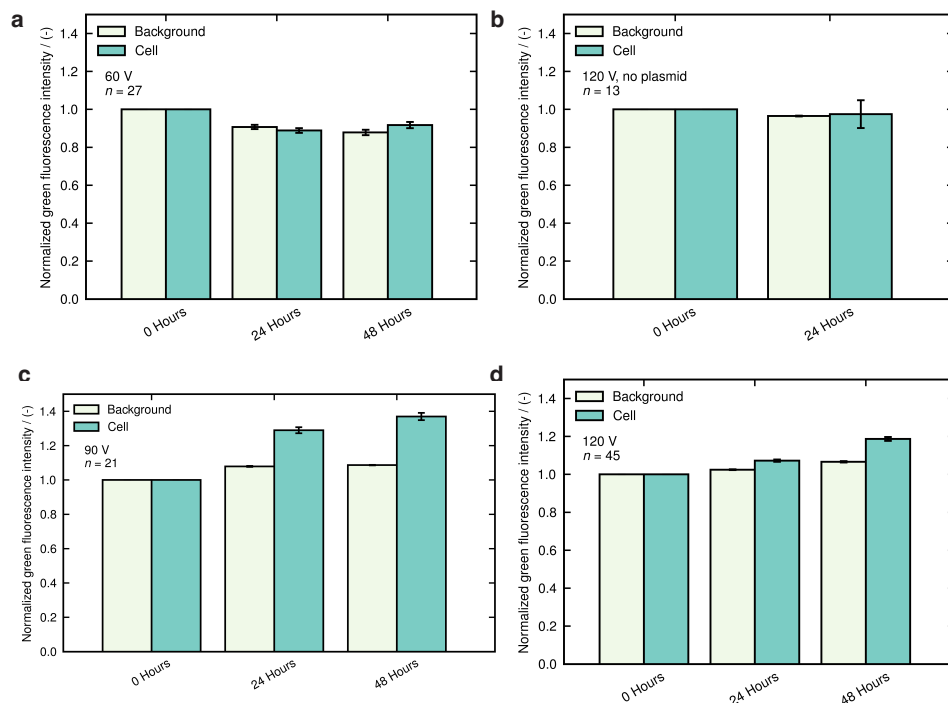


Figure 4.17: Increase in fluorescence intensity of the cell after electrotransfer of pEGFP-C1 plasmids. The fluorescence intensity is measured at three time points, 0 hour (immediately after electroporation), 1 day and 2 days after electroporation. (a) These cells are from the experiment with an applied voltage difference of 60 V. (b) These cells are from the experiment with an applied voltage difference of 90 V. (c) These cells are from the experiment with an applied voltage difference of 120 V. The fluorescence intensity is normalized by the fluorescence intensity at time = 0 hr. The background corresponds to the average fluorescence intensity from 27 for (b), 21 for (c), and 45 for (d) randomly chosen cell sized circles in the imaging frame. This shows the cell fluorescence intensity increase can be attributed to successful GFP expression in the cells.

## REFERENCES

- [1] A. Muralidharan, G. R. Pesch, H. Hubbe, L. Rems, M. Nouri-Goushki, and P. E. Boukany, *Microtrap array on a chip for localized electroporation and electro-gene transfection*, *Bioelectrochemistry* **147**, 108197 (2022).
- [2] M. R. Prausnitz, V. G. Bose, R. Langer, and J. C. Weaver, *Electroporation of mammalian skin: a mechanism to enhance transdermal drug delivery*, *Proceedings of the National Academy of Sciences* **90**, 10504 (1993).
- [3] L. M. Mir, M. F. Bureau, J. Gehl, R. Rangara, D. Rouy, J.-M. Caillaud, P. Delaere, D. Branellec, B. Schwartz, and D. Scherman, *High-efficiency gene transfer into skele-*

- tal muscle mediated by electric pulses*, Proceedings of the National Academy of Sciences **96**, 4262 (1999).
- [4] M. L. Yarmush, A. Golberg, G. Serša, T. Kotnik, and D. Miklavčič, *Electroporation-based technologies for medicine: principles, applications, and challenges*, Annual Review of Biomedical Engineering **16**, 295 (2014).
- [5] W. Kang, R. L. McNaughton, and H. D. Espinosa, *Micro-and nanoscale technologies for delivery into adherent cells*, Trends in Biotechnology **34**, 665 (2016).
- [6] M. P. Stewart, R. Langer, and K. F. Jensen, *Intracellular delivery by membrane disruption: mechanisms, strategies, and concepts*, Chemical Reviews **118**, 7409 (2018).
- [7] J. Brooks, G. Minnick, P. Mukherjee, A. Jaber, L. Chang, H. D. Espinosa, and R. Yang, *High throughput and highly controllable methods for in vitro intracellular delivery*, Small **16**, 2004917 (2020).
- [8] P. J. Canatella, J. F. Karr, J. A. Petros, and M. R. Prausnitz, *Quantitative study of electroporation-mediated molecular uptake and cell viability*, Biophysical Journal **80**, 755 (2001).
- [9] S. Sachdev, T. Potočnik, L. Rems, and D. Miklavčič, *Revisiting the role of pulsed electric fields in overcoming the barriers to in vivo gene electrotransfer*, Bioelectrochemistry, 107994 (2021).
- [10] P. E. Boukany, A. Morss, W.-c. Liao, B. Henslee, H. Jung, X. Zhang, B. Yu, X. Wang, Y. Wu, L. Li, *et al.*, *Nanochannel electroporation delivers precise amounts of biomolecules into living cells*, Nature Nanotechnology **6**, 747 (2011).
- [11] Y. Cao, E. Ma, S. Cestellos-Blanco, B. Zhang, R. Qiu, Y. Su, J. A. Doudna, and P. Yang, *Nontoxic nanopore electroporation for effective intracellular delivery of biological macromolecules*, Proceedings of the National Academy of Sciences **116**, 7899 (2019).
- [12] S. Wang and L. J. Lee, *Micro-/nanofluidics based cell electroporation*, Biomicrofluidics **7**, 011301 (2013).
- [13] L. Rems, D. Kawale, L. J. Lee, and P. E. Boukany, *Flow of DNA in micro/nanofluidics: From fundamentals to applications*, Biomicrofluidics **10**, 043403 (2016).
- [14] M. Khine, A. Lau, C. Ionescu-Zanetti, J. Seo, and L. P. Lee, *A single cell electroporation chip*, Lab on a Chip **5**, 38 (2005).
- [15] H. Lu, M. A. Schmidt, and K. F. Jensen, *A microfluidic electroporation device for cell lysis*, Lab on a Chip **5**, 23 (2005).
- [16] K. Gao, L. Li, L. He, K. Hinkle, Y. Wu, J. Ma, L. Chang, X. Zhao, D. G. Perez, S. Eckardt, *et al.*, *Design of a microchannel-nanochannel-microchannel array based nanoelectroporation system for precise gene transfection*, Small **10**, 1015 (2014).

- [17] L. Chang, M. Howdysshell, W.-C. Liao, C.-L. Chiang, D. Gallego-Perez, Z. Yang, W. Lu, J. C. Byrd, N. Muthusamy, L. J. Lee, *et al.*, *Magnetic tweezers-based 3d microchannel electroporation for high-throughput gene transfection in living cells*, *Small* **11**, 1818 (2015).
- [18] L. Chang, D. Gallego-Perez, X. Zhao, P. Bertani, Z. Yang, C.-L. Chiang, V. Malkoc, J. Shi, C. K. Sen, L. Odonnell, *et al.*, *Dielectrophoresis-assisted 3d nanoelectroporation for non-viral cell transfection in adoptive immunotherapy*, *Lab on a Chip* **15**, 3147 (2015).
- [19] L. Chang, D. Gallego-Perez, C.-L. Chiang, P. Bertani, T. Kuang, Y. Sheng, F. Chen, Z. Chen, J. Shi, H. Yang, *et al.*, *Controllable large-scale transfection of primary mammalian cardiomyocytes on a nanochannel array platform*, *Small* **12**, 5971 (2016).
- [20] D. Gallego-Perez, L. Chang, J. Shi, J. Ma, S.-H. Kim, X. Zhao, V. Malkoc, X. Wang, M. Minata, K. J. Kwak, *et al.*, *On-chip clonal analysis of glioma-stem-cell motility and therapy resistance*, *Nano Letters* **16**, 5326 (2016).
- [21] L. Chang, P. Bertani, D. Gallego-Perez, Z. Yang, F. Chen, C. Chiang, V. Malkoc, T. Kuang, K. Gao, L. J. Lee, *et al.*, *3d nanochannel electroporation for high-throughput cell transfection with high uniformity and dosage control*, *Nanoscale* **8**, 243 (2016).
- [22] D. Gallego-Pérez, D. Pal, S. Ghatak, V. Malkoc, N. Higueta-Castro, S. Gnyawali, L. Chang, W.-C. Liao, J. Shi, M. Sinha, *et al.*, *Topical tissue nano-transfection mediates non-viral stroma reprogramming and rescue*, *Nature Nanotechnology* **12**, 974 (2017).
- [23] P. Mukherjee, S. S. P. Nathamgari, J. A. Kessler, and H. D. Espinosa, *Combined numerical and experimental investigation of localized electroporation-based cell transfection and sampling*, *ACS Nano* **12**, 12118 (2018).
- [24] Z. Yang, J. Shi, J. Xie, Y. Wang, J. Sun, T. Liu, Y. Zhao, X. Zhao, X. Wang, Y. Ma, *et al.*, *Large-scale generation of functional mrna-encapsulating exosomes via cellular nanoporation*, *Nature Biomedical Engineering* **4**, 69 (2020).
- [25] Z. Fei, S. Wang, Y. Xie, B. E. Henslee, C. G. Koh, and L. J. Lee, *Gene transfection of mammalian cells using membrane sandwich electroporation*, *Analytical Chemistry* **79**, 5719 (2007).
- [26] X. Xie, A. M. Xu, S. Leal-Ortiz, Y. Cao, C. C. Garner, and N. A. Melosh, *Nanostraw-electroporation system for highly efficient intracellular delivery and transfection*, *ACS Nano* **7**, 4351 (2013).
- [27] Y. Cao, H. Chen, R. Qiu, M. Hanna, E. Ma, M. Hjort, A. Zhang, R. Lewis, J. Wu, and N. Melosh, *Universal intracellular biomolecule delivery with precise dosage control*, *Science Advances* **4**, eaat8131 (2018).

- [28] G. He, J. Feng, A. Zhang, L. Zhou, R. Wen, J. Wu, C. Yang, J. Yang, C. Li, D. Chen, *et al.*, *Multifunctional branched nanostraw-electroporation platform for intracellular regulation and monitoring of circulating tumor cells*, *Nano Letters* **19**, 7201 (2019).
- [29] X. Liu, A.-Y. Chang, Y. Ma, L. Hua, Z. Yang, and S. Wang, *Robust three-dimensional nanotube-in-micropillar array electrodes to facilitate size independent electroporation in blood cell therapy*, *Lab on a Chip* (2021).
- [30] W. Kang, F. Yavari, M. Minary-Jolandan, J. P. Giraldo-Vela, A. Safi, R. L. McNaughton, V. Parpoil, and H. D. Espinosa, *Nanofountain probe electroporation (nfp-e) of single cells*, *Nano Letters* **13**, 2448 (2013).
- [31] R. Yang, V. Lemaître, C. Huang, A. Haddadi, R. McNaughton, and H. D. Espinosa, *Monoclonal cell line generation and crispr/cas9 manipulation via single-cell electroporation*, *Small* **14**, 1702495 (2018).
- [32] S. S. P. Nathamgari, N. Pathak, V. Lemaitre, P. Mukherjee, J. J. Muldoon, C.-Y. Peng, T. McGuire, J. N. Leonard, J. A. Kessler, and H. D. Espinosa, *Nanofountain probe electroporation enables versatile single-cell intracellular delivery and investigation of postpulse electropore dynamics*, *Small* **16**, 2002616 (2020).
- [33] S.-O. Choi, Y.-C. Kim, J. W. Lee, J.-H. Park, M. R. Prausnitz, and M. G. Allen, *Intracellular protein delivery and gene transfection by electroporation using a microneedle electrode array*, *Small* **8**, 1081 (2012).
- [34] D. Xia, R. Jin, G. Byagathvalli, H. Yu, L. Ye, C.-Y. Lu, M. S. Bhamla, C. Yang, and M. R. Prausnitz, *An ultra-low-cost electroporator with microneedle electrodes (epatch) for sars-cov-2 vaccination*, *Proceedings of the National Academy of Sciences* **118** (2021).
- [35] Y. Xuan, S. Ghatak, A. Clark, Z. Li, S. Khanna, D. Pak, M. Agarwal, S. Roy, P. Duda, and C. K. Sen, *Fabrication and use of silicon hollow-needle arrays to achieve tissue nanotransfection in mouse tissue in vivo*, *Nature Protocols*, 1 (2021).
- [36] X. Zhao, X. Huang, X. Wang, Y. Wu, A.-K. Einfeld, S. Schwind, D. Gallego-Perez, P. E. Boukany, G. I. Marcucci, and L. J. Lee, *Nanochannel electroporation as a platform for living cell interrogation in acute myeloid leukemia*, *Advanced Science* **2**, 1500111 (2015).
- [37] P. E. Boukany, Y. Wu, X. Zhao, K. J. Kwak, P. J. Glazer, K. Leong, and L. J. Lee, *Nonendocytic delivery of lipoplex nanoparticles into living cells using nanochannel electroporation*, *Advanced Healthcare Materials* **3**, 682 (2014).
- [38] K. Gao, X. Huang, C.-L. Chiang, X. Wang, L. Chang, P. Boukany, G. Marcucci, R. Lee, and L. J. Lee, *Induced apoptosis investigation in wild-type and *flt3-itd* acute myeloid leukemia cells by nanochannel electroporation and single-cell *qrt-pcr**, *Molecular Therapy* **24**, 956 (2016).



- [39] A. Huebner, D. Bratton, G. Whyte, M. Yang, A. J. Demello, C. Abell, and F. Hollfelder, *Static microdroplet arrays: a microfluidic device for droplet trapping, incubation and release for enzymatic and cell-based assays*, *Lab on a Chip* **9**, 692 (2009).
- [40] Y. Kazayama, T. Teshima, T. Osaki, S. Takeuchi, and T. Toyota, *Integrated microfluidic system for size-based selection and trapping of giant vesicles*, *Analytical Chemistry* **88**, 1111 (2016).
- [41] Y. Xia and G. M. Whitesides, *Soft lithography*, *Annual Review of Materials Science* **28**, 153 (1998).
- [42] L. Retelj, G. Pucihar, and D. Miklavčič, *Electroporation of intracellular liposomes using nanosecond electric pulses—a theoretical study*, *IEEE Transactions on Biomedical Engineering* **60**, 2624 (2013).
- [43] J. C. Neu and W. Krassowska, *Asymptotic model of electroporation*, *Physical Review E* **59**, 3471 (1999).
- [44] K. A. DeBruin and W. Krassowska, *Modeling electroporation in a single cell. i. effects of field strength and rest potential*, *Biophysical Journal* **77**, 1213 (1999).
- [45] W. Krassowska and P. D. Filev, *Modeling electroporation in a single cell*, *Biophysical Journal* **92**, 404 (2007).
- [46] J. Li, W. Tan, M. Yu, and H. Lin, *The effect of extracellular conductivity on electroporation-mediated molecular delivery*, *Biochimica et Biophysica Acta (BBA)-Biomembranes* **1828**, 461 (2013).
- [47] G. Pucihar, T. Kotnik, D. Miklavčič, and J. Teissié, *Kinetics of transmembrane transport of small molecules into electropermeabilized cells*, *Biophysical Journal* **95**, 2837 (2008).
- [48] T. B. Napotnik and D. Miklavčič, *In vitro electroporation detection methods—an overview*, *Bioelectrochemistry* **120**, 166 (2018).
- [49] A. Muralidharan, L. Rems, M. T. Kreutzer, and P. E. Boukany, *Actin networks regulate the cell membrane permeability during electroporation*, *Biochimica et Biophysica Acta (BBA)-Biomembranes* **1863**, 183468 (2021).
- [50] Z. Fan, H. Liu, M. Mayer, and C. X. Deng, *Spatiotemporally controlled single cell sonoporation*, *Proceedings of the National Academy of Sciences* **109**, 16486 (2012).
- [51] T. Kotnik, G. Pucihar, and D. Miklavčič, *The cell in the electric field*, in *Clinical Aspects of Electroporation* (Springer, 2011) pp. 19–29.
- [52] M. Golzio, J. Teissié, and M.-P. Rols, *Direct visualization at the single-cell level of electrically mediated gene delivery*, *Proceedings of the National Academy of Sciences* **99**, 1292 (2002).

- [53] C. Rosazza, A. Buntz, T. Rieß, D. Wöll, A. Zumbusch, and M.-P. Rols, *Intracellular tracking of single-plasmid DNA particles after delivery by electroporation*, *Molecular Therapy* **21**, 2217 (2013).
- [54] C. Rosazza, S. Haberl Meglic, A. Zumbusch, M.-P. Rols, and D. Miklavcic, *Gene electrotransfer: a mechanistic perspective*, *Current Gene Therapy* **16**, 98 (2016).
- [55] A. Muralidharan, H. Uitenbroek, and P. E. Boukany, *Intracellular transport of electrotransferred DNA cargo is governed by coexisting ergodic and non ergodic anomalous diffusion*, *bioRxiv* (2021).
- [56] X. Ding, M. P. Stewart, A. Sharei, J. C. Weaver, R. S. Langer, and K. F. Jensen, *High-throughput nuclear delivery and rapid expression of DNA via mechanical and electrical cell-membrane disruption*, *Nature Biomedical Engineering* **1**, 1 (2017).
- [57] L. D. Cervia, C.-C. Chang, L. Wang, M. Mao, and F. Yuan, *Enhancing electrotransfection efficiency through improvement in nuclear entry of plasmid DNA*, *Molecular Therapy-Nucleic Acids* **11**, 263 (2018).
- [58] M. Mao, C.-C. Chang, A. Pickar-Oliver, L. D. Cervia, L. Wang, J. Ji, P. B. Liton, C. A. Gersbach, and F. Yuan, *Redirecting vesicular transport to improve nonviral delivery of molecular cargo*, *Advanced Biosystems* **4**, 2000059 (2020).
- [59] C. Faurie, M. Rebersek, M. Golzio, M. Kanduser, J.-M. Escoffre, M. Pavlin, J. Teissie, D. Miklavcic, and M.-P. Rols, *Electro-mediated gene transfer and expression are controlled by the life-time of DNA/membrane complex formation*, *The Journal of Gene Medicine* **12**, 117 (2010).
- [60] J.-M. Escoffre, T. Portet, C. Favard, J. Teissié, D. S. Dean, and M.-P. Rols, *Electro-mediated formation of DNA complexes with cell membranes and its consequences for gene delivery*, *Biochimica et Biophysica Acta (BBA)-Biomembranes* **1808**, 1538 (2011).



# 5

## CONCLUSION AND OUTLOOK

In the following sections, the conclusions of the research goals formulated in chapter 1 are briefly discussed. A perspective on the future research directions for each of the goals is also provided.

### 5.1. ROLE OF ACTIN

The formation of electropores on the plasma membrane as a response to electric fields is the basis of our fundamental understanding of biomolecule electrotransfer [1]. However, our knowledge of how the cytoskeletal protein networks inside the cell regulate the cell membrane electropermeability is limited. The first research goal of this dissertation was to understand the role of actin networks during electrotransfer. To achieve this, we monitored the electrotransfer of cell membrane-permeable molecules, which exhibit enhanced fluorescence upon cellular entry by chemically disrupting actin networks in chapter 2. Disruption of actin networks led to enhanced molecular uptake. By theoretically analyzing our measurements conducted at different temperatures, we found that the energy barrier of pore formation during electroporation is reduced upon actin disruption. Subsequently, this leads to enhanced cell membrane electropermeabilization when the actin network is disrupted. The increase in electropermeability of the cell membrane is correlated to the degree of actin disruption.

The demonstrated involvement of the actin cytoskeleton in electropermeability challenges the traditional electroporation models, which assume that only the lipid membrane is involved in electroporation. Now, recent experimental pieces of evidence point towards the involvement of the actin networks in regulating electropermeability [2, 3] and the electrophoretic disruption of the actin networks [3]. For obtaining predictive power over electroporation and associated molecular transport, theoretical models have to include the cell membrane mechanics regulation by the cytoskeletal networks. To aid further development of theory following questions need to be answered:

1. How are the cell membrane properties (surface tension and line tension) influenced by the microscopic membrane-cytoskeletal coupling?
2. How are the cell membrane properties influenced by the electric fields which disrupt the cytoskeleton?

3. How does the electrophoretic disruption of the cytoskeleton by an electric pulse influence the electroporation in subsequent pulses?

Experimental evidences show that theory still is unable to explain the observations made related to role of actin in electroporation. To move this field forward, theorists could possibly find clues from the mechanical coupling of the cytoskeleton to the cell membrane.

## 5.2. INTRACELLULAR DNA TRANSPORT

DNA forms DNA-membrane complexes when they are electrotransferred to a mammalian cell [4]. The complexes are then trafficked through the cell as a DNA cargo aided by intracellular trafficking machinery. Intracellular transport of electrotransferred DNA cargo was investigated for animal cell lines and human cancer cell lines (benign, malignant and metastatic) in chapter 3. Most DNA cargo stays stationary inside the cells after electrotransfer due to its low diffusion coefficient. The DNA cargo stochastically exhibits modes of superdiffusive transport, the probability of which is highest for metastatic cell lines followed by malignant and then benign cell lines. This combination of stochastic stationery directed transport leads to a weak ergodicity breaking. The directional transport supports the endocytotic model of intracellular transport of electrotransferred DNA cargo. Furthermore, the viscoelastic cytoplasm leads to a coexisting ergodic, non-ergodic kind of transport of the electrotransferred DNA cargo in the cells.

These experiments demonstrate that the properties of the cellular cytoplasm are a primary determinant for intracellular DNA cargo transport. However, our experimental setup was limited to observing only snippets of the intracellular DNA cargo transport and not the whole trajectory from the membrane to the nucleus due to photobleaching of the fluorescent tags. A unified theory that can predict the transfection efficiency for DNA electrotransfer will include predictions for intracellular DNA cargo transport, endosomal escape and translocation of the DNA across the nuclear pore complex [5–7]. Within the itinerary of the electrotransferred DNA cargo transport, the following questions remain unanswered:

1. How does the endosomal escape of the DNA cargo scale with DNA size and cell types?
2. How does the nuclear translocation of the DNA cargo scale with the DNA size?

Decisive experiments are still lacking to formulate predictive theories pertaining to this section. Here, we require using gene knockout experiments to understand which constitutive proteins are involved in the intracellular transport. Furthermore, advanced labelling strategies and super resolution nanoscopy will allow for resolving individual DNA cargo, and translocation of exogenous DNA through nuclear pore complexes.

## 5.3. MICRO-TRAP ELECTROPORATION

Localized electroporation has recently emerged as an alternative to conventional bulk electroporation as it offers better control over biomolecule delivery due to the preservation of cell viability [8]. Current localized electroporation devices often are limited to adherent cells or require manual micromanipulation to areas of high local electric

fields [9, 10]. This restricts the technique's applicability to a few cell lines and limits the throughput of the process. To overcome these issues, a localized electroporation device was fabricated by incorporating a PDMS based microtrap array in a microfluidic channel in chapter 4. The cells can be easily positioned in the microtrap array where there is a high local electric field using flow without requiring any micromanipulation.

The microtrap electroporation device allows us to electroporate cells and deliver small molecules and larger plasmid DNA without compromising cell viability. The next in this line of research is to test the device's compatibility with a broad range of cell types where there is an urgent need to deliver exogenous biomolecules. A highly relevant example of such a cell type would be human immune cells such as T cells and NK cells where expression of cancer-targeting chimeric antigen receptors are clinically relevant [11, 12]. In addition, testing the capability of the device to deliver a more broad range of molecules such as mRNA and genomic engineering tools such as CRISPR/Cas9 components would demonstrate the range of applications in which the technique could be used [13]. To optimize the design of the device geometries for localization electroporation and the hydrodynamic trapping, the numerical model of localized electroporation in this dissertation could be used. To make the technology commercially viable, finding methods to scale up the device from simply numbering up the microtraps to testing the possibility to use a continuous flow-through process would be fruitful. Furthermore, approaches to reduce the cost of fabrication of such devices need to be elucidated.

## REFERENCES

- [1] T. Kotnik, L. Rems, M. Tarek, and D. Miklavčič, *Membrane electroporation and electropermeabilization: mechanisms and models*, Annual Review of Biophysics **48**, 63 (2019).
- [2] A. Muralidharan, L. Rems, M. T. Kreutzer, and P. E. Boukany, *Actin networks regulate the cell membrane permeability during electroporation*, Biochimica et Biophysica Acta (BBA)-Biomembranes **1863**, 183468 (2021).
- [3] D. L. Perrier, A. Vahid, V. Kathavi, L. Stam, L. Rems, Y. Mulla, A. Muralidharan, G. H. Koenderink, M. T. Kreutzer, and P. E. Boukany, *Response of an actin network in vesicles under electric pulses*, Scientific Reports **9**, 8151 (2019).
- [4] S. Sachdev, A. Muralidharan, D. K. Choudhary, D. L. Perrier, L. Rems, M. T. Kreutzer, and P. E. Boukany, *DNA translocation to giant unilamellar vesicles during electroporation is independent of DNA size*, Soft Matter **15**, 9187 (2019).
- [5] C. Rosazza, H. Deschout, A. Buntz, K. Braeckmans, M.-P. Rols, and A. Zumbusch, *Endocytosis and endosomal trafficking of DNA after gene electrotransfer in vitro*, Molecular Therapy-Nucleic Acids **5**, e286 (2016).
- [6] L. D. Cervia, C.-C. Chang, L. Wang, and F. Yuan, *Distinct effects of endosomal escape and inhibition of endosomal trafficking on gene delivery via electrotransfection*, PLoS one **12**, e0171699 (2017).

- [7] L. D. Cervia, C.-C. Chang, L. Wang, M. Mao, and F. Yuan, *Enhancing electrotransfection efficiency through improvement in nuclear entry of plasmid DNA*, *Molecular Therapy-Nucleic Acids* **11**, 263 (2018).
- [8] J. Brooks, G. Minnick, P. Mukherjee, A. Jaber, L. Chang, H. D. Espinosa, and R. Yang, *High throughput and highly controllable methods for in vitro intracellular delivery*, *Small* **16**, 2004917 (2020).
- [9] P. E. Boukany, A. Morss, W.-c. Liao, B. Henslee, H. Jung, X. Zhang, B. Yu, X. Wang, Y. Wu, L. Li, *et al.*, *Nanochannel electroporation delivers precise amounts of biomolecules into living cells*, *Nature Nanotechnology* **6**, 747 (2011).
- [10] S. S. P. Nathamgari, N. Pathak, V. Lemaitre, P. Mukherjee, J. J. Muldoon, C.-Y. Peng, T. McGuire, J. N. Leonard, J. A. Kessler, and H. D. Espinosa, *Nanofountain probe electroporation enables versatile single-cell intracellular delivery and investigation of postpulse electropore dynamics*, *Small* **16**, 2002616 (2020).
- [11] T. Ingegnere, F. R. Mariotti, A. Pelosi, C. Quintarelli, B. De Angelis, N. Tumino, F. Besi, C. Cantoni, F. Locatelli, P. Vacca, *et al.*, *Human car nk cells: a new non-viral method allowing high efficient transfection and strong tumor cell killing*, *Frontiers in immunology* **10**, 957 (2019).
- [12] E. S. Atsavaprane, M. M. Billingsley, and M. J. Mitchell, *Delivery technologies for t cell gene editing: Applications in cancer immunotherapy*, *EBioMedicine* **67**, 103354 (2021).
- [13] M. P. Stewart, R. Langer, and K. F. Jensen, *Intracellular delivery by membrane disruption: mechanisms, strategies, and concepts*, *Chemical Reviews* **118**, 7409 (2018).

# PROPOSITIONS

1. The electroporation theory based on energetic costs of local membrane electro-pore opening fails to describe the added energy costs from anchored cytoskeletal networks.  
*This proposition pertains to chapter 2 of this thesis.*
2. It is not the DNA size but what it encounters in the cytosol which governs the intracellular electrotransferred DNA cargo transport.  
*This proposition pertains to chapter 3 of this thesis.*
3. A unified theory of electro-transfection will include the DNA size-dependent DNA-membrane complex formation and cell line dependent intracellular activity.  
*This proposition pertains to chapter 3 of this thesis and Sachdev et al., BBA Biomembranes, 2020.*
4. Scale-up is best achieved through continuous processing, that holds for localized electroporation.
5. Electroporation theoretical models help predict whether the cell membrane is permeabilized but do not help predict the associated molecule transport kinetics.
6. The global rollout of biomolecule electrotransfer in clinics will be governed by cost rather than the high efficiency and control that localized electroporation devices promise.  
*Based on ElectroPen (Byagathvalli et. al., PLoS Biology, 2020) and ePatch (Xia et. al., PNAS, 2021)*
7. Therapeutic promise of CRISPR-Cas9 will be met only when difficulty in delivering the required biomolecules *in vivo* is addressed.
8. Target specifications come first, and research questions second when it comes to development of new technologies.
9. The COVID-19 pandemic has shown that in-person mega-conferences are a waste of taxpayer money.
10. Lack of scores for gender diversity in the university rankings is the cause of gender inequality among university principal investigators.





# ACKNOWLEDGEMENTS

It is a bittersweet moment when you finish a four-year doctoral project. First, there is the sense of satisfaction of contributing to a field and creating a tiny bit of new knowledge. At the same time, you are filled with several ideas to explore which cannot be finished within the short duration of the project. For providing me the opportunity and environment to do and feel so, I thank **Pouyan** and **Michiel**. **Pouyan**, I am grateful to you for my personal and professional development over the last several years (in fact, we started working together from my masters). Apart from the research which ended up in this dissertation, I am thankful to you for letting me explore other areas through numerous collaborations within and outside the group. **Michiel**, your critical thinking, focus on the fundamentals and precision required for the problem at hand, and hypothesis-driven approach to research are genuinely inspiring. Although our time together was cut short when you became the dean of Leiden University, I learned a lot from our meetings about my research or transport phenomena. The yearly Christmas dinner you hosted at your home is already missed by all who had the opportunity to experience it.

I also feel fortunate to have not to look too far to get help. **Lea**, we have been involved in multiple projects together, and you had a substantial contribution to this dissertation as a whole. You were always someone I could look up to with absolute confidence of getting an answer in anything related to electroporation, right from the beginning by introducing me to the field through EBTT in Ljubljana. **Shaurya**, we have come a long way from the student-supervisor relationship we had during my masters. Being my first supervisor in Delft, you significantly influenced my scientific working style, and I couldn't be more grateful for your guidance (personally and professionally) even after your Ph.D. I also look forward to us having more conversations in Malayalam, now that you are (un)officially almost a Malayali. **Dayinta**, although we did not overlap much during our Ph.D. timeline, we overlapped in figuring out how actin is involved in electroporation. I also fondly remember you as one of the best teaching assistants during my masters with your calm and bubbly demeanor while always providing closure to the question asked.

And the unofficial members of the getting DNA into cells team. **Georg**, I am lucky to have bribed you into joining the micro-trap array electroporation project. While it started as a rough idea which a master student was working on, it wouldn't have reached the current stage without your help. Best wishes for starting your own group now in Dublin. **Qian** and **Yi**, you both were able to contribute a lot to the projects I was leading during our time together as officemates. We also managed to work together quite well and had several quick but successful experiments; micro bucket electroporation and functionalizing your microbuckets with lipids, to name a few. I look forward to the new steps in your life, both as new PI and as a parent. Knowing you and **Meng**, I am sure you will do both the steps exceptionally well. **Reece** and **Rienk**, it was nice having someone around who wanted to put DNA into cells, although in your case, not with an electric field. I am impressed by the number of things and techniques we tried out and looking forward to how the scientific community values the effort.

I am also grateful to the several students who found the topics I worked on interesting. For this, I have to thank **Jazzy**, **Parsa**, **Hans**, **Narayani**, **Birte**, **Ivo**, **Pim**, **Jan**, and

**Kyriacos.** **Jazzy** and **Parsa**, you were my first students within the first months of my project working on mechanical properties of cells and cell mimicking systems using optical tweezers. **Jazzy**, I don't think I know any other person who managed to finish a bachelors degree at the age of 19. Your help with the LO-1 projects cannot be thanked enough. Furthermore, together with you I was confident of growing cells and keeping them alive without a contamination. **Parsa**, you continued to help me with being a teaching assistant for applied transport phenomena. I am happy to have gotten the opportunity to watch you grow from doing a bachelor thesis to a doctoral program, and I am sure you will make an excellent scientist. I will remember you challenging me with the theoretical foundations of nanotube pulling from the cell membranes. I would have loved to have closed that question and the contribution of actin to the cell mechanics to you, but we had limited time in a bachelor's thesis. **Hans**, you were as excited as me to look at how DNA delivered to cells walk around. Your rigorous efforts on this challenging project directly helped me set up one of the toughest chapters in my Ph.D., and I am grateful for that. I still think there is a lot still learn from the dataset we generated together. I will always remember you casually mentioning that you have a hard deadline to defend since you had to get married exactly eight months after starting your thesis. **Narayani**, we learned together that using microfluidics to make "synthetic cells" is not a walk in the park. However, our early designs laid the foundations to perform localized electroporation of cells on a chip. **Birte**, although you were from a different university with no experience in microfluidics or electroporation, you quickly adapted to the challenge and started performing electroporation in microfluidic devices. Your efforts led to another one of my chapters in this dissertation, and I am grateful for that. Furthermore, I loved the Belgian chocolates that you gave me when you left. **Ivo**, you were extremely structured, organized and did not hesitate to ask for precise help needed for your progress. It was a pleasure to supervise you on your bachelor thesis in which you showed maturity and dedication, which surpasses even master students. **Pim**, you had a challenging task of having to communicate to two supervisors entirely through remote sessions during the pandemic, and your growth during the project is commendable. **Jan** and **Kyriacos**, my apologies for being more conservative with my availability as I was nearing towards the end of my project timeline. **Jan**, I gave you an ambitious project to understand how the electrotransfer of different molecules works in realistic tumor mimicking systems. It was never expected to be an easy task, and your hard work provided big progress for our lab in this field. We had minimal experience working with spheroids or extracellular matrix mimicking systems. And you still managed to come a long way from the beginning. You should be proud of your work. **Kyriacos**, you were given a task to reveal the mystery of "enhanced viability" of living cells during electroporation when there is a co-transfer agent. Your critical scientific attitude and creativity were refreshing, and I am happy we finally have evidence to support our early hypothesis.

Having experienced a period without technical support, I know that the road would have been more challenging if I didn't have excellent technicians during the Ph.D. period. **Wim**, thanks for showing me how to work in PPE labs. **Durgesh**, thanks for all the help with ordering the microscope incubators. **Mojgan**, thanks for the help with maintaining the lab when there were no mammalian lab technicians. **Erwin**, you showed me how to grow bacteria, express plasmids in them, make glycerol stocks and extract plasmid

DNA using purification kits. I never thought my next job would require those skills on an everyday basis. Furthermore, thanks for all the help with making sure all the work we do is safe and has the approval of the biosafety officer. **Bas**, your deep interest in the science we did and what it meant for the medical community was nice to be around. You also showed me and **Hans** how to speed up our lab work and test out different ways to make cells happier. **Kristen**, thanks for all the help in purifying the plasmid DNA over the last year. Also, thanks for responding quickly when the microscopes were down and maintaining the labs for the last couple of years.

The last two years of my Ph.D. (during the corona pandemic) would have been a different story if not for the moments shared outside work. After all, good friends are life's treasures. For making sure we stayed in touch and had a day per week to cook together and have fun, I cannot thank **Isabell, Dominik, Zaid, Margherita, and Lukas** enough. **Izzy**, thanks for the company during all the coffee/chocolate/lunch/COMSOL/scaling breaks we had and for opening up your home on almost all Saturdays in the last years. We made a habit of leaving the office together after work and discussing how the day went, and I couldn't think of a better paronymph who knows my project more to help me defend this thesis (you already had the initial preparation while drawing the cover). I trust our training sessions in the gym will pay off during the defence. **Domi**, we have visited the fries shop so many times that the server even knows which sauce we want when he sees us. I was hoping one of these days you may finally convince me to work out (maybe even a pullup without taking 45 minutes of convincing) instead of having fries, but then you gave up and decided to leave to Aachen. Jokes aside, I highly appreciate you being around, and best wishes for your new career steps (and the astronaut application). **Zaid**, bruh, I don't think I will ever taste a beef dry fry better than the one you make. And also, thanks for giving me company for losing horribly in monopoly. I am truly happy that I am one of the people you are not polite to anymore (especially developing intolerance to my bad jokes). **Meg**, we both have the absolute least willpower when it comes to food. But thanks for always saying, "No!!!! We are the worst!!!! I am on my way!!!!" if I check with you to go for ice cream or a pizza. **Luki**, thanks for making sure we do proper workout in the gym (if we actually go), all the dinners you and **Izzy** hosted, and being there as a person who I could send Tool, Gojira and Polyphia songs to.

And to my other family away from home, **Anirudh, Jishnu, Varsha, Amit**, I hardly felt homesick in the last six years in Delft with all of you around. **Andiru**, my second paronymph, your dedication to anything you put your mind to is truly inspiring. Talking to you always forces me to think of the bigger picture of everything we do. Thanks for always keeping your door open for an evening chaya, dinner, talks about the project, or even about setting up our own startups. **Jinsu**, we have known each other for more than half our lives, and it was great having you around a quick train ride away. The (road)trips you initiate were always a welcome breeze in our busy lives. **Andiru** and **Jinsu**, we should seriously consider making Balarama Pvt. Ltd. a reality someday. **Vidhu**, thanks for being the glue that keeps the group together. **Koi**, you were basically the person who I call if I had a difficult week during both the master thesis and the doctoral thesis. Thanks for always lending an ear and giving (in)appropriate advice. **Manu, Gokul, and Shreya**, thanks for the tiny European NITC get-togethers. **Adarsh** and **K P**, thanks for keeping me company even after all these years and having to listen to the "boring" science talks.

**Chythan**, from our time in KV to now, we never ran out of topics to chit chat about.

Next comes the different generations of Ph.D. candidates, postdocs who spend their time in PPE, who in different ways have contributed to the completion of this thesis. **Maulik**, although most people in their acknowledgments mention your calmness, I remember you for our shared time as an ATP TA. I always found your work extremely elegant and conversations with you refreshing. **Kartik**, unlike Maulik, our common struggle was in the lab. Cheers to all those long hours of leaking microfluidic setups, dying cells, and several failed and successful experiments. I hope we do meet again as colleagues sometime in the future in Indian academia. **Damiano**, my first day in PPE as a master student, you were defending your master thesis. I would have never realized that both of us would continue to stay in the same group for the next four years. Whenever I thought I was leaving late from work and no one would be around, you continued to show that isn't true. **Afshin**, we both shared a love for biophysics, and I was always excited to have someone as critical as you around. We never got to the end of our discussion on whether cell membranes have a surface tension or not. **Hamid** and **Fatemeh**, I am thankful for you being so calm amongst all the chaos **Domi**, **Shaurya** and I created in the office. I never heard either of you complain about a bad day in the lab, and that really showcased how mature you both were as senior members of our research group. **Fabio**, you were finishing up when I started, and we did not spend much time together. I am also grateful for how quickly you helped me with the questions I had with anomalous diffusion. **Erik**, good luck with finishing up your thesis and starting your new job. **Alessandro**, although we spent so little time in the group (just two months), I am glad we became good friends over the last two years. **Ale** and **Martina** thanks for all the visits, and I definitely would come over to Würzburg one of these days (who are we kidding). **Abtin**, not every day you come across someone who point-blank asks what the novelty of your work is. I was happy to have your critical mind around and someone who thought a lot about the right questions to ask before diving in. **Saeed**, you were quite caring about everyone in the group, and I highly admire that. Thanks for all the offers of help and advice. **Feilong**, we discussed a lot of possibilities of working together with optical tweezers and how we can use them for characterizing pharmaceutically relevant materials. Although our work didn't overlap much, looking from afar, your work here at PPE was amazing. **Mahdiyeh**, we came officemates for a very short duration towards the end of both our Ph.D. projects, but still you managed help me with important experiments. Thanks for the beautiful SEM images you took for me. **Fuweng**, **Ruben**, **Albert**, **Rens**, **Christian**, **Lukas**, **Ming** we didn't overlap a lot in our work but thanks for making PPE a social place to be. **Ruud**, **Gabrie**, **Alina**, **Volkert** thanks for keeping the group functional with active discussions.

Having done the master thesis in the group down the corridor, there was no lack of connections around. First, thanks to **Sasa** for all the help, right from supervising my master thesis, to always having a nice word when we meet in the corridor. The joy on your face and appreciative words when we meet, even after all these years, is inspirational enough. **Sid**, I am thankful for many things, but mostly for introducing me to Tool, which naturally made every day more joyful. Apart from Tool, you always inspire with your intellect, skills in music, photography, and scientific acumen. **Christiaan**, thanks for continuing to help me with any technical stuff even after moving out of the lab with

the Hulk. **Manu, Minu** thanks for always being around for a quick chat in Malayalam. **Manas**, thanks for making all the TP borrels lively.

And finally not but the least comes the family members. **Sreekumar**, thanks for making science an attractive field to be in from my childhood. Somehow, no other profession seemed as appealing after seeing all the cool stuff you are doing. It is a pity that our fields don't overlap (yet). **Sreejith**, although neither of us knew it back then, you prepared me for the Netherlands by teaching me to ride a bike and swim, two essential Dutch survival skills. Furthermore, you showed me my way around computers, from the basics to taking the ram out of the CPU to clean it if the CPU started beeping (trust me, that helped in my Ph.D.). **Achachan**, it was your wish that I write a book, and here it is. I would have loved to share it with you and talk you through the content. **Ammamma**, thanks for always being an enthusiastic audience. Although you probably think what I do is way cooler than reality, it was nice to talk to you about my work. **Anandu**, you have so far done everything better than I did, and I hope you find what you do exciting. Finally, **Achan** and **Amma**, the two main people of this thesis from the background. Somehow, your combination of mathematical and biological backgrounds perfectly fits the story told in this thesis. **Achan**, thanks for showing me the value of integrity and always asking me not to let stress get to me. **Amma**, although most of our calls sound like shouting matches to people around, we both know it is out of love, and I wouldn't exchange our daily calls for anything else.



# CURRICULUM VITÆ

## Aswin MURALIDHARAN

04-01-1993 Born in Calicut, Kerala, India.

### EDUCATION

2010 – 2014 Bachelor of Technology in Chemical Engineering.  
National Institute of Technology Calicut, India.

2015 – 2017 Master of Science (Honours) in Chemical Engineering, *Cum Laude*.  
Delft University of Technology, the Netherlands.

*Thesis:* In-vitro validation of cardiovascular flow measurements using particle image velocimetry.

*Supervisor:* Prof. dr. dipl.-ing. S. Kenjereš.

*Honours thesis:* Single molecule breakup dynamics of polymeric droplets using microfluidics and single DNA imaging.

*Supervisors:* Dr. P.E. Boukany.  
Dr. ir. S. Sachdev.

2017 – 2021 Doctor of Philosophy.  
Delft University of Technology, the Netherlands.

*Dissertation:* Biomolecule electrotransfer to mammalian cells.

*Promotors:* Prof. dr. ir. M.T. Kreutzer.  
Dr. P.E. Boukany.

### WORK EXPERIENCE

2013 Intern at the Indian Space Research Organization in Trivandrum, India.

2014 – 2015 Graduate engineering trainee at Reliance Industries Ltd in Vadodara, India.

2021 – present Post doctoral researcher at the Kavli Institute of Nanoscience,  
Department of Bionanoscience, Delft University of Technology,  
the Netherlands.

*Advisor:* Dr. S.J.J. Brouns.





# LIST OF PUBLICATIONS

## JOURNAL PUBLICATIONS RELATED TO THIS DISSERTATION:

7. R. Lewis, **A. Muralidharan**, P. E. Boukany, R. Eelkema, "GSH responsive cationic charge reversion polymers for cell transfection.", *Under preparation*.
6. M. Scuderi, J. Dermol-Černe, C. Amaral da Silva, **A. Muralidharan**, P. E. Boukany, L. Rems, "Models of electroporation and the associated transmembrane molecular transport should be revisited." *Bioelectrochemistry*, 2022.
5. **A. Muralidharan**, G. R. Pesch, H. Hubbe, L. Rems, M. Nouri-Goushki, P. E. Boukany, "Micro-trap array on a chip for localized electroporation and electro-gene transfection.", *Bioelectrochemistry*, 2022.
4. **A. Muralidharan**, H. Uitenbroek, P. E. Boukany, "Intracellular transport of electrotransferred DNA cargo is governed by coexisting ergodic and non ergodic anomalous diffusion.", *Under review*. A preprint is available in bioRxiv.
3. **A. Muralidharan**, L. Rems, M. T. Kreutzer, and P. E. Boukany, "Actin networks regulate the cell membrane permeability during electroporation.", *BBA-Biomembranes*, 2021.
2. S. Sachdev, **A. Muralidharan**, D. K. Choudhary, D. L. Perrier, L. Rems, M. T. Kreutzer, and P. E. Boukany, "DNA translocation to giant unilamellar vesicles during electroporation is independent of DNA size.", *Soft Matter*, 2019.
1. D. L. Perrier, A. Vahid, V. Kathavi, L. Stam, L. Rems, Y. Mulla, **A. Muralidharan**, G. Koenderink, M. T. Kreutzer, and P. E. Boukany, "Response of an actin network in vesicles under electric pulses.", *Scientific Reports*, 2019.

## OTHER JOURNAL PUBLICATIONS:

6. A. R. Costa, D. F. van den Berg, J. Q. Esser, **A. Muralidharan**, H. van den Bossche, B. E. Bonilla, B. A. van der Steen, A. C. Haagsma, F. L. Nobrega, P.-J. Haas, S. J. J. Brouns, "Accumulation of defense systems drives panphage resistance in *Pseudomonas aeruginosa*.", *Under review*. A preprint is available in bioRxiv.
5. H. Hubbe, **A. Muralidharan**, E. Mendes, P. E. Boukany, "Bifunctional micelles for biological assays.", *Under review*.
4. Q. Liu, **A. Muralidharan**, A. Saateh, Z. Ding, P. ten Dijke, P. E. Boukany, "A programmable multifunctional 3D cancer cell invasion micro platform.", *Small*, 2022.
3. S. S. Khalafvand, J. D. Voorneveld, **A. Muralidharan**, F. J. H. Gijsen, J. G. Bosch, T. van Walsum, A. Haak, N. de Jong, and S. Kenjeres, "Assessment of human left ventricle flow using statistical shape modelling and computational fluid dynamics.", *Journal of Biomechanics*, 2018.
2. J. D. Voorneveld, **A. Muralidharan**, T. Hope, H.J. Vos, P. Kruizinga, A. F. W. van der Steen, F. J. H. Gijsen, S. Kenjeres, N. de Jong, and J. G. Bosch, "High frame rate ultrasound particle image velocimetry for estimating high velocity flow patterns in the left ventricle.", *IEEE Transactions on Ultrasonics, Ferroelectrics, and Frequency Control*, 2017.

1. S. Sachdev, **A. Muralidharan**, and P. E. Boukany "Molecular processes leading to "necking" in extensional flow of polymer solutions: using microfluidics and single DNA imaging.", *Macromolecules*, 2016.

## CONFERENCE PROCEEDINGS/PRESENTATIONS:

7. **A. Muralidharan**, G. R. Pesch, H. Hubbe, L. Rems, M. Nouri-Goushki, P. E. Boukany, World Congress of Electroporation and Pulsed Electric Fields in Biology, Medicine, and Food & Environmental Technologies, Copenhagen, Denmark, *Oral Presentation*, 2022.
6. **A. Muralidharan**, L. Rems, D. L. Perrier, M. T. Kreutzer, P. E. Boukany, Physics @ Veldhoven, Veldhoven, the Netherlands, *Oral Presentation*, 2019.
5. **A. Muralidharan**, L. Rems, D. L. Perrier, M. T. Kreutzer, P. E. Boukany, World Congress of Electroporation and Pulsed Electric Fields in Biology, Medicine, and Food & Environmental Technologies, Toulouse, France, *Oral Presentation*, 2019.
4. **A. Muralidharan**, M. T. Kreutzer, P. E. Boukany, Physics @ Veldhoven, Veldhoven, the Netherlands, *Poster Presentation*, 2018.
3. **A. Muralidharan**, J. de Waard, M. T. Kreutzer, P. E. Boukany, Burgers Symposium, Lunteren, the Netherlands, *Oral Presentation*, 2018.
2. **A. Muralidharan**, W. de Haan, L. Rems, M. T. Kreutzer, P. E. Boukany, Electroporation-Based Technologies and Treatments, Ljubljana, Slovenia, *Oral Presentation*, 2017.
1. J. D. Voorneveld, **A. Muralidharan**, T. Hope, H.J. Vos, P. Kruizinga, A. F. W. van der Steen, N. de Jong, F. J. H. Gijssen, S. Kenjeres, and J. G. Bosch, IEEE International Ultrasonics Symposium, Washington, United States of America, *Oral Presentation*, 2017.